



University of Brasília - UnB

Master's Program in Nanoscience and Nanobiotechnology
(PPGNANO)

Kissia Batista Ferreira

Correlation of the size of self-assembled silver nanoparticles in phosphate glasses modified with aluminum or zinc oxides in RAMAN-SERS signal aiming application as early biomarker-related disease diagnosis

Masters Dissertation

BRASÍLIA
2020

Kissia Batista Ferreira

Correlation of the size of self-assembled silver nanoparticles in phosphate glasses modified with aluminum or zinc oxides in RAMAN-SERS signal aiming application as early biomarker-related disease diagnosis

Master's Dissertation presented to the Graduate Program in Nanoscience and Nanobiotechnology of the Biology Institute of University of Brasília as a partial requirement for obtaining the title of Master in Nanoscience and Nanobiotechnology.

Supervisor: Prof. Dr. Juliano Alexandre Chaker

BRASÍLIA
2020

To my mother and father, Terezinha and Eduardo, I dedicate this work, who encouraged me in the search of knowledge.

Acknowledgments

This scientific journey I experienced was full of surprises, challenges, struggles and realizations. I feel grateful for everyone who have been a part of this moment, that helped and guided me until now. Here, I thank everyone who made it possible.

I want to thank Prof. Juliano Alexandre Chaker, for always believing in my potential and making me become better. His guidance and friendship were crucial to develop my maturity in the scientific field and support me through challenges. To my lab friends Prof. Marcelo Henrique Sousa, who assisted me many times and always amused me with his good spirit, making my workdays funnier, and to Atailson, Mac-Kedson and Eliane for always sharing their knowledges and contributing to my personal development.

I thank Prof. Ricardo Schneider for providing all the support needed with my samples and their supplies. I deeply thank Prof. Sebastião da Silva and his students Isis and Alexandre, who instructed and assisted me countless times during all my analysis with Raman that, without them, my work could not have been completed. My gratitude to Prof. Jorlândio Felix for his knowledge and assistance with my SERS analysis.

I thank Felipe de Almeida, who encouraged and pushed me to never give up, while providing me strength and carefulness (which I deeply needed to keep my sanity). His contribution was more than what I could ever ask. I Thank all my beautiful friends Angela, Marina, Eduardo, Leonardo, Lucas, Lúcio e Roberto, for always believing, cheering for me and watching me at difficult moments.

I specially thank my family, who provided me always with the best, assisting me in all necessary aspect. To Jessica Ferreira, my precious sister, who always believed in me, and helped me with her encouragement. To Terezinha Ferreira, my mother, who gave my freedom to pursue my dreams and engage in the science field, while supporting me with my expenses. To Eduardo Ferreira, my father, who introduced me to science and always inspired me to seek knowledge.

I thank all the collaborators and friends, here not mentioned, who indirectly helped me within this past two years.

“Ignorance more frequently begets confidence than does knowledge: it is those who know little, and not those who know much, who so positively assert that this or that problem will never be solved by science.”

Charles Darwin

“Nothing in life is to be feared, it is only to be understood. Now is the time to understand more, so that we may fear less.”

Marie Curie

Abstract

FERREIRA, K. B.. **Correlation of the size of self-assembled silver nanoparticles in phosphate glasses modified with aluminum or zinc oxides in RAMAN-SERS signal aiming application as early biomarker-related disease diagnosis.** Masters Dissertation – Graduate Program in Nanoscience and Nanobiotechnology, University of Brasília, Brasília, 2020

The use of nanostructured SERS substrates in biomolecule detection has gaining considerable attention as they offer great sensitivity and specificity, displaying a very promising application for early disease diagnoses of biomolecule-related (expressing biomolecules) diseases. Albeit the innumerable substrates developed with this objective, many lacks in few crucial criterions for clinical or point-of-care applications such as sensitivity, resistivity, high spectroscopic performance and reproducibility. This is a consequence of the difficulty in getting strong Raman signal enhancements with simple approaches, either by substrate structuring or analysis methods. Under those circumstances, it was investigated in this work the potential of two borophosphate glass compositions (modified with aluminum or zinc oxides) as nanostructured SERS substrates for detecting a standard dye molecule and, subsequently, their potential in detecting biomolecules under different conditions. And, since the method for acquiring metallic nanoparticles can influence in SERS effect (in respect of particle size, morphology and arrangement) and in biomolecule interaction (due to the surface characteristics of the nanoparticle) the influence of the nanoparticle obtainment process in the vitreous structure was also investigated. Thus, this study also involved the portrait of the main differences between the glass compositions, when thermally treated at different times for the growth of nanoparticles (bottom-up), accessing the structural conformation of the glassy network, the general thermal stability of the matrices and the morphology of the nanoparticles for each treatment time. It was observed that thermal treatment changes insignificantly the glass matrices, but the difference in thermal stability and degree of packing among them results in different nanoparticles growth rates, culminating in distinct nanoparticle size distributions between same treatment time. SERS effect was achieved for the spherical-like nanoparticles at similar sizes, estimated to be between 34 to 38 nm, and with an enhancement factor greater than the overall found in the literature, having maximum value calculated in 1.7×10^7 for aluminum and 7×10^6 for zinc modified glass. Biomolecule detection showed to be promising with PCA analysis, but biomolecule adsorption and respective SERS analysis must be further investigated.

Resumo

FERREIRA, K. B.. **Correlação do tamanho de nanopartículas de prata automontadas em vidros fosfatados modificados com óxidos de alumínio ou zinco no sinal RAMAN-SERS visando aplicação como diagnóstico precoce de doenças relacionadas a biomarcadores.** Dissertação de Mestrado - Programa de Pós-Graduação em Nanociência e Nanobiotecnologia, Universidade de Brasília, Brasília, 2020.

O uso de substratos SERS nanoestruturados na detecção de biomoléculas vem ganhando considerável atenção por oferecerem grande sensibilidade e especificidade, mostrando uma aplicação bastante promissora para diagnósticos precoces de doenças relacionadas a (que expressem) biomoléculas. Apesar dos inúmeros substratos desenvolvidos com esse objetivo, muitos carecem de alguns critérios cruciais para aplicações clínicas ou no local de atendimento, como sensibilidade, resistividade, alto desempenho espectroscópico e reprodutibilidade. Isso é consequência da dificuldade de obter fortes melhorias de sinal Raman com abordagens simples, seja pela estruturação do substrato ou pelos métodos de análise. Nessas circunstâncias, investigou-se neste trabalho o potencial de duas composições de vidro borofosfato, modificadas com óxidos de alumínio ou zinco e dopadas com prata, como substratos SERS para detecção de uma molécula de corante padrão e, posteriormente, o potencial desses na detecção de biomoléculas em diferentes condições. E, como o método para aquisição de nanopartículas metálicas pode influenciar no efeito SERS (em relação ao tamanho, morfologia e arranjo das partículas) e na interação com biomoléculas (devido às características superficiais da nanopartícula), foi examinada também a influência do processo de obtenção de nanopartículas de prata na estrutura vítrea. Assim, este estudo envolveu também o retrato das principais diferenças entre as composições vítreas, quando tratados termicamente em diferentes tempos para o crescimento de nanopartículas (*bottom-up*), acessando a conformação estrutural da rede vítrea, a estabilidade térmica geral das matrizes e morfologia das nanopartículas para cada tempo de tratamento. Observou-se que o tratamento térmico altera de forma insignificante as matrizes de vidro, mas a diferença de estabilidade térmica e grau de empacotamento entre elas resulta em diferentes taxas de crescimento de nanopartículas, culminando em distribuições distintas de tamanho de nanopartículas no mesmo tempo de tratamento. O efeito SERS foi alcançado para as nanopartículas esféricas em tamanhos semelhantes, estimadas entre 34 e 38 nm, e com um fator de aumento maior que o padrão alcançado na literatura, tendo valor máximo calculado em $1,7 \times 10^7$ para alumínio e 7×10^6 para vidro modificado com zinco). A detecção de biomoléculas mostrou-se promissora com a análise de PCA, mas a adsorção de biomoléculas e a respectiva análise SERS devem ser mais investigadas.

Figures List

Figure 1. Cancers rate incidence (per 100,000) of prostate, breast, colon (male/female) and lung (male/female) from 2000 to 2016 in Brazil.....	2
Figure 2. XRD patterns of 200PBAI (green) and 300PBZn (purple) glasses without thermal treatment (0 min.) and with annealing time of 5 and 12 min. each.....	32
Figure 3. Rietveld refinement of the glass precursors. Calculated (straight light orange line) and experimental ZnO (purple dots), H ₃ BO ₃ (green dots), Al ₂ O ₃ (orange dots) and NaH ₂ PO ₄ (blue dots) diffraction patterns.....	33
Figure 4. Experimental diffractogram of borophosphate glass samples (uppermost) modified with aluminum (green shades) or zinc (purple shades) and glass precursors (NaH ₂ PO ₄ – dash line, H ₃ BO ₃ – straight line with open circle, Al ₂ O ₃ – straight line and ZnO – straight line open triangle). ...	34
Figure 5. DSC analysis of borophosphate glass matrices modified with aluminum (left, green lines) and zinc (right, purple lines), in their respective annealing times (2 – 12 min).....	36
Figure 6. Raman spectra (532nm) of borophosphate glass samples modified with aluminum (left) and zinc oxides (right) without thermal treatment (0 min.) and with annealing time of 2, 5, 8 and 12 min. each	41
Figure 7. Raman spectra (532nm) of borophosphate glass samples modified with aluminum without thermal treatment.....	42
Figure 8. Raman spectra (532nm) of 200PBAI (left) and 300PBZn (right) at their corresponding annealing times (a-0 min, b-2 min, c-5 min, d-8 min and e-12 min).	43
Figure 9. Raman spectra (532nm) of borophosphate glass samples modified with zinc without thermal treatment.....	46
Figure 10. FTIR spectra of borophosphate glass matrices modified with aluminum without thermal treatment.....	49
Figure 11. FTIR spectra of borophosphate glass matrices modified with zinc without thermal treatment.	50

Figure 12. FTIR spectra of borophosphate glass matrices modified with aluminum (green) and zinc (purple) without thermal treatment and with thermal treatment with 12 min.....	51
Figure 13. SEM images of borophosphate glasses modified with aluminum (left side) annealed for 2 (a), 5 (b), 8 (c) and 12 (d) minutes and zinc (right side) annealed for 2 (e), 8 (f) and 12 (g and h) min.	57
Figure 14. Normality plot of silver nanoparticle grown on both glass sample matrices (modified with aluminum or zinc), thermally treated for 8 min. Normally (200PBA18) and non-normally (300PBZn8) distributed data are compared.....	58
Figure 15. Boxplot of non-normal size distribution of nanoparticles grown on both glass matrices (modified with aluminum or zinc), at their respective thermal treatment time (2-12 min.). The dispersity of NP size (dot scores) has fixed values for “x” axis, varying only in the “y” axis.....	59
Figure 16. Linear regression fit (red line) of the nanoparticle size median, grown on borophosphate matrices containing aluminum (triangle) or zinc (circle), with their corresponding line equation, Pearson’s correlation coefficient (r), and R2 of each. The calculated NP size for HT time of 5min. for both lattices are represented as the blue star, with estimated standard deviation.	61
Figure 17. Nanoparticle size distribution of 200PBA1 and 300PBZn borophosphate glass sample sets at their respective thermal treatment time (2-12 min).....	63
Figure 18. UV-VIS absorbance spectra of 200PBA1 (uppermost) and 300PBZn (lowermost), at their respective thermal treatment time (in minutes).....	66
Figure 19. Normal Raman spectra of Cresyl Violet Perchlorate (CVP) at 1 M concentration and its enhanced Raman spectra obtained by SERS using 200PBA1 set (a) and 300PBZn set (b) at the different annealing times (2 – 12 min), with concentrations of 10 ⁻⁶ M, 10 ⁻³ M and 1 M (front to back). (c) Chemical structure of CVP.....	70
Figure 20. SERS of the CVP most intense peak (around ~592 cm ⁻¹), at concentrations 1, 1x10 ⁻³ and 1x10 ⁻⁶ mol.l ⁻¹ , obtained on 200PBA1 (a) and 300PBZN (b) vitreous substrates, at their respective annealing times (in minutes). The scales were adapted (cut) for better visualization.....	71
Figure 21. SERS substrate enhancement factor of borophosphate glasses modified with aluminum (a) and zinc (b) according to their respective heat treatment time (in minutes) and CVP concentration	

(1, 1×10^{-3} and 1×10^{-6} mol.l⁻¹) compared to normal Raman signal of CVP obtained at 1 M. The scales were adapted (cut) for better visualization. 73

Figure 22. (a) Normal Raman spectra of BSA (i), 200PBA18 (ii) and 300PBZn5 (iv), with respective BSA SERS spectra collected on 200PBA15 (iii) and 300PBZn (v). (b) Normal Raman spectra of anti-HIL2 (i) and carbonate buffer (ii), with respective SERS spectra collected on 200PBA18 (iii) and 300PBZn5 (iv). SERS were collected subsequent ambient drying. 75

Figure 23. PCA scatter plot of BSA samples and vitreous substrates. ● (light purple) 200PBA18, ● (dark purple) 300PBZn5, ● (light blue) BSA Raman spectra, ● (light pink) 300PBZn5 + BSA 1µM, ● (red) 300PBZn + BSA 1nM, ● (light green) 200PBA18 + BSA 1µM..... 77

Figure 24. PCA scatter plot of anti-HIL2 samples and vitreous substrates. ● (light purple) - HIL2 antigen, ● (light green) anti-HIL2, ● (orange) antibody + antigen, ● (light pink) 200PBA18 + anti-HIL2 2.5 pg.ml⁻¹, ● (light yellow) 200PBZn5 + anti-HIL2 pg.ml⁻¹, ● (red) 200PBA18, ● (dark blue) 300PBZn5, ● (light blue) carbonate buffer, ● (dark purple) microscope slide. 78

Figure 25. SERS of immobilized anti-HIL2 incubated with HIL2 antigen at 12.5 pg.ml⁻¹ (a), 50 pg.ml⁻¹ (b), 200 pg.ml⁻¹ (c), 800 pg.ml⁻¹ (d), anti-HIL2 antibody (e) and normal Raman of anti-HIL2 (f)..... 80

Figure 26. PCA scatter plot of immobilized anti-HIL2 antibody (on 300PBZn5) conjugated with HIL2 at different concentrations. ● (light blue) HIL2 12.5 pg.ml⁻¹, ● (dark blue) HIL2 50 pg.ml⁻¹, ● (light green) HIL2 200 pg.ml⁻¹, ● (dark green) HIL2 800 pg.ml⁻¹, ● (light yellow) immobilized anti-HIL2, ● (orange) normal Raman of anti-HIL2. 81

Tables List

Table 1. Pre-established vitreous samples and their corresponding annealing times used during the study, with their respective characterization and application studies.....	20
Table 2. Crystalline phase of borophosphate glass precursors identified by Rietveld refinement.	35
Table 3. Glass transition temperature (T_g), degradation onset (T_x), degradation peak (T_c), glass stability (ΔT) and peak enthalpy for vitreous matrices treated with Al or Zn and their respective heat treatment time (in minutes).....	37
Table 4. Descriptive statistics (mean, standard deviation (σ), Pearson's coefficient(r)) of borophosphate glass matrices glass transition (T_g), crystallization onset (T_x) and peak (T_c), thermal stability (ΔT_{x-g}) temperatures and enthalpic variation (ΔH).....	39
Table 5. Vibrational modes presented on Raman spectra of borophosphate glasses modified with aluminum or zinc.....	45
Table 6. Vibrational modes presented on FTIR spectra of borophosphate glasses containing aluminum or zinc oxide.....	53
Table 7. Descriptive statistics (median, percentiles, median absolute deviation (MAD), quartile-based coefficient of variation (QCV), mean and standard deviation) of nanoparticle size and distance of the respective heat treatment time of each glass matrix, with calculated values for samples treated for 5 min.	59
Table 8. SERS substrate enhancement factor of each thermal treatment time calculated at three different CVP concentrations for the peak at -592 cm^{-1}	74

Abbreviations List

AgNP	Silver Nanoparticle	SRO	Short Range Order
AuNP	Gold Nanoparticle	SSEF	SERS Surface-enhancement Factor
BM	Biomolecule	UV-VIS	Ultraviolet-Visible
BO	Bridging Oxygen	XRD	X-Ray Diffraction
BSA	Bovine Serum Albumin		
CA	Capture Antibody		
CPV	Cresyl Violet Perchlorate		
CV	Coefficient of Variation		
DSC	Differential Scanning Calorimetry		
EM	Electromagnetic		
FTIR	Fourier-Transform Infrared		
HIL-2	Human Interleukin 2		
HT	Heat treatment		
IQR	Interquartile Range		
MAD	Median Absolute Deviation		
ND	Neutral Density filter		
NBO	Non-Bridging Oxygen		
NP	Nanoparticle		
PCA	Principal Component Analysis		
PI	Isoelectric point		
PSD	Particle size distribution		
QCV	Quartile-Based Coefficient of Variation		
QR	Quartile Range		
RR	Rietveld Refinement		
SEM	Scanning Electron Microscopy		
SERS	Surface-enhanced Raman Spectroscopy		
SPR	Surface Plasmon Resonance		

Symbols List

cm^{-1}	Wavenumber / Raman shift
ΔH	Enthalpic variation
ΔT	Thermal variation related to Glass stability
m	Mass
M	Molar concentration (mol/l)
N_A	Avogadro constant
nm	Nanometers
p	Statistical significance (<i>p-value</i>)
Q_1	First interquartile (or 25 th percentile)
Q_2	Median (\bar{x}) value of interquartile range
Q_3	Third interquartile (or 75 th percentile)
Q^n	Number of bridging oxygens
r	Pearson's correlation coefficient
σ	Standard deviation
δ	Bending modes
$\nu_{s/as}$	Symmetric/asymmetric stretching
T_c	Glass crystallization Peak Temperature
T_g	Glass Transition Temperature
T_x	Glass crystallization Onset Temperature
θ	Theta
x_i	Data point
\bar{x}	Median
\bar{x}	Mean

Summary

1. Introduction	1
1.1. Global Treats	1
1.2. Overall of Current Diagnostic Methods.....	2
1.3. Researches on Biomarkers Based Biosensors	4
1.4. Plasmonic Resonance in SERS	6
1.5. Types and Approaches for SERS Substrates	9
1.6. Some Applications of Glasses in Biosensors.....	11
1.7. Synthesis of Glass Matrices for Nanoparticle Growth	12
1.8. Adsorption of Biomolecule on Nanoparticle	14
2. Objectives.....	18
2.1. General Objectives	18
2.2. Specific Objectives.....	18
3. Experimental.....	20
3.1. Glass Structure and Synthesis.....	20
3.2. Glass Properties and Structural Analysis	21
3.2.1. Crystallographic analysis.....	21
3.2.2. Thermostability	22
3.2.3. Molecular structure investigation	23
3.3. Nanoparticle Morphology and Vitreous Surface Study.....	24
3.3.1. Arrangement and size investigation	24
3.3.2. Plasmon identification.....	25
3.3.3. Study of the surface plasmon resonance effect	26
3.4. Biomolecular Adsorption and SERS analysis	27

4. Results and Discussion	31
4.1. Spatial array analysis by XRD.....	31
4.2. Thermal Properties Studied by DSC.....	35
4.3. Chemical Glass Structure	41
4.3.1. Molecular evaluation by Raman spectroscopy.....	41
4.3.2. Molecular evaluation with FTIR spectroscopy.....	49
4.4. Nanoparticle Morphology by SEM	54
4.4.1. Morphology and distribution evaluation	54
4.4.2. Nanoparticles size statistical analysis from SEM data.....	58
4.5. Plasmonic Resonance UV-VIS Absorbance	65
4.6. Enhancement Factor	68
4.7. SERS Analysis of Adsorbed Protein.....	74
4.7.1. Single step incubation	75
4.7.2. Antibody immobilization.....	79
4.7.3. Discussion.....	82
5. Conclusions	85
APPENDIX A - Theoretical background	87
A.1. X-Ray Diffraction.....	87
A.2. Differential Scanning Calorimetry	88
A.3. Raman and Infrared Spectroscopies	89
A.4. Scanning Electron Microscopy.....	91
A.4.1. Statistical analysis of nanoparticle size study.....	92
A.5. Ultraviolet-Visible Spectroscopy.....	93
A.6. Surface Enhanced Raman Spectroscopy	94
References	96

Introduction

Ultrasensitive and fast detection of analytes has been, for a long time, crucial in many fields – food industry, drug discovery, environmental control and early-stage disease diagnosis, for instance.¹⁻⁴ In this respect, the use of analytes for the identification of a health condition is highly important since issues in human health are advancing constantly and so the need of new reliable detection methods for an accurate and efficient disease diagnose.

1.1. Global Treats

According to the World Health Organization (WHO), resistant bacterial infections and non-communicable diseases such as cancer were one of the greatest threats to global health in 2019.⁵ Many difficulties arise when it comes to detection, treatment and prevention of infectious diseases and cancers, partially because of the complexity of these diseases and their rapid spread (either between people or in person).⁶

The International Agency of Research on Cancer (IARC) has been updated on rates of cancer incidence worldwide and, for Brazil, the overall rate of the four most fatal types (including the ones shared amongst both sexes) have not been decreasing in the past years (**Figure 1**), not including lung cancer and prostate in male patients. In this case, rate reduction is linked to decrease in smoking rates in the past decades due to smoking conscientization, but, even so, the rates are still high.⁷ Meanwhile, the WHO released a statistical report last year describing that infectious diseases contributed the most for

differences in life expectancy in low income countries.⁸ However, mortality of patients, due to infectious disease or cancer, can be effectively reduced with early diagnosis and treatment, demonstrating that this situation requires new prevention strategies, diagnosis, treatment and/or the application of theranostic medicine.^{9,10} Within it, development of techniques associated to disease diagnosis with minimum disadvantage is required.

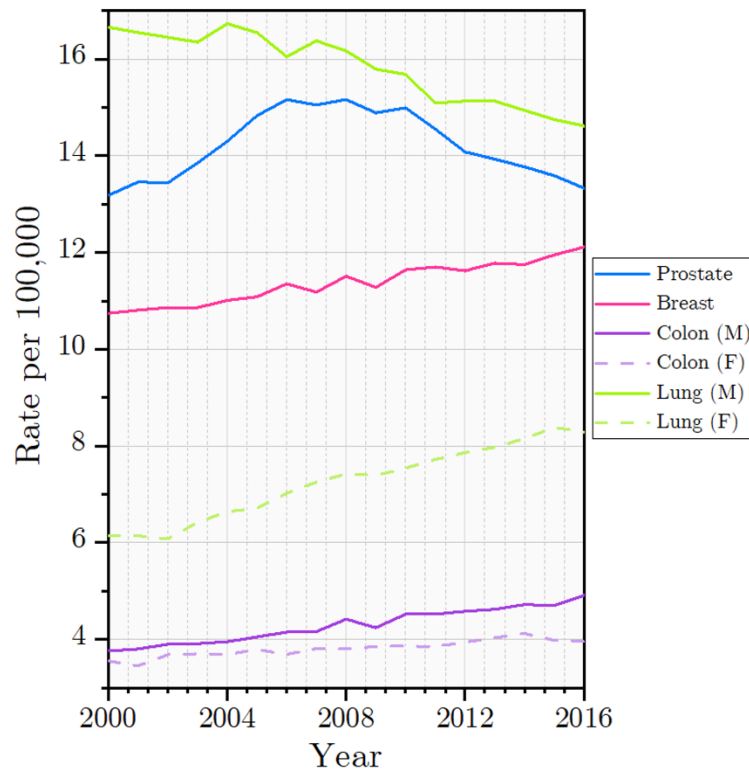


Figure 1. Cancers rate incidence (per 100,000) of prostate, breast, colon (male/female) and lung (male/female) from 2000 to 2016 in Brazil.

Data from International Agency of Research on Cancer (IARC) - WHO

1.2. Overall of Current Diagnostic Methods

Important and useful techniques used currently for diagnosis and disease therapeutics such as Enzyme-linked immunosorbent assay (ELISA), magnetic resonance imaging (MRI), computed tomography (CT), positron emission tomography (PET), polymerase chain reaction (PCR), culturing and others aids in the medical health system

with disease identification, each of them carrying their strengths and drawbacks related to sensitivity, swiftness, low-cost, portability and easy accesses, for example. ELISA, for instance, is a versatile immunological assay technique that can be used as a diagnostic tool in medical centers, and also in the analytical industries. This technique allows the user to access quality control or detect and quantify a particular antigen, with similar approaches that can be adapted for an individual purpose.¹¹ Nevertheless, target labeling demands complicated chemical processes, which can affect the biological molecular structures used in this methodology. Therefore, label-free techniques exhibit distinguish potential for analyte detection.¹

MRI, largely used in various brain disorder analysis and also often used to examine other organs abnormalities, has a major drawback related to detection and sensibility.¹¹ This advanced technique can generate images deeper into the tissue, but cannot detect entities smaller than a few centimeters or differentiate minor changes in tumor size,¹²⁻¹⁴ which can result in a tardily cancer detection, when the disease is at a more advanced stage and treatment options are considerably affected.¹⁵ CT and PET are techniques that can be complementary to each other for providing detailed description of structures and images, in which metastasis in the organism can also be identified.^{13,16} However, submitting the patient to relatively high radiation doses, it may lead to the appearance of new cancer outbreaks, not to mention that PET also has a limited resolution on the order of few millimeters.^{15,17} These disadvantages, therefore, require new strategies that are able to provide rapid diagnostics with a great sensitivity, capable of early detection that are also not aggressive/prejudicial to the patient.⁶

Infectious disease identification, on the other hand, requires different approaches, involving techniques such as ELISA and other methodologies like PCR and culturing. PCR has great sensitivity and specificity but has also limitations concerning chain reaction products, which are prone to binding and mutation errors. Additionally, as it needs isolated

genetic materials, a careful manipulation of biological sample and complex analytical instruments are also needed.^{18,19} Furthermore, even though culturing, the mainstay in clinical microbiology, is related to pathogen identification by isolated cultures, it became outdated for the study of complex microbial communities and is not totally adapted for detection of emerging fastidious bacteria.¹⁰ Within it, approaches that offer great sensitivity and specificity but are also versatile and ease do handle are then an opportunity to overcome these challenges.

Many current diagnostics, as could be seen, lack in at least one crucial criterion necessary to be considered favorable in developing nations, being them sensitivity, swiftness, low-cost, portability and easy accesses.⁶ That being the case, point of care tests (POCT) emerge as an alternative for detecting a variety of diseases-related biomarkers, enabling these technological systems to encompass the missing critical parameters of the analysis already in use, and improve overall diagnosis.²⁰

1.3. Research on Biomarkers Based Biosensors

The biomolecular network of a human being is very complex, comprising of countless micro and macromolecules that regulates biological functions.²¹ Changes in the concentration of some specific biomolecules can lead to malfunction of a cell and/or it can be the organism response against a health condition. Withing it, it is notable the use of these components for improvement of clinical care, which can include the assessment of a disease status monitored by a set of distinguish biomarkers.^{21,22} Biomarker can thus be defined as a particular component related to a normal biological process, pathogenic mechanism or response to an (external) interference.²² Different approaches for the detection of biomolecules have been under study, aiming disease diagnosis such as wearable molecular diagnostic systems,^{23,24} lateral flow assays,^{18,25} micro-fluidics assays^{20,24} and plasmonic technologies.^{18,20,25}

Detection of biomolecules based on plasmonic effects is the commonly used approach in optical sensors and is gaining an outstanding importance in the past years owing to their label-free nature, high sensitivity and great limit of detection as low as single-molecule level.^{20,27} The fundament of the plasmon resonance is based on the amplification of the electromagnetic field by association of the oscillatory electrons frequency on a metal surface with an external electromagnetic source.^{13,28} This electromagnetic resonance, at a specific wavelength, is what is known as surface plasmon resonance (SPR). Among the distinct techniques that uses SPR, surface-enhanced Raman spectroscopy (SERS) is a very wide used one as it has little interference from water and, in some cases, additional structural information can also be acquired, making SERS very suited for biological applications.^{17,29,30}

In the past few years, during Ebola epidemic, Sebba *et. al.*²⁷ published about a multiplex platform for detection of pathogen-related molecules, characterized by a particle-based sandwich immunoassay. This system is based on SERS tags and magnetic beads conjugated with specific antigen for Ebola, Lassa or malaria, latter forming a complex with the target molecule and, after magnetic separation, it allows one to access enhanced Raman spectrum information of the disease biomarkers. Nonetheless, Xiao and collaborators³¹ demonstrated that it is even possible to analyze untargeted molecules through SERS with liquid chromatography separation. This allowed the creation of a unique tumor metabolic fingerprint based on SERS spectra, enabling the detection of a tumor without knowing the identity of the component metabolites.

Moreover, Hernández-Arteaga and coworkers²⁶ investigated a colloidal suspension of a citrate-silver-nanoparticle (cit-Ag-NP) as SERS substrate for the ability of measuring the concentration of sialic acid in human saliva. Their work aimed to determine levels of this component and compare data among healthy and breast cancer patients, in which high sialic acid concentration in the saliva is related to disease presence. Using a calibration

curve, their methodology, based on mixing the cit-Ag-NP with treated saliva samples showed sensitivity of 94%, specificity of 98% and accuracy of 92%, proving to be a promising technique. It is notable that enhanced Raman signals of molecules, which can be obtained from very low particle concentrations (up to 10^{-16} M), greatly outperforms the detection limits of prevalent medical technologies.¹⁷

Some of these SERS-based sensors that focus clinical applications, nonetheless, are yet to be improved considering that, in general, point of care tests must also be simple to operate as well as suited for application in non-laboratory settings.²⁴ Furthermore, the use of non-specific biomolecules for disease identification can lead to uncertain diagnosis, since an indiscriminate biomarker can be related to more than one health condition. This implies that the use of specific (targeted) molecules may ameliorate diagnostic precision.²⁶

At last, it is important to consider that performance in a real-life situation may culminate in different results of that obtained in a bench research, and one must consider how some conditions (such as other molecules interference, sample type, storage condition, and others) may interfere in the final analysis.²⁷ Given these points, as SERS is a technique based on Raman signal enhancement through SPR effect provided by metallic nanoparticles, it is also pertinent to investigate substrate-sensitivity and limit of detection based on the enhancement effect of the probed approach.

1.4. Plasmonic Resonance in SERS

Unlike some fluorescence and absorbance techniques (such as ELISA and fluorescence microscopy), Raman spectroscopy relies on inelastic light scattering directly from an analyte, not requiring sample labeling with external dye molecules.^{32,33} However, biological specimens analyzed at low wavelength such as 532 nm often yield in fluorescence and damage/burning of sample.^{32,34} This type of analysis thus requires longer excitation wavelengths, which result in significantly Raman signal intensity loss.³⁴ To overcome this

adversity, enhancement of Raman spectra has been improved over time through surface plasmon resonance, a technique known as SERS, providing high sensitivity, resistance to photobleaching and optimization to avoid native autofluorescence of organic samples.^{32,35}

SERS, as explained previously, is based on the plasmonic resonance between an incident electromagnetic wave and a metal surface, which amplifies the field near the surface.^{32,36} For this oscillation to be in resonance, it depends on several factors such as nanoparticle size and shape, the wavelength frequency applied, the environment (i.e., air, aqueous solutions, etc.), metal type and others.³⁷

Among the metals normally used in nanoparticle studies, silver, gold and copper are widely employed in SERS applications due to their high optical properties and enhancement factors, having plasmon band lying in the visible range.^{28,38,39} AuNP, for example, have great biocompatibility, being broadly applied for detection in living cells and animals.^{28,30,40} Nevertheless, gold is a more expensive material and produces weaker SERS enhancement compared to silver nanoparticles.⁴¹ Copper nanoparticles, on the other hand, have enhancement factor compared to gold and even silver nanoparticles.^{38,42} However, since copper is easily oxidized, gold and silver nanostructures are still more attractive for optical applications.³⁹ Hence, biomolecule detection using silver nanoparticles have substantial benefits for SERS applications compared to other metals.^{36,43}

Furthermore, as shape and size of metallic nanostructure can influence plasmon resonance, an intense magnetic field at specific positions, such as the corners of nanocubes, can generate highly localized SPR (LSPR), capable of increasing the overall sensitivity of the technique.²⁸ Single plasmonic nanoparticle, nevertheless, does not provide sufficient enhancement for practical applications.³² When particles are brought close together, however, the gap between them can produce extremely vast signal enhancement, known as “hot-spots”.^{32,44} These so called “hot-spots” are regions of the nanoparticulate

colloids/substrates where the electromagnetic field is highly enhanced. These regions between metallic nanoparticles highly localize the EM field and, thus, very high enhancements are produced at these interfaces.^{29,45} Bulk metal or a smooth metallic surface can generate SPR, but plasmon dispersion results in low sensitivity.⁴⁶ Nanoparticles, on the other hand, have higher surface area and, by controlling the basic geometry and nanoparticle distance, it is possible to achieve extremely large sensitivity because of the spatial confinement of the plasmon mode in the narrow gaps between particles.⁴⁷

Matteini and collaborators²⁹ produced a standardized Ag nanocube suspended in physiological pH, in which the tips of the cubes worked as “antennas” for the plasmonic resonance, presenting plasmon band at 455 nm and electric field around 22 V.m⁻¹. With this very specific location for enhancement, the EF_{\max} obtained by the authors were around 10⁵, not much higher than the average reported on the literature, possibly due to the small and isolated areas for the LSPR. The EM fields presented on the nanostructure surface are immensely pronounced on sharp edges or vertices, but the high field strengths at these regions diminish rapidly with distance from the particle surface.¹⁷

Additionally, Lu and colleagues³⁶ developed a silver nanostructured substrate with particles ranging from 46.5 to 75.8 nm. They observed that with increase in nanoparticle size, the plasmon band red shifted and a decrease of interparticle spacing was also observed from 15 to 1 nm respectively. This resulted in an increase in electric field increment from 5.7 to 40.7 V.m⁻¹, with enhancement factor estimated to be 3.10⁶. This indicates that strong electric fields can be obtained when interparticle distance decreases, producing powerful hot-spots. However, since these regions comprise smaller areas compared to the neighboring metallic surface, the chances of a molecule adsorbing at a hot-spot are narrow.⁴⁸ In colloidal nanoparticles, the aggregates are responsible for forming these hot-spots (when no sharp structure is adopted), but this leads to poor reproducibility of signal enhancement, since aggregation is not completely controlled.²

Regardless of this, the higher the enhancement, the lesser the nanogap will be, which lowers the probability to find the hot-spot.³² Thus, hot-spot regions will only be found in a small portion of the whole SERS substrate. According to this, different SERS substrates have been developed aiming the obtention of good hot-spot regions for great sensitivity and limit of detection.

1.5. Types and Approaches for SERS Substrates

Metal colloids and structural solid substrates are the most used approaches to obtain SERS effect and they differ mostly in the arrangement of nanoparticles. They have been developed with the purpose of improving the Raman signal enhancement based on hot-spots, with techniques such as silver mirror reaction,³⁶ spin-coating,⁴⁹ lithographic systems,⁵⁰ nanoimprinting⁵¹ and self-assembly.⁵² This variety of systems for nanoparticle obtention aspire the best SPR response, each having its own singularity since metal type, configuration, morphology and arrangement of nanoparticles can influence in the plasmonic resonance effect. These characteristics regulate both collection efficiencies of signal and detection sensitivities in SERS, hence distinct techniques can be applied resulting in a different nanoparticle configuration and different signal enhancement outcome.^{36,53}

Within it, a number of these mechanisms are using cellulose based substrates for nanoparticle assembly as cellulose provides a unique three-dimension cross-linked porous structure that lead to a wide hot-spot region following (controlled) silver deposition.^{36,54–57} Lu and collaborators³⁶ recently demonstrated the efficiency of a cellulose based nanofiber structured with silver NP for detecting Rhodamine 6G at concentrations as low as 1×10^{-16} mol.l⁻¹ (depending on NP size). They also reported that large silver particles aggregates formed with prolonged reaction time resulted in a reduced number of hot-spots and signal

intensity. Therefore, some difficulties arise when taking into account reproducibility and SERS signal homogeneity along the substrate.⁵⁴

Providing that, different strand materials can also be employed for SERS based on standardized techniques, such as optical fiber with lithographic systems. Quero *et. al.*⁵⁰ applied nanosphere lithography to obtain regular polystyrene nanoparticles covered by thin gold film at the fiber tips and was able to achieve an enhancement factor of 4×10^5 . This approach gives a substrate with very high periodicity and proper enhancement factor. However, this technique requires the use of sophisticated equipment and is time consuming. Furthermore, for colloidal nanoparticles acquisition, some of the techniques include the use of sodium citrate (i.e. Lee-Meisel method)⁵⁸, which produce nanoparticles with great Raman signal enhancement.⁵⁹ But it can result in signal interference from some of the citrate or other capping agents, which disturbs the desired analyte vibrational mode obtention.^{57,60} Therefore, “clean” techniques for obtaining NP are important strategies to avoid adulteration of the SERS signal.

Notwithstanding, the challenges regarding the facile fabrication of these substrates with a high spectroscopic performance remains difficult and costly for routine SERS detection. An explanation to that concerns the substrates and techniques requirement for advanced apparatus, while they occasionally provide good sensitivity and signal homogeneity/reproducibility.⁵² An alternative for metallic nanoparticle assembly is by using glassy materials, in which a diverse number of approaches can be used for obtaining good standardized nanoparticle aiming SERS substrates.^{38,61,62} Additionally, metallic glassy substrates possess good mechanical properties, making them easy to be conserved and durable in applications.⁵¹

1.6. Some Applications of Glasses in Biosensors

Among the SERS solid substrates, glassy materials are an alternative for obtaining reproducible highly sensitive metallic nanoparticles for Raman signal enhancement, as it can present high-density hot-spots, satisfactory uniformity, signal reproducibility, high enhancement factors and low fabrication cost, depending on the approach for NP obtention.^{51,62–64} Liu and collaborators,⁵¹ for instance, used nanoimprinting to produce metallic glass array nanowires as an easy, rapid, environmentally and economically favorable method to prepare air-stable SERS substrates. The uniformly distributed nanowires presented plentiful hot-spots between the nanowire tips, with an overall enhancement factor of 1×10^5 when analyzing Rhodamine B.

Conversely, Solís and coworkers⁶² studied SERS effect of nanoparticles submonolayers by drop-coating colloidal solution on a glass substrate. They obtained planar and highly uniform NP monolayers on glass surfaces and could observe that SERS efficiency of nanospheres and nanorods outgrowth with increasing neatly/tidily surface coverage, which can be explained by an accumulation of hot-spots on these substrates. Furthermore, a distinct approach using glass as a SERS substrate was applied in a study performed by Schneider *et. al.*,⁶⁴ where they used a distinct NP growth process, based on a bottom-up approach, to obtain nanoparticles at the glass surface. This mechanism is based on vitreous doping with a noble metal while producing the glass melting. They could obtain silver based nanostructures from an active glass matrix using thermal treatment under a reductive atmosphere, with overall 1×10^5 enhancement factor.

Owing to this, the importance of glasses in SERS applications is remarkable and prominent, since it possesses improved durability, enhanced signal reproducibility, abundance in hot-spots, satisfactory uniformity, high enhancement factors and low fabrication cost.

1.7. Synthesis of Glass Matrices for Nanoparticle Growth

Recently, the synthesis of doped glasses for nanoparticle assembly (through bottom-up approach) have been demonstrated by researches to be a compelling SERS substrates.^{38,64–66} As it is, the process of glass fabrication can be better understood in order to elucidate the mechanism of nanoparticle formation.

The traditional definition of the word “glass” is related with molten inorganic products that have been cooled to a solid state without crystallizing, maintaining its liquid nature in a rigid condition.⁶⁷ In general, for one to obtain a vitreous substrate, glass network formers such as borate, silicate, phosphate, borosilicate and borophosphate must be used as they can form a highly connected three-dimensional amorphous chain.⁶⁸ If an oxide, like Na_2O , is added to the glass during its fusion process, a bond in this network is broken and the sodium ion becomes part of this structure. These types of oxides are known as modifying agents, and their addition are useful to reduce the matrix viscosity and to grant more chemical resistance since they depolymerize the lattice and reduce the glass transition temperature.

For example, phosphate glasses are composed basically of PO_4 tetrahedra units linked through covalent bridging oxygens (BO), while the basic units of borate glasses are trigonal BO_3 .^{69,70} The addition of modifiers to each glass network will result in depolymerization of phosphate glasses, as the introduction of an oxygen from the modifier oxide forms negative non-bridging oxygen (NBO) sites. Controversially, it increases the polymerization degree of borate glasses, changing the boron coordination number from trigonal to tetrahedral (BO_3 to BO_4). Additionally, the charge of these NBO formed during depolymerization is compensated by the positive modifier cation.⁷¹

After fusion, these metallic and non-metallic elements (mostly oxides) can turn into glass only under critical cooling rates, in which they maintain their amorphous spatial structuring like that of a liquid (can also be referred as a super cooled liquid).⁶⁷ The

definition of a glass can thus be summarized as a thermodynamically and kinetically stabilized liquid but in a non-equilibrium amorphous solid state.⁷¹ In addition, differently from crystals, the atomic arrangement of the vitreous structure has no periodicity over space, but they can be considered to have a short-range order (SRO).⁷² However, with the addition of modifying agents in high concentrations, the matrix can become extremely fluid, facilitating the formation of crystalline structures in the matrix and increasing the long-range order (LRO) of the three-dimensional network, which is generally not desired.⁶⁸ Nonetheless, it is possible to control crystal nucleation with temperature, or with concentration of former and modifier oxides.

Among the oxides considered good glass forming agents, phosphate oxide have been earning attention due to its remarkable functional properties as a glass, such as low viscosity, high thermal expansion and low refractive index for instance, which make them excellent candidates in optical applications.^{73,74} Nevertheless, pure phosphate glasses have low chemical durability with low aqueous corrosion resistance, but they have an important advantage that includes the ability to incorporate high concentrations of transition metal ions and still remain amorphous.^{74,75} Thus, modification of the pure phosphate glass matrix with other glass formers, such as B_2O_3 , helps in improving chemical durability as well as thermal and mechanical stability.^{74,76} The further addition of trivalent and divalent oxides thus helps improving its resistance and borophosphate glasses, modified with ZnO or Al_2O_3 , have already been demonstrated to have great chemical stability and low hygroscopicity.^{65,66,71}

The addition of modifiers depolymerizes the borophosphate network by forming NBO as the glass structure also becomes more open.⁷⁷ This, in turn, favors cation mobility within these formed free paths and, under certain temperature conditions (annealing), metallic dopant ions, such as $AgNO_3$, can be reduced on the glass surface and form

nucleation sites for nanoparticle growth.^{65,75} A reductive atmosphere, such as hydrogen, can hence produce Ag⁰ nanoparticles that size can be controlled with annealing time.^{64–66}

Withing it, these metallic nanostructures formed at the outer side (surface border) of vitreous matrix can serve as “antennas” for enhancing Raman signal through plasmon resonance effect. Furthermore, since SERS effect of a particular molecule arises only close to the metallic surface (due to SPR range), it is pertinent to investigate the analyte interaction with nanoparticles along with test-sensitivity (related to the response of a molecule to Raman) and limit of detection (associated to molecular concentration) of the probed approach.

1.8. Adsorption of Biomolecule on Nanoparticle

The enhancement of the Raman signal of a molecule by surface plasmons generally occurs at close proximity of the nanometallic surface.²⁰ Given that, some chemical and/or physical mechanisms are associated in this bioconjugation to efficiently adsorb biomolecules onto the nanoparticle surface.

SERS immunoassays requires surface modification of the metal nanoparticles with target-specific antibodies in order to be able to precisely identify the desired analyte. This discriminatory mechanism based on antibodies adsorption rather than direct analyte interaction is very pertinent as it is based on biospecific recognition, offering great selectivity.³⁷ It can be accomplished by antibody binding to the silver surface through their amino acids, forming complexes with the silver.⁷⁸

Providing this, several potential adsorption strategies can be employed, either by relying on chemical or physical interactions, to analyze a biomarker via SERS. Chemical process (stronger, rely on covalent bonds) requires functionalization of NP by using, for example, chemisorption via thiol derivatives and bifunctional or mediator linkers.⁴⁰

Physical process (weaker, but very abundant), on the other hand, relies on non-covalent interactions such electrostatic attractions.⁷⁹

Formerly, in vivo or in living cells applications, colloidal nanoparticles are typically preferred due to its practicality in administration as they are already suspended in a solution.⁴¹ For these types of nanoparticles, surface functionalization (alteration of the exterior nanoparticle characteristics – charge, presence of linkers, etc.) is commonly used not only for targeting a specific molecule or cell but also to improve NP stability, increase cellular uptake, depress immunogenicity, decrease aggregation, among others.⁴⁰ Chemical functionalization of these nanoparticles are thus a routine mechanism employed in biological analysis. In consequence, the use of immunosorbent sandwich approach for biomolecule detection is frequently applied with the use of Raman active dye molecules or use of another functionalized colloidal nanoparticle solution to produce satisfactory SERS.⁴⁴ Nonetheless, the electromagnetic enhancement of the analyte signal decays exponentially with the distance formed, after functionalization, between nanoparticle surface and desired biomolecule, drastically reducing SERS effect.⁸⁰

Furthermore, some SERS based methodologies benefit from the signal of another Raman active molecule (similar to ELISA approach), in which the intensity of the Raman reporter collected is directly related to the concentration of the desired analyte. Chuong and colleagues,⁸¹ for instance, presented a SERS-linked sandwich assay based on two Raman tags, one linked to a gold film surface and another linked to gold nanoparticles. They aspired in detecting thrombin without a false-positive result, so only read-out signals containing both Raman reporter spectra were indicative of the presence of thrombin. This (sandwiched) approach, however, requires the stabilization of the colloidal nanoparticles to avoid nanoparticle aggregation which may interfere in the analysis and, since the hot-spots formed are only achieved if there is a conjugation between targeted film and nanocolloids, three false-positives can occur: SERS from defected thin films, from

nanoparticle aggregates or from protein mediated binding “errors”.^{44,81} Additionally, some analysis, based on a colormap result, can culminate in false color result since it is difficult to achieve homogeneous distribution of SERS NP aggregates on the surface. All these protracting methodologies, with oodles steps and difficulties, are an impasse for an efficient point-of-care test.

Solid SERS substrates, on the other hand, do not necessarily demand surface functionalization for nanoparticle stabilization or particle aggregation reduction, which cooperates for direct biomolecule adsorption. Ionic interactions depend on the attraction of the amino acid groups (in a non-zwitterionic state) with opposed charged ions presented on the metallic molecule of interest. The difference in a pH solution enables the adjustment of the protein net charge without the need of previously functionalize the nanoparticle surface with a specific charge. So, if the surface of interest is positive, the biomolecule can be protonated in an acidic buffer to enable ionic interactions, not previously possible if considering physiological conditions.

However, when it is indeed crucial and used (especially when the substrate is not nanostructured), some strategies are necessary to be considered in order to intensify the SERS signal as signal enhancement decay with distance rise.⁸⁰ As an example, the use of functionalized thin-films of gold (AuTF) and gold nanospheres (AuNS) with dithiol can be configured in such a way that the gap distance between the region of interest surfaces is set by the length of the adsorbed molecules.⁸² Good enhancement factors can be achieved with a functionalized sandwiched between AuTF-AuNS, in the order of 6.4×10^6 . But this approach, consequently, has a gap distance, nanoparticle size and sandwich configuration dependency, which makes reproducibility difficult.⁸²

Developing a scenario in which physical interactions can be further exploit offers a breakthrough for a methodology simpler to reproduce. Processes such as (i) ionic interactions between the charged nanoparticles surface and the opposed charged antibody

residues, (ii) hydrophobic attraction between biomolecule and NP surface and (iii) dative binding between conductive electrons and sulfur atoms of antibody amino-acids describe the spontaneous adsorption of antibodies onto nanoparticle surfaces.⁴⁰ Thus, the antibody structure plays an important role when relying on physical means for molecule adsorption. However, a major drawback of this strategy is the necessity of high antibody concentration, random orientation and replacement by other molecules in biological samples.^{40,83}

Even though, (free) immobilization (without the use of chemical linkers) of proteins onto a metallic nanoparticle surface can also offer single molecule detection limits, similarly to results found with functionalization.⁸⁴⁻⁸⁶ It is important to consider, however, that some immobilization strategies already studied counted on citrate stabilized gold nanoparticles (facilitating protein interaction), with extreme long incubation time (>15 h).^{59,84}

Withing it, biomolecule conjugation offers additional difficulty in SERS study by affecting the quality and easiness of analysis. Hence, extending the comprehension and capability of antibody adsorption, based on physical methods, can advance the development of practical methodologies to be applied in a rapid and simple way analysis. Notwithstanding, despite of all the different substrates for SERS applications that have been developed or are in-development, an analysis of the literature leads us to come to one main conclusion: Albeit the several qualities these substrates present, to the best of our knowledge, they lack at least one crucial criterion to be considered a great point-of-care diagnostic tool, such as sensitivity, low-cost, portability, easy access and important aspects like facile fabrication, resistivity, high spectroscopic performance, reproducibility and easy assembly.

As previous shown, glass substrates with self-assembled nanoparticles possesses great potential to overcome these attributes, since they are reasonably easy to obtain, with overall cheap procedures, with great SERS effect, are resistant and offers good signal reproducibility.^{38,64,65,87}

Objectives

2.1. General Objectives

Explore the use of two borophosphate glass matrix as a self-supported silver nanoparticle substrate for SERS application, one modified with aluminum oxide (Al_2O_3) and another with zinc oxide (ZnO). Our aim is thus to identify the main differences between both vitreous matrices under thermal treatment and how they respond to the SERS effect based on the different nanoparticle sizes obtained at each annealing time. The hypotheses investigated thus considered whether the nanoparticles growth offers dissimilarities in glass matrices and if the enhancement ability as a SERS substrate is superior to the overall found in the literature. Furthermore, protein analysis was also investigated in order to better elucidate whether biomolecule detection is possible and which method (between long or short incubation, and in the presence or not of buffer solution) would be best suited to employ in our vitreous substrate.

2.2. Specific Objectives

- I. Characterization of glass matrices and silver nanoparticles according to the adopted annealing time by accessing:
 - Crystallographic/amorphous profile
 - Thermostability
 - Structural conformation
 - Nanoparticle dimension and morphology
 - Plasmonic resonance effect of metallic nanoparticles

- II. Examination of SERS performance with overall enhancement factor in respect of a standard molecule
- III. Study of the performance of our vitreous substrate in detecting biomolecule based on three direct approaches for biomolecule adsorption with: protein solution in water (free of possible salt interference) and protein under simulated biological conditions (buffers); based on:
 - Single step for protein adsorption (short incubation)
 - Protein immobilization (long incubation)

Experimental

The techniques employed in this study are summarized in **Table 1**, and theoretical information regarding each of them can be accessed in Theoretical Background (**APPENDIX A**).

Table 1. Pre-established vitreous samples and their corresponding annealing times used during the study, with their respective characterization and application studies.

Sample	HT Time (min)	Characterization						Application	
		XRD	DSC	Raman	FTIR	SEM	UV-VIS	SERS (CVP)*	(BM)**
200PBAI	0	•		•	•		•	•	
	2		•	•		•	•	•	
	5	•	•	•		•	•	•	
	8		•	•		•	•	•	•
	12	•	•	•	•	•	•	•	
300PBZn	0	•		•	•		•	•	
	2		•	•		•	•	•	
	5	•	•	•		•	•	•	•
	8		•	•		•	•	•	
	12	•	•	•	•	•	•	•	

* Cresyl Violet Perchlorate** Biomolecules

Source: Self-elaborated

3.1. Glass Structure and Synthesis

Borophosphate glasses were fabricated (by collaborators) adopting (in mol%) the $\text{NaH}_2\text{PO}_4\text{-HBO}_3\text{-Al}_2\text{O}_3\text{/ZnO}$ glass template, in which NaH_2PO_4 and HBO_3 ratio was set at 2, Al_2O_3 or ZnO were added in a proportion of 20% (10% Al_2O_3 and 20% ZnO). Samples were also doped with AgNO_3 , added at 3%, and all reagents used were of high purity (Aldrich Co.). The melting-quenching technique applied is described previously by

Schneider,⁶⁴ where the synthesis used 5 g of the above-mentioned reagents, homogenized by an agate mortar. The mixture was then transferred to a covered Pt/Au crucible and fused at 1050 °C for 1h and, posteriorly, glasses were quenched to the room temperature in a graphite mold.

Thermal post-treatment was applied (by collaborators) for growth of nanoparticles (bottom-up process),^{38,64,65} in which Ag⁰ nanolayer was obtained at 200 °C for aluminum matrix and at 300 °C for zinc matrix, under an hydrogen atmosphere for 2, 5, 8 and 12 minutes. A constant flow of 50 ml.min⁻¹ was applied during the bottom-up process. Samples were stored in a dissector under vacuum until analysis. The nomenclature of samples was designated as 200PBA t or 300PBZn t , where 200 or 300 represents the temperature used during the annealing process (in °C), P = NaH₂PO₄, B = HBO₃, Al/Zn = Al₂O₃/ZnO and t = 0, 2, 5, 8 or 12 (depending on the amount of thermal treatment time applied, in minutes).

3.2. Glass Properties and Structural Analysis

3.2.1. Crystallographic analysis

The crystallographic structures of vitreous borophosphate matrix were studied by x-ray diffraction technique (XRD). The crystallinity patterns were obtained by a Miniflex diffractometer 600 (Rigaku, Japan), with a Cu K α radiation (1.541 Å) at 40 kV and 30 mA. Data were collected from 10 to 90° 2θ , with a step size of 0.02° min⁻¹. For the analysis of XRD patterns, experimental diffraction patterns have been normalized. Additionally, in order to identify the possible phases of the glass samples, XRD of the glass precursors (NaH₂PO₄, H₃BO₃, Al₂O₃ and ZnO) were also collected. A Rietveld refinement of the precursors were conducted in the Miniflex diffractometer 600 software for crystalline phase identification and further comparison with vitreous diffraction patterns.

3.2.2. Thermostability

Vitreous state of 200PBA12-12 and 300PBZn2-12 samples were studied by thermal analysis known as differential scanning calorimetry (DSC). The glass transition temperature (T_g) measurements were achieved by DSC-60 Differential Scanning Calorimeter (Shimadzu, Japan). Samples were ground to a thin powder using agate mortar, with 5 to 10 mg of each being placed into sealed aluminum crucibles and analyzed under a constant nitrogen flux of 50 ml.min⁻¹ with applied heating rate of 10 °C min⁻¹ ranging from 30 to 600 °C. A baseline was run under a flowing nitrogen atmosphere using a reference empty aluminum crucible.

For this current work, the adopted definition of T_g considered the onset value. The glass degradation onset (T_x) was determined similarly, taking the intersection of tangents from the baseline and the initial slope of the peak. And finally, the determination of degradation peak (T_c) considered the midpoint of its maximum value, while the area under the peak provided the latent heat (enthalpy) of degradation (See A.2 of APPENDIX A for further comprehension).

To further investigate the association of thermal analysis and annealing time, a correlation analysis was investigated for each sample set. No normality test was assumed, since sample size number is not sufficient to express significance. Pearson's correlation coefficient was then chosen as it measures the association, that is, the tendency of the variables to lie on a straight line, considering the following equation:

$$r = \frac{\sum_{i=1}^n (x_i - \bar{x}) * (y_i - \bar{y})}{\sqrt{\sum_{i=1}^n (x_i - \bar{x})^2 * \sum_{i=1}^n (y_i - \bar{y})^2}}$$

Eqn. (1)

Which consider the variation of data from the mean (\bar{x} and \bar{y}) divided by its variability.⁸⁸

3.2.3. Molecular structure investigation

In this sense, chemical structure of vitreous substrates was evaluated by normal Raman analysis, conducted on a LabRAM HR Evolution (HORIBA Scientific) coupled with a CCD detector. A 532 nm line with CW Argon ion laser was used, with a 50x objective and optical intensity was kept at 100% laser power. All samples were analyzed at room temperature and with Raman shift ranging from 150 to 1800 cm^{-1} . All borophosphate matrices (Al200 °C, Zn300 °C) at all different treatment times (0, 2, 5, 8 and 12 min.) were analyzed. Samples were not polished or pre-treated, having whole fragments selected.

Raman analysis was complemented with Fourier transform infrared (FTIR) spectroscopy, with spectra collected in a Shimadzu IRPrestige-21 spectrometer (IRPrestige-21 model). Data were obtained at room temperature, with wavenumbers ranging from 4000 to 400 cm^{-1} and spectra given in transmittance percentage vs. wavenumber. For this analysis, only one annealing time per matrix was selected, being it the maximum treatment time (12 min), along with samples without thermal treatment (0 min). Fragments were first dried for 40 minutes at 60 °C and then grounded to thin powder, with an agate mortar, previous to pellet preparation. Sampling preparation used potassium bromide (KBr) (pre-dried for 12 hours at 100 °C) and powdered glass samples at a ratio of 0.1% (m of KBr/m of sample), vigorously mixed in an agate mortar. The 13 mm pellets of the KBr/sample mixture were assembled with an applied pressured of 60 psi for 30 seconds, and pure KBr pellet was used for baseline correction.

All Raman and FTIR spectra were baseline corrected (constant at minimum value) and normalized to the band with maximum intensity. Deconvolution of spectra was carried out in order to identify all peak contributions related to vibrational modes of the chemical glass structure. For spectra plotting, baseline correction based on a second order polynomial fitting and Loess smooth signal process were performed.

3.3. Nanoparticle Morphology and Vitreous Surface Study

3.3.1. Arrangement and size investigation

All glass samples (200PBA1/300PBZn) at all annealing times (2-12 min), with exception of 300PBZn5, had their nanoparticle size and shape assessed by scanning electron microscopy (SEM) technique. The images were recorded using a Quanta FEG 250 Scanning Electron Microscope, with platinum and gold coating performed at 40 mA for 60s. In general, 201 nanoparticle counts, for each HT time and matrices, were considered for area calculation of thresholded images where clearly isolated nanoparticles were used in the counting. Thresholded nanoparticle images that appeared coalesced together were not included for the area calculation or were manually separated (when associated by just few pixels), as these samples could bring size dispersion to higher values erroneously. It must be considered that, since SEM images gives a superficial representation of the glass surface without perspective or depth notion, area rather than volume was the adopted strategy for size evaluation, with further diameter measurement.

The average nanoparticle size was calculated based on the Shapiro-Wilk test, used for assessing normality of data previously the statistical analyses. The dispersion or variability of data (deviation of data from the median value) was calculated by the median absolute deviation (MAD), a more robust alternative (for nonparametric data) compared to the standard deviation method, with the following equation:

$$\text{MAD} = \text{median} (|x_i - \bar{x}|)$$

Eqn. (2)

Which considers the absolute deviation of data from the median. Additionally, the average uniformity of a particle was calculated by the median coefficient of variation (CV), known as an estimate of the particle size distribution (dispersity) in its environment.⁸⁹

This coefficient is defined as 100 percent times the standard deviation (σ) of the particle diameter distribution divided by the mean (\bar{x}) particle diameter.^{88,89}

$$CV = \frac{\sigma}{\bar{x}} \times 100$$

Eqn. (3)

This equation is applied for normal distributed data, where mean and standard deviation provide enough useful statistical information. However, when the data is not normally distributed, this coefficient can be estimated based on the IQR from a median calculation, and this measure is given by the quartile-based coefficient of variation (QCV).⁹⁰

$$QCV = \frac{(Q_3 - Q_1)}{Q_2} \times 100$$

Eqn. (4)

Where Q_1 is the 25th percentile, Q_3 is the 75th percentile and Q_2 is the median (\bar{x}) value in the interquartile range. The QCV was then applied for the investigation of nanoparticle size dispersion. Further explanations about this statistical analysis can be accessed in **A.4.1 of APPENDIX A**.

3.3.2. Plasmon identification

The qualitative analysis of silver nanoparticles was evaluated by ultraviolet-visible (UV-VIS) spectroscopy with a UV-3600 UV-VIS-NIR Shimadzu spectrometer, operating from 400 to 4000 nm and with a resolution of 1 nm. The technique allows the assessment of surface plasmon resonance (SPR) bands of metallic nanoparticles bigger than 2 nm by analyzing the absorption band resulting from the interaction of the electromagnetic wave and the free electrons of the surface silver nanoparticles (refer to A.5 APPENDIX A for further comprehension). Data was collected for both glass matrices without annealing time and for each thermal treatment time under study. This analysis used whole fragment, held

onto a barium sulphate sample holder and fixed with a double face adhesive tape, maintaining the most reflective side of the sample upwards.

3.3.3. Study of the surface plasmon resonance effect

A more refined surface-sensitive technique than Raman, known as surface-enhanced Raman spectroscopy (SERS), was employed to investigate the potential of nanoparticles in boost molecular signal. For SERS, data analysis was performed similarly to Raman spectroscopy as previously mentioned.

The well-known Raman reporter Cresyl Violet Perchlorate (CVP) (Sigma Aldrich) was used for SERS surface-enhancement factor (SSEF) calculation by reasons of the molecule be positively charged and contain extensively delocalized p-electron systems (3–4 phenyl rings),⁹¹ thus, being sensitive for Raman and SERS. Standard stock solution was prepared at 1 M using ethanol 98% (Sigma Aldrich). Further dilutions at 10^{-3} and 10^{-6} M were performed, and all solutions were stored at room temperature (final molar concentrations may have suffered minor alterations due to solvent volatilization in the process of solubilization and analysis).

Borophosphate glass matrices, modified either with zinc or aluminum, were selected for all annealing time (0, 2, 5, 8 and 12 minutes). A total volume of 0.5 μ L from the respective CVP concentrations were applied on top of each glass sample under study. Normal Raman signal of CVP was acquired with laser power at 100% (no ND filter), and SERS signals of vitreous substrates were acquired with laser power at 1% (ND2) to avoid signal saturation from the CCD detector.

For standardization of peak intensity analysis, Lorentzian function was used to access intensity of the most prominent peak subsequently baseline subtraction by polynomial fit.

3.3.3.1. Descriptive data of enhancement factor

The estimate of the SERS substrate enhancement factor (SSEF) of our borophosphate glass matrices adopted, in this work, the following equation as reported by authors,^{38,48,51,92}

$$\text{SSEF} = \frac{I_{\text{SERS}}/N_{\text{SERS}}}{I_{\text{RS}}/N_{\text{RS}}}$$

Eqn. (5)

where I_{SERS} and I_{RS} are the intensities obtained from SERS and normal Raman spectra, respectively, N_{SERS} is the average number of adsorbed molecules in the scattering volume for SERS measurements and N_{RS} is the average number of molecules in the Raman scattering volume. Considering that the probed molecules are uniformly dispersed on the substrates, it is possible to estimate the number of probed molecules contributing to the signal by

$$N = N_{\text{A}} \times M \times \frac{V_{\text{droplet}}}{A_{\text{spot}}} \times A_{\text{laser}}$$

Eqn. (6)

where N_{A} is the Avogadro constant, M is the molar concentration of the used CVP solution, V_{droplet} is the volume of the CVP droplet, A_{spot} is the area of the spot formed by the CVP droplet and A_{laser} is the area of the laser spot.

3.4. Biomolecular Adsorption and SERS analysis

Biomolecule conjugation on the nanoparticle surface focused on physical rather than chemical interactions, to prevent nanoparticle and/or glass properties adulteration. It was considered that antibodies can efficiently adsorb on the nanoparticle surface via electrostatic interactions when at their isoelectrical point.⁹³

For this experiment step, vitreous sample selection followed previous SERS results with CVP, culminating in the use of 200PBA1 and 300PBZn at annealing times of 8 and 5 min respectively. No sample pre-processing was adopted, and whole fragments were arbitrary selected based on size (bigger than 2 mm). Bovine Serum Albumin (BSA) and anti-Human Interleukin 2 (HIL-2) were the proteins selected for biomolecule SERS analysis, with the intention to investigate the coating efficiency of proteins, prepared as described above.

Firstly, BSA was used as a proof-of-concept protein for SERS label-free biomolecule detection. Albumin Standard fraction v (Pierce), at initial concentration of 2 mg.ml⁻¹ (3x10⁻⁵ M) in a 0.9% aqueous NaCl solution, was serially diluted to 1x10⁻⁶ M and 1x10⁻⁹ M with ultrapure water and stored at room temperature. SERS spectra were recorded using each dilution, corresponding to [BSA] = 66 µg.ml⁻¹ and 66 ng.ml⁻¹ respectively.

Purified anti-Human IL-2 antibody (anti-HIL2) (MQ1-17H12/ELISA MAX™ Deluxe Set Human IL-2) was used to investigate antibody interaction with silver nanoparticles and biomolecules sensitivity under simulated biological conditions (buffers). Two step dilutions were applied. First, stock solution of anti-HIL-2, at initial concentration of 0.5 mg.ml⁻¹ (3.25x10⁻⁵ M), was diluted at a final concentration of 2.5 µg.ml⁻¹ with standard carbonate buffer (Biolegend) and stored at 4 °C. Second, Human-IL2 antigen (ELISA MAX™ Deluxe Set Human IL-2) was serially diluted in concentrations of 800 pg.ml⁻¹, 200 pg.ml⁻¹, 50 pg.ml⁻¹ and 12.5 pg.ml⁻¹ with PBS standard solution A (Biolegend).

Subsequently, two approaches were tested for protein immobilization: (i) ambient drying with short incubation; (ii) ambient drying with long incubation.

(i) Short incubation

A droplet of each protein solution (BSA and anti-HIL2 in carbonate buffer) from their respective dilutions, in a volume of 0.05 µl, was poured on top of the most reflective side of each vitreous sample. In addition, a mixture between antigen-antibody (1:1 v/v)

solution from the highest antigen dilution was also included. A quick incubation of 20 min were allowed, at room temperature. Solutions were set aside to dry spontaneously at room temperature. Enhanced Raman signal was collected right after samples were completely dried, at 532 nm laser line, with acquisition time of 15 s and 3 accumulations. Laser power was attenuated to 5% to minimize photoinduced and thermal effects.

(ii) Long incubation

For protein immobilization, incubation process was adapted from ELISA MAX™ Deluxe Set Human IL-2 protocol (Biolegend). This step was applied just for anti-HIL2, with 200PBA18 and 300PBZn5 samples. Five of each vitreous sample were incubated with 200 µl protein solution (2.5 µg.ml⁻¹) for 90 minutes, at 37 °C. After incubation, samples were washed with PBS, and 4 fragments were re-incubated with the four-fold serially diluted Human IL-2 antigen, ranging from 800 pg.ml⁻¹ to 12.5 pg.ml⁻¹, for 1 hour, at 37 °C. SERS analysis were performed immediately after each incubation, recorded using acquisition time of 15 seconds, with 3 accumulations, and laser power kept at 5%.

Spectra investigation was performed based on a multivariate analytical method. Principal Component Analysis (PCA) was selected due to its power to reduce data, highlight spectroscopic variations and obtain meaningful patterns by maximizing the covariance of spectral information via principal components (PCs).^{3,60} It is based on the reduction of a set of variables into smaller sets of (orthogonal) independent principal components in the direction of its maximal variation.⁹⁴ In other words, it reduces the dimensionality of data while retaining the most significant information for further analysis. The principal component one (PC1) demonstrates the maximum variance in the data, and the second (PC2) illustrates the largest residual variance, and so the other principal components (PC3, PC4...) and they are completely uncorrelated and independent. But the higher-order PCs are progressively more related with noise, leaving no further scope for

dimensionality reduction.⁹⁴ The data will then have its variance explained (in %) by the plot of, at least 2 components.

Additionally, pre-processing techniques are essential to remove background signal and noise, in order to ensure that the analysis is based on the Raman measurements and not on other artifacts.⁹⁵ That being the case, the baseline corrected spectra (with second-derivative polynomial fit) was smoothed by Savitzky–Golay at a polynomial order of 5, and spectra was further normalized previous to PCA analysis.

Results and Discussion

4.1. Spatial array analysis by XRD

According to Zachariasen, a glass can be defined as a non-crystalline (or in an amorphous state) material that is absent of periodicity and symmetry but is not entirely random, thus having a short-range order (SRO).^{96,97} Furthermore, phosphate glass matrices have low chemical durability and, therefore, the addition of B_2O_3 is important to increase the overall substrate resistance. The further combination of these forming agents (P_2O_5 and B_2O_3) with modifying agents (i.e. Al_2O_3 and ZnO) contribute to decrease the borophosphate matrix hygroscopicity, important for some biological applications.^{38,65,87} However, an increased amount of modifiers can lead to formation of crystalline phase (or LRO) in the lattice. That being the case, the examination of the atomic arrangement of 200PBA1 and 300PBZn samples before and after thermal treatment was achieved by X-ray diffraction (XRD) in order to identify if the substrates had or developed any crystalline phase during matrix fabrication and nanoparticle growth process.

The normalized XRD patterns are presented in **Figure 2** and it exhibits a broad diffuse diffraction pattern in the range $20^\circ \leq 2\theta \leq 40^\circ$ and some residual (weak) peaks being observed at $2\theta = 27.7^\circ$, 32° and 38.1° . The absence of intense peaks in the diffractogram confirms the vitreous nature of the material, meaning that no long-range order can be observed in the lattice. During the glass preparation, the precursors were heated up to $1050^\circ C$, which resulted in a solid solution with no crystalline centers and, consequently, maintaining the amorphous characteristic of the matrix, represented by the diffused halos

in **Figure 2**.⁶⁵ In addition, the thermal treatments were not able to influence the formation of a crystalline phase, even after silver nanoparticle arrangement. Yet, the residual peaks observed may show a correlation to diffraction peaks of the precursor crystalline polymorphs.⁹⁶ Within it, to confirm the nature of the crystalline phases from the residual peaks, it was attempted an indirect microstructure analysis using Rietveld refinement (RR).

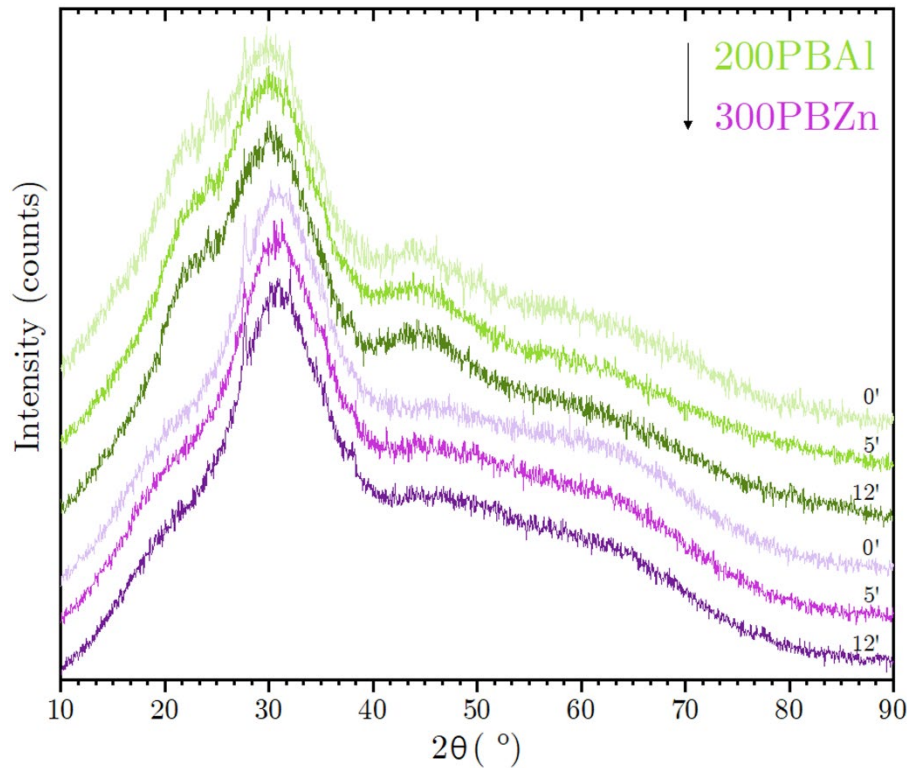


Figure 2. XRD patterns of 200PBAI (green) and 300PBZn (purple) glasses without thermal treatment (0 min.) and with annealing time of 5 and 12 min. each.

The RR of the precursors (NaH_2PO_4 , H_3BO_3 and $\text{Al}_2\text{O}_3/\text{ZnO}$) can be seen in **Figure 3** and the main phases obtained are displayed in **Table 2**. The most defined diffraction peaks for ZnO (**Figure 3** (a)) occur at 31.66° , 34.31° , 36.14° , 56.49° , 62.76° . Other less intense peaks are not attributed. The H_3BO_3 (**Figure 3** (b)) diffractogram showed one strong peak, occurring at 27.78° , with other less intense peaks not attributed

as well. For Al_2O_3 (**Figure 3 (c)**), they occur at 31.69° , 37.17° , 45.48° , 60.92° and 66.99° . At last, for the NaH_2PO_4 precursor (**Figure 3 (d)**), many phases were detected, with main peaks occurring at 22.49° , 26.38° , 27.77° and 32.92° .

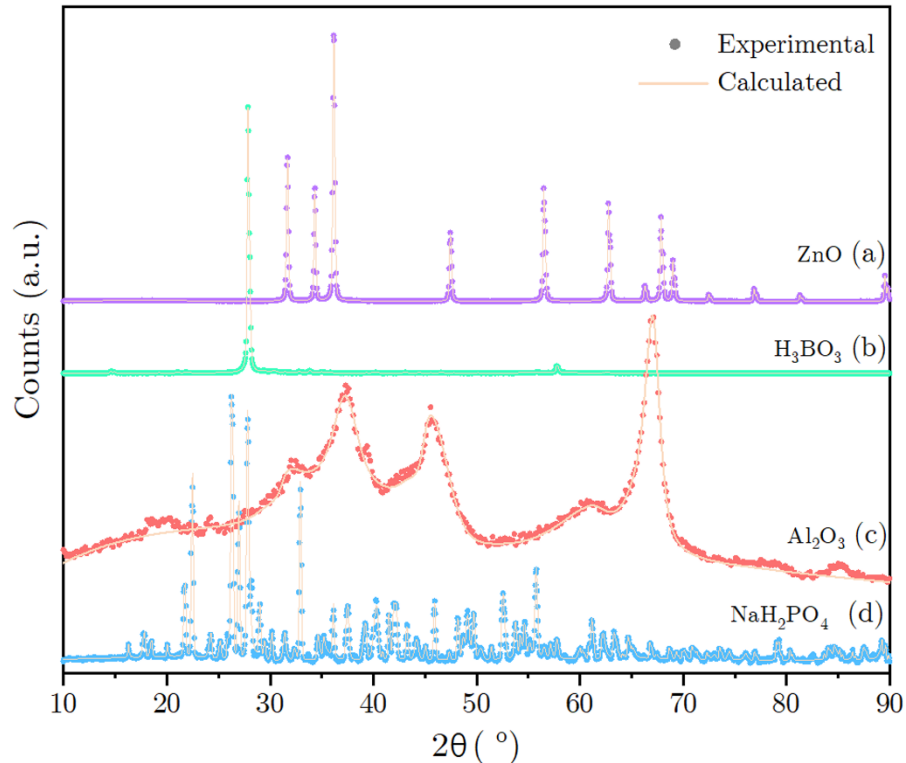


Figure 3. Rietveld refinement of the glass precursors. Calculated (straight light orange line) and experimental ZnO (purple dots), H_3BO_3 (green dots), Al_2O_3 (orange dots) and NaH_2PO_4 (blue dots) diffraction patterns.

According to RR analysis, the diffraction pattern observed for each precursor can be related to aluminum oxide, zinc oxide, boric/orthoboric acid and metaborate and, at last, tetrasodium triclinic and monoclinic (summarized in **Table 2**). By using these identified phases of the precursors, a Rietveld refinement of the glass matrices diffraction patterns was also performed, aiming the comparison of crystalline phases from the precursors with the residual peaks (observed in **Figure 2**). However, no representative crystal structure or phase could be detected from the glass diffractograms (data not shown).

Regarding this, the observed residual peaks for 200PBAl and 300PBZn can be (directly) related to the diffraction peak of metaboric acid ($B_3H_3O_6$) and tri/tetraphosphate ($NaPO_3$)₄ for the first (27.7°), while the second, at 32° , can be associated to tri/tetraphosphate ($NaPO_3$)₄ (**Figure 4**). Additionally, there may be a correlation for this last peak with aluminum oxide for 200PBAl samples and zinc oxide for 300PBZn.

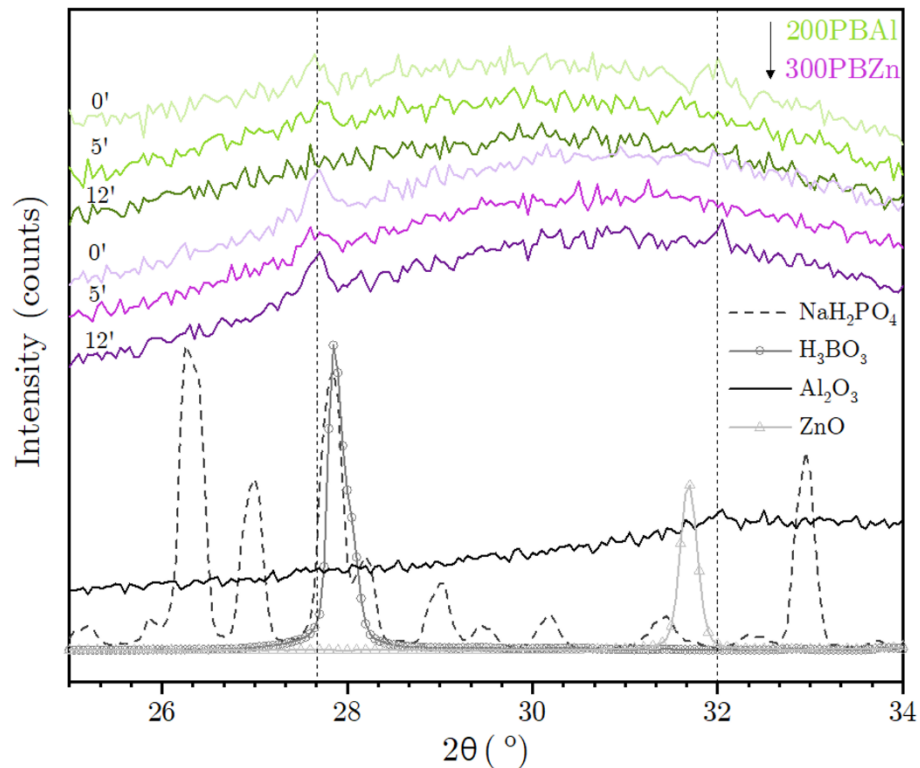


Figure 4. Experimental diffractogram of borophosphate glass samples (uppermost) modified with aluminum (green shades) or zinc (purple shades) and glass precursors (NaH_2PO_4 – dash line, H_3BO_3 – straight line with open circle, Al_2O_3 – straight line and ZnO – straight line open triangle).

Moreover, after annealing process, it was also expected for the thin nanometallic silver layer to result in an apparent peak in the diffractogram, representing crystalline silver. Yet, the Ag^0 nanoparticles may have not been detected since, in a nanocrystalline material, a small sized crystallite results in peak broadening. However, by paying attention to the diffraction patterns at angle 38.1° (**Figure 2**), it is possible to observe a residual

peak for 200PBA12 and 300PBZn12, corresponding to metallic silver face-centered cubic phase (111). Nonetheless, this direct analysis must consider that the underlying molecular packing of the crystalline form is eminently different from the amorphous material and must not be precisely attributed.

Table 2. Crystalline phase of borophosphate glass precursors identified by Rietveld refinement.

Glass matrix	Precursors			
	NaH ₂ PO ₄	H ₃ BO ₃	Al ₂ O ₃	ZnO
200PBA1	Tetrasodium Triclinic	Boric Acid	Aluminium oxide	-
	Tetrasodium Monoclinic	Orthoboric Acid	-	-
	-	Metaborate	-	-
300PBZn	Tetrasodium Triclinic	Boric Acid	-	Zinc Oxide
	Tetrasodium Monoclinic	Orthoboric Acid	-	-
	-	Metaborate	-	-

Source: Self-elaborated.

4.2. Thermal Properties Studied by DSC

The modification of a vitreous borophosphate matrix is an important step to achieve higher chemical resistance and inferior hygroscopicity, since pure borophosphate glasses are still easily degraded in aqueous solutions or in high humid environments.^{73,75} The addition of modifier agents such as zinc and aluminum oxides were employed in order to obtain borophosphate glass matrices with overall higher chemical resistance.^{65,66,71} These modifiers can provide an increase in glass durability, with singular effects granted by each modifier.^{98,99}

Differential scanning calorimetry (DSC) were performed to study the chemical resistance properties of the glassy samples. Variables such as glass transition temperature, degradation temperature and enthalpy were investigated for sample series with aluminum and zinc oxides. The DSC curves obtained from the 200PBA1 and 300PBZn samples are shown in **Figure 5**. It also shows the temperatures associated with the glass transition

(T_g), determined from the change in the slope (tangent onsets), the degradation onset (T_x) and the degradation peak (T_c), which consider the midpoint of the maximum peak value (Table 3).

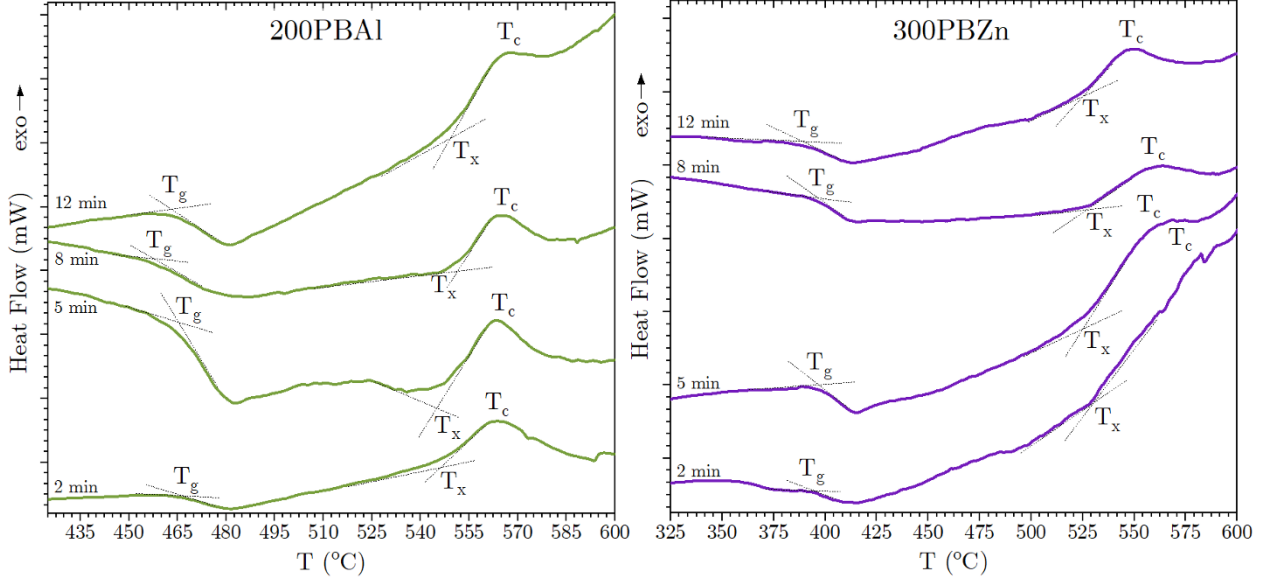


Figure 5. DSC analysis of borophosphate glass matrices modified with aluminum (left, green lines) and zinc (right, purple lines), in their respective annealing times (2 – 12 min).

Two main thermal events are clearly observed in curves independently of oxide type used in series preparation. The first one, around 400-460 °C as an endothermic base line variation, due to the glass transition; a second event as an exothermic peak corresponding to the effect of the degradation of the glassy materials structure. The area under the peak is associated with latent heat (ΔH), also shown in Table 3.

We can observe in Table 3 that T_g values are almost invariant for each preparation series. The 200PBAI series display a mean T_g temperature value of 461.3 ± 0.7 °C and 300PBZn series of 393.5 ± 3.1 °C. Despite these variations are not considered relevant for a vitreous material (range lower than 10 °C),^{100,101} we can note a slight tendency of T_g to increase for aluminum modified matrix and the opposite effect for zinc modified matrix. When analyzing the T_g temperatures with Pearson's correlation coefficient r , it is possible

to correlate it with annealing glass time. These results (Table 4) demonstrated a moderate ($r = 0.49$) correlation for 200PBAI T_g , and a strong negative ($r = - 0.88$) correlation for 300PBZn samples series. It indicates that glass transition temperature may be slightly affected with annealing process, with a tendency to increase their values for 200PBAI lattice and decrease for 300PBZn. However, this correlation demonstrated to be statistically insignificant in this current observation ($p > 0.05$) and, to better elucidate this correlation, it is necessary that glass transition temperatures are measured at higher HT times, including thermal analysis at samples without heat treatment (0 min.).

Table 3. Glass transition temperature (T_g), degradation onset (T_x), degradation peak (T_c), glass stability (ΔT) and peak enthalpy for vitreous matrices treated with Al or Zn and their respective heat treatment time (in minutes).

Matrix	HT Time (min.)	T_g (°C)	T_x (°C)	T_c (°C)	ΔT_{x-g} (°C)	ΔH (J/g)
200PBAI	2	460.4	545.9	563.5	85.6	43.6
	5	462.0	547.6	563.3	85.5	11.8
	8	461.1	549.9	564.3	88.8	13.2
	12	461.6	551.6	567.7	89.9	15.2
300PBZn	2	395.2	530.1	582.4	135.0	11.0
	5	395.6	525.0	568.5	129.4	18.6
	8	394.1	527.0	563.8	132.8	18.7
	12	389.0	521.0	549.5	132.0	31.9

Source: Self-elaborated.

Furthermore, considering both matrices, T_g of 200PBAI is higher than 300PBZn (approximately 68 °C). This difference can be attributed basically to two factors, structure relaxation of glassy lattice¹⁰²⁻¹⁰⁴ and increased vitreous network connectivities.^{73,102,105-107} Relaxation is related to the structural rearrangements occurring within a sample, and a material held in a temperature under, but close, to its T_g goes into a lower enthalpic state as it relaxes.¹⁰⁴ Lower enthalpic states are associated to lower T_g values.¹⁰⁴ Since the vitreous matrix modified with zinc was annealed at 300 °C, approximately 93 °C lower than its T_g (compared to aluminum matrix with an annealing temperature difference of

-261 °C from its T_g), it can be expected that 300PBZn matrix will eventually acquire a decreased enthalpic state compared to 200PBAI after thermal treatment.

Regarding to the vitreous network, the presence of glass modifiers, such as Al_2O_3 and ZnO to the melting can result in an increased chemical stability by increasing vitreous connectivities.^{65,108,109} As a result, a strengthening in the network is achieved leading to, consequently, an increase in the T_g temperatures. In addition, as reported by Zhang and Stamboulis¹¹⁰ in a study comparing the density of different glass-ceramics compositions, the atomic mass of a glass modifier has a more important impact in glass density and degree of packing than its atomic radius. Within it, Zn has an atomic weigh considerably higher than Al (-65/-27 u respectively), resulting in a more compacted network. Interestingly, they reported that with increase in Zn content and increase in their glass-ceramic density, a decrease in T_g from 667 °C (0%Zn) to 613 °C (60%Zn) was reported. Comparing to this, elevated content of zinc in the matrix can result in packed low range ordering affecting (adversely) the glass microstructure and chemical bonding,¹¹⁰ thus, lowering the vitreous T_g temperature compared to aluminum containing matrix. Furthermore, analyzing the difference of T_x-T_g , it is possible to investigate glass stability against devitrification as a function of heat treatment time by using the parameter $\Delta T = T_x-T_g$.^{108,109,111} There is a significant difference of thermal stability temperature between aluminum and zinc modified matrices (about 45 °C), with 200PBAI presenting the lowest value. It represents that Zinc matrix sample set is more stable against devitrification during heat (lower probability to crystallize during thermal treatment), ant can be a consequence of the low T_g values of this composition.^{112,113}

Subsequently, further structural information concerning the enthalpy can be acquired based on the peak degradation events, around 555 °C for both samples. It is observed in **Table 3**, a decrease of the enthalpy values for 200PBAI matrices and an increase for 300PBZn matrices with annealing treatment temperatures. This non-linear

opposed “trend” can be further explained considering that thermal stability of phosphate glasses is strongly related to the presence of P–O–P bonds (bridging bonds between PO₄).¹¹⁴ The degradation of the borophosphate matrix due to new bonds formed between bridging oxygens and Al or Zn cations result in a diminished bonding strength since B–O (806 kJ.mol⁻¹) and P–O (597 kJ.mol⁻¹) have increased dissociation energy compared to Al–O (512 kJ.mol⁻¹) and Zn–O (284 kJ.mol⁻¹) and, thus improve the thermal stability. A similar behavior could be observed by Choi *et. al.*,¹⁰⁹ in which a decrease in the glass stability of their ternary Ge–Sb–Se glass in increasing Ge amounts is related to destroyed Ge–Ge/Se–Se connectivities by Ge–Sb with lower bonding energy.

Table 4. Descriptive statistics (mean, standard deviation (σ), Pearson’s coefficient(r)) of borophosphate glass matrices glass transition (T_g), crystallization onset (T_x) and peak (T_c), thermal stability (ΔT_{x-g}) temperatures and enthalpic variation (ΔH).

Matrix	Statistical analysis	T_g (°C)	T_x (°C)	T_c (°C)	ΔT_{x-g} (°C)	ΔH (J/g)
200PBAI	mean	461.3	548.7	564.7	87.5	20.9
	σ	0.7	2.5	2.1	2.3	15.1
	r	0.49	0.99	0.89	0.94	-0.68
	p	0.12	0.12	0.01	0.71	0.05
300PBZn	mean	393.5	525.8	566.0	132.3	20.0
	σ	3.1	3.8	13.6	2.3	8.7
	r	-0.88	-0.88	-0.99	-0.29	0.95
	p	0.51	0.01	0.12	0.06	0.32

Source: Self-elaborated.

In addition, for 200PBAI, the ΔH for sample thermally treated for 2 minutes has a value of -46 J.g⁻¹ and decreases with rise of the annealing time. For 300PBZn matrix, the sample treated for 2 min. has a ΔH about 11 J.g⁻¹ and it increases with annealing time. Essentially, glasses are a supercooled material that have been “frozen” into high-energy conformations.⁷² When reheating it during annealing process, it allows the specimen to release this excess of energy in form of heat (thus, the exothermic peak). In this case, more heat is being lost for borophosphate glasses modified with aluminum, but after annealing

process, zinc modified matrix releases more energy. This effect is possibly explained due to the thermal treatment temperature be closer to its T_g temperature compared to 200PBA1.

At last, when borophosphate glass is doped with silver, NBOs from the PO_4 tetrahedral structure of metaphosphate chains are bonded with Ag^+ by ionic bonds.⁷⁵ When the annealing process is performed for silver-nanoparticle growth (bottom-up approach), Ag^+ ions aggregate and coalesce at the glass surface.⁶⁵ As atomic size difference of modifiers also plays a significant role in glass formation and thermal stability,^{115,116} after annealing process, the mobility of silver ions in the lattice can result in structural changes due to the change in packing density. Ag^+ ions have atomic radii of approximately 172 pm, smaller than Al^{3+} and bigger than Zn^{2+} (184 and 139 pm respectively). Consequently, when silver ions are “removed” from the lattice with increase in annealing time, it may result in loosening of aluminum-containing glass structure but in tightening of the one containing zinc. This can explain why the change in thermal treatment have this inversed propensity outcome for T_x and T_c temperatures.

In summary, the doping of vitreous matrix with Ag^+ have a reasonably good thermal stability for 300PBZn matrix sample set, but post thermal treatment tends to lower its resistance. This matrix is also expected to have higher degree of packing. In the other hand, a lower thermal stability is observed for 200PBA1 matrix sample set, with a tendency in increasing its stability with an increase in post thermal treatment. This matrix is also expected to have increased connectivities in its vitreous lattice.

4.3. Chemical Glass Structure

4.3.1. Molecular evaluation by Raman spectroscopy

The borophosphate glass samples modified with the two different oxides, Al_2O_3 or ZnO , had their Raman spectra measured for each time treatment under study in order to elucidate the resulting structure modifications after the NP growth process. The results are summarized in **Figure 6**.

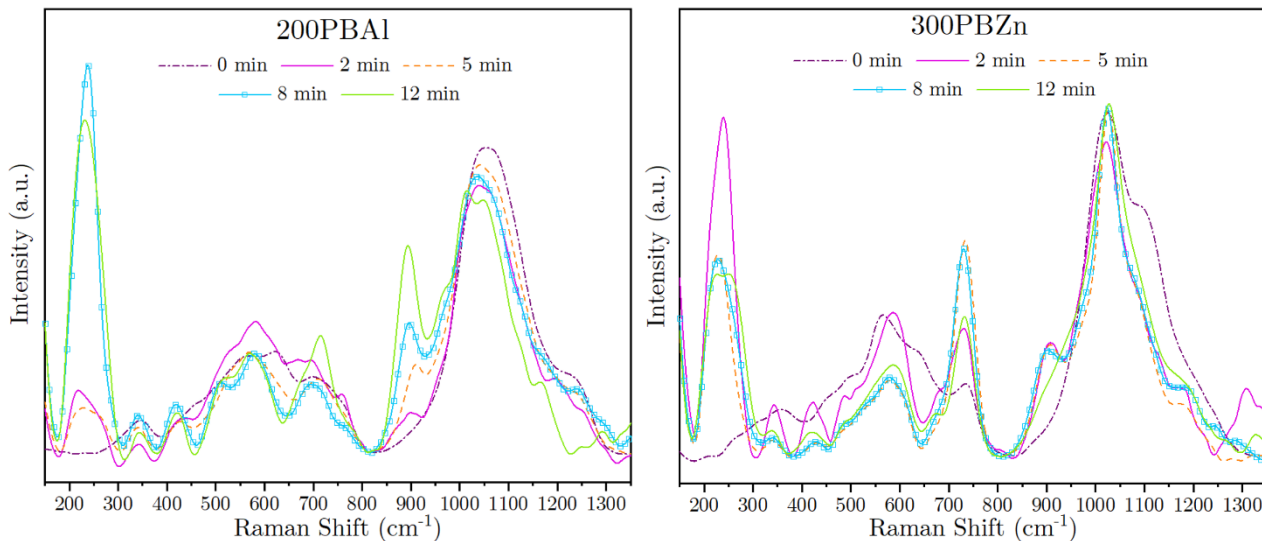


Figure 6. Raman spectra (532nm) of borophosphate glass samples modified with aluminum (left) and zinc oxides (right) without thermal treatment (0 min.) and with annealing time of 2, 5, 8 and 12 min. each

4.3.1.1. Aluminum modified matrix

It is displayed in **Figure 7** the Raman spectra of only aluminum borophosphate glass sample set without thermal treatment, with its respective vibrational modes (and no baseline correction). Comparison of the changes in vibrational modes for the following thermal treatment times can be observed in **Figure 8** (baseline corrected). The most intense band is found between 850 and 1300 cm^{-1} of the Raman shift. Deconvolution of the spectra in this region (not shown), using Lorentzian line shapes for fitting, indicated the presence of four peaks. First, the shoulder at $\approx 891 \text{ cm}^{-1}$ can be ascribed to symmetric

stretching of P–O bonds.^{38,65,66} With augmentation in HT time, it is possible to observe an increase in intensity of 891 cm^{-1} shoulder (as seen in **Figure 8**). Annealing time up to 8 minutes shows an additional contribution at $\approx 960 \text{ cm}^{-1}$, ascribed to asymmetric stretching of P–O–P in metaphosphate (Q^2) structures.^{65,66,68,117–120}

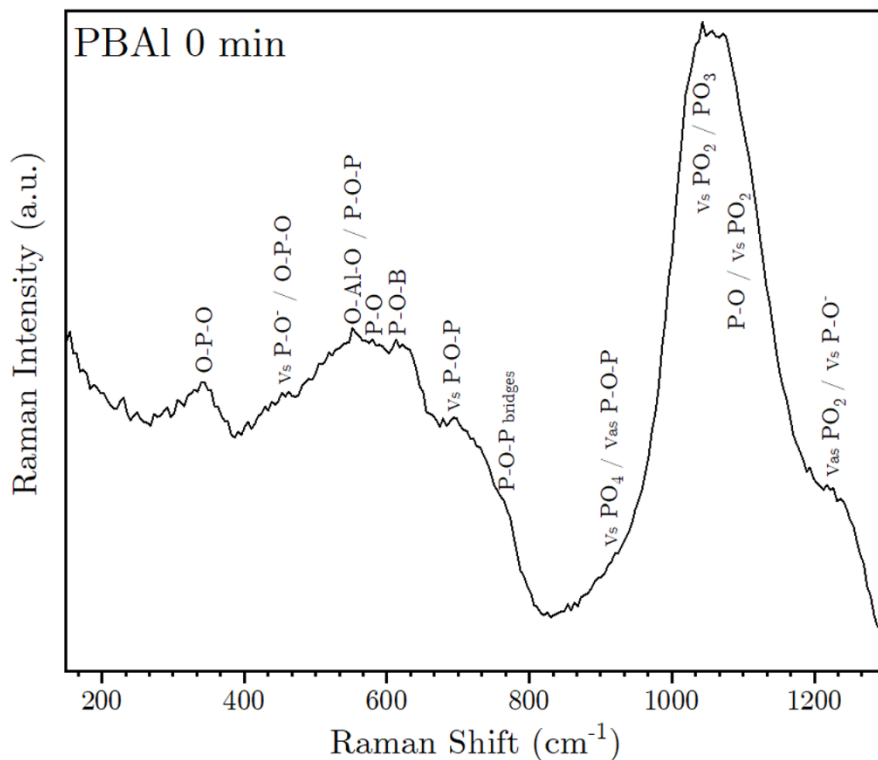


Figure 7. Raman spectra (532nm) of borophosphate glass samples modified with aluminum without thermal treatment.

This is not clearly understood, but can be explained, as discussed earlier, by the fact that NBO of isolated metaphosphate chains are ionically bonded with Ag^+ . With thermal treatment, these silver ions coalesce at the surface, increasing the number of P–O structural units in the Q^2 structures. Furthermore, Belusso and collaborators⁶⁵ observed that an increase in aluminum content equals or superior to 10 mol% Al_2O_3 in their borophosphate glasses made the band related to $\nu_{\text{as}}\text{P-O-P}$ (at approx. 930 cm^{-1}) disappear due to depolymerization of Q^2 units.⁶⁵ However, this band is reappearing after thermal

treatment, inferring that doped borophosphate glass matrices with prolonged annealing periods may increase the cross-linking and vitreous connectivities.

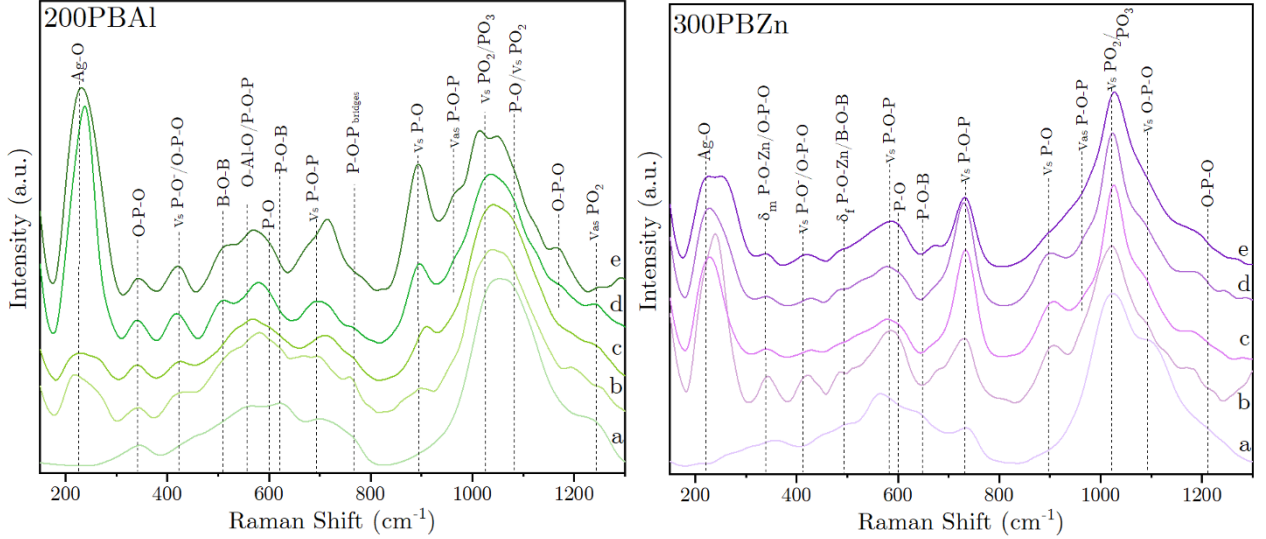


Figure 8. Raman spectra (532nm) of 200PBAI (left) and 300PBZn (right) at their corresponding annealing times (a-0 min, b-2 min, c-5 min, d-8 min and e-12 min).

Other contribution found in the envelope, is the band at $\approx 1024 \text{ cm}^{-1}$ assigned to $\nu_s(\text{PO}_3)$ stretching modes⁶⁶ and/or to asymmetric stretching of non-bridging PO_2 in Q^1 units.^{118,119} The band at $\approx 1080 \text{ cm}^{-1}$ is related to stretching of P–O bonds in pyrophosphate groups (Q^1) and can also be related to symmetric stretching of non-bonded P–O–P in Q^2 structure.^{65,66,70,121} It was observed a narrowed blue shift in this region, with a small decrease in intensity. Since Raman spectra is composed on the vibration frequency of a substance, peaks can shift in wavenumber without any change in the atomic species. Shifts to higher frequencies may indicate changes in the P–O–P bond angles, such as increase in the bonding energy of the atomic species.¹²² The fourth contribution in the envelop is the shoulder at $\approx 1240 \text{ cm}^{-1}$. It is ascribed to asymmetric $\nu_{\text{as}}\text{PO}_2$,^{65,66,68,123} and is shifted towards lower wavenumbers with continued annealing time ($\approx 1235 \text{ cm}^{-1}$ for 8 min.), while is barely seen at 12 minutes.

Additional deconvolution of spectra between 200 and 800 cm^{-1} of the Raman shift reveals the different following attributions: i) A strong peaks around 212 cm^{-1} /237 cm^{-1} , ascribed to silver mode (metallic silver nanoparticles) or to the Ag^+ ionic species sorbed onto the metal surface;^{38,124} ii) The band at $\approx 343 \text{ cm}^{-1}$, assigned to symmetric stretching of O–P–O bond in Q^2 structures;^{38,65,66,68,70,119,121} iii) Further, peaks at $\approx 426 \text{ cm}^{-1}$ are related to stretching and bending modes of P–O bonds (ν_s PO- and O–P–O) of orthophosphate PO_4^{3-} ; iv) Torsional modes around 494 cm^{-1} can be associated with diborate groups;^{68,125} v) Vibrational modes related to the cation motion and chain conformation are found at $\approx 561 \text{ cm}^{-1}$,^{38,66} involving O–AL–O moieties; vi) The presence of stretching and bending modes of P–O are observed at $\approx 600 \text{ cm}^{-1}$. vii) Bands at $\approx 620 \text{ cm}^{-1}$ are assigned to stretching modes of P–O–B and ν_s P–O–P of the long chain of phosphate glass,^{38,65,66,118} in which the band broaden and almost disappears completely after thermal treatment longer than two minutes. At last, the peak at $\approx 698 \text{ cm}^{-1}$ is also related to symmetric stretching modes of P–O–P, and ν_s P–O–P bridges at $\approx 765 \text{ cm}^{-1}$. The first peak red shifts from ≈ 698 to approximately 714 cm^{-1} , while the peak at the shoulder broadens, slightly shifting to longer wavenumbers. The ascribed stretching modes of all peaks are summarized in **Table 5**.

4. Results and Discussion

Table 5. Vibrational modes presented on Raman spectra of borophosphate glasses modified with aluminum or zinc.

	Position (cm ⁻¹)		Indication	Vibrational mode
	200PBAI	300PBZn		
≈	212	237	Ag-O	Silver modes or to ionic species sorbed onto the metal surface. ^{38,124}
≈	343	345	O-P-O δm (P-O-Zn)	Network bending vibrations of O-P-O chains in Q2 structures and/or bending modes of polyhedral with Zn cations. ^{38,65,66,68,70,118,119,121}
≈	426	427	vs PO- O-P-O	Stretching modes of vs PO- and bending modes of O-P-O in orthophosphate PO4 ³⁻ units. ⁶⁸
≈	495	494	δf (P-O-Zn) Diborate	Torsional modes of polyhedral with Zn cations / isolated diborate groups. ^{68,119}
≈	561	561	O-Al-O Al-O-Al P-O-P	Bending modes involving O-AL-O moieties, associated with the motions of bridged oxygen in Al-O-Al / bending vibrations of P-O bonds. ^{38,65,66,68}
≈	600	600	P-O	Stretching and bending modes of P-O. ⁶⁸
≈	620	630	P-O-B vs P-O-P	Stretching of P-O-B/vsPOP of the long chain of phosphate glass. ^{38,65,66,118}
≈	698	-	vs P-O-P	Symmetric stretching of P-O-P. ^{38,66,68,121}
≈	765	730	vs P-O-P bridges	Symmetric vibration of bridging oxygen (P-O-P) in the long-chain metaphosphates and in Q1 units. ^{38,65,66}
≈	891	882	vs P-O	Symmetric vibrations of P-O links of orthophosphate (Q0). ^{68,120,121}
≈	960	960	vas P-O-P	Asymmetric stretching of P-O-P in metaphosphate (Q2) structures. ^{65,66,68,118-120,123}
≈	1024	1019	vs PO3 vs PO2	Stretching of non-bridging PO2 sym in Q1 units. ^{66,118,119} Source: Self-elaborated
≈	1080	1107	P-O vas PO2	Stretching of P-O bond in pyrophosphate groups (Q1) / asymmetric stretching of P-O-P non-bonded (Q2 structure). ^{65,66,70,121}
≈	1170	1206	P-O-P	Stretching vibrations of P-O-P in Q1 units. ^{68,120}
≈	1240	-	vas PO2	Asymmetric stretching vibration of PO2 non-bonded (Q2 structure). ^{65,66,68,123}

Source: Self-elaborated

4.3.1.2. Zinc modified matrix

Raman spectra of only zinc borophosphate glass sample set without thermal treatment is presented in **Figure 9**, presenting also its ascribed vibrational modes (with no baseline correction). Comparing the matrices containing zinc and aluminum with their respective thermal treatment time (shown in **Figure 8**, for instance), we can observe similarities in the emission spectra, once the chemical structure is akin.

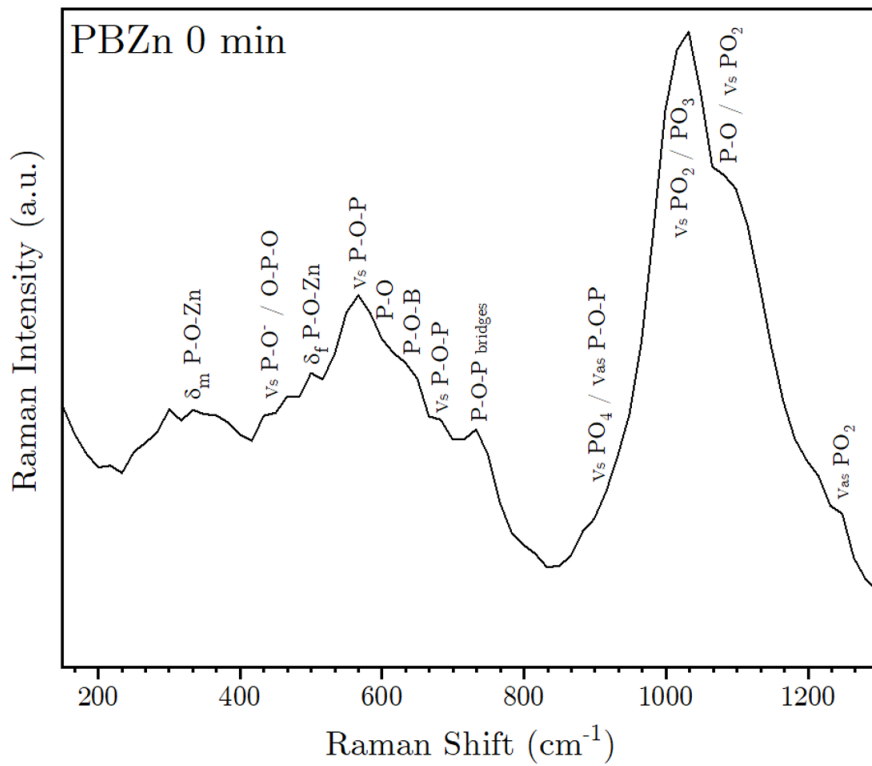


Figure 9. Raman spectra (532nm) of borophosphate glass samples modified with zinc without thermal treatment.

As observed in aluminum modified borophosphate glass, the most intense band for sample prepared with zinc is also found between 850 and 1300 cm^{-1} . Deconvolution of the spectra in this region (not shown), using Lorentzian line shapes for fitting, also indicated the presence of four peaks, i.e.: i) The shoulders at $\approx 882 \text{ cm}^{-1}$, commonly ascribed to isolated orthophosphate groups in Q^0 units and to symmetric stretching of P-O;^{68,120,121}

ii) A contribution band at $\approx 960 \text{ cm}^{-1}$, ascribed to asymmetric stretching of P–O–P in metaphosphate (Q^2) structures;^{65,66,68,117–120} iii) The band at $\approx 1019 \text{ cm}^{-1}$, assigned to $\nu_s(\text{PO}_3)$ stretching modes⁶⁶ and/or to symmetric stretching of non-bridging PO_2 in Q^1 units,^{118,119} similarly to 200PBAI matrix. The band at $\approx 1107 \text{ cm}^{-1}$ is also related to stretching of P–O bonds in pyrophosphate groups (Q^1) and can further be related to symmetric stretching of non-bonded P–O–P in Q^2 structure;^{65,66,70,121} and iv) The peak at $\approx 1206 \text{ cm}^{-1}$, assigned

to stretching vibrations of P–O–P in Q^1 units.^{68,120} This shoulder slightly shifts to lower wavenumbers ($\approx 1180 \text{ cm}^{-1}$), becoming more prominent with prolonged thermal treatment.

Further deconvolution of spectra in lower Raman shifts (between 200 and 1200 cm^{-1}) showed similar attributions with 200PAI: i) The strong peaks around 212/237 cm^{-1} , ascribed to silver modes (metallic silver nanoparticles) or to the Ag^+ ionic species sorbed onto the metal surface;^{38,124} ii) The band around $\approx 345 \text{ cm}^{-1}$ is assigned to symmetric stretching of O–P–O bond in Q^2 structures and, in the presence of ZnO as a modifier agent, it can also be ascribed to torsional modes of phosphate polyhedral noted as δ_m P–O–Zn;^{38,65,66,68,70,119,121} iii) stretching and bending modes at $\approx 427 \text{ cm}^{-1}$, ascribed to P–O bonds (ν_s PO- and O–P–O) of orthophosphate PO_4^{3-} ; iv) Similar torsional modes of phosphate polyhedral attributed to δ_f (P–O–Zn), around 494 cm^{-1} , and can also be associated with diborate groups;^{68,125} v) Stretching modes involving P–O bonds motion are found at $\approx 561 \text{ cm}^{-1}$.^{38,66} vi) The presence of stretching and bending modes of P–O are also observed at $\approx 600 \text{ cm}^{-1}$. Vii) Bands at $\approx 630 \text{ cm}^{-1}$ are assigned to stretching modes of P–O–B and ν_s P–O–P of the long chain of phosphate glass, in which the band red shifts to higher wavenumbers to approximately $\approx 670 \text{ cm}^{-1}$. At last, the peak at $\approx 730 \text{ cm}^{-1}$ is also related to symmetric stretching modes of P–O–P. This band increases in intensity according to prolonged thermal treatment.^{38,65,66,118}

As has been observed, few changes in the glass lattice, for both compositions, can be noticed. One clear event is the rise of the peak related to silver particles. This region increases for both matrix compositions with increasing in HT time but has no linearity for 300PBZn sample. This is due to zinc modified matrix HT temperature being 100 °C higher than for aluminum modified matrix. As a consequence, silver ions move with less restriction in the 300PBZn lattice and grow at the surface in a higher rate, achieving larger sizes in a shorter time. As this band can also be associated to AgO,^{38,124} prolonged annealing time may also form a (quasi-flat) thin nanolayer, considerably reducing the total surface area available for oxidation, hence being able to explain why longer thermal treatment is not correlated to linear intensity increase in this region.

Furthermore, the existence of silver ions in the matrix favors the presence of ortho, pyro and small metaphosphate chains.⁶⁸ And, with thermal treatment, silver ions are “extracted” from the matrix, disfavoring these structure conformations, what could possibly explain the broadening and dissipation of some peaks related to these arrangements.

4.3.2. Molecular evaluation with FTIR spectroscopy

In order to assist in the understanding of the molecular characteristics and its modifications in vitreous samples with annealing process and get supplementary molecular description, Fourier-transform infrared spectroscopy (FTIR) analysis was performed. The spectra of aluminum and zinc borophosphate glass sample set, without thermal treatment and with their corresponding ascribed absorption bands, are presented in **Figure 10** and **Figure 11**, respectively.

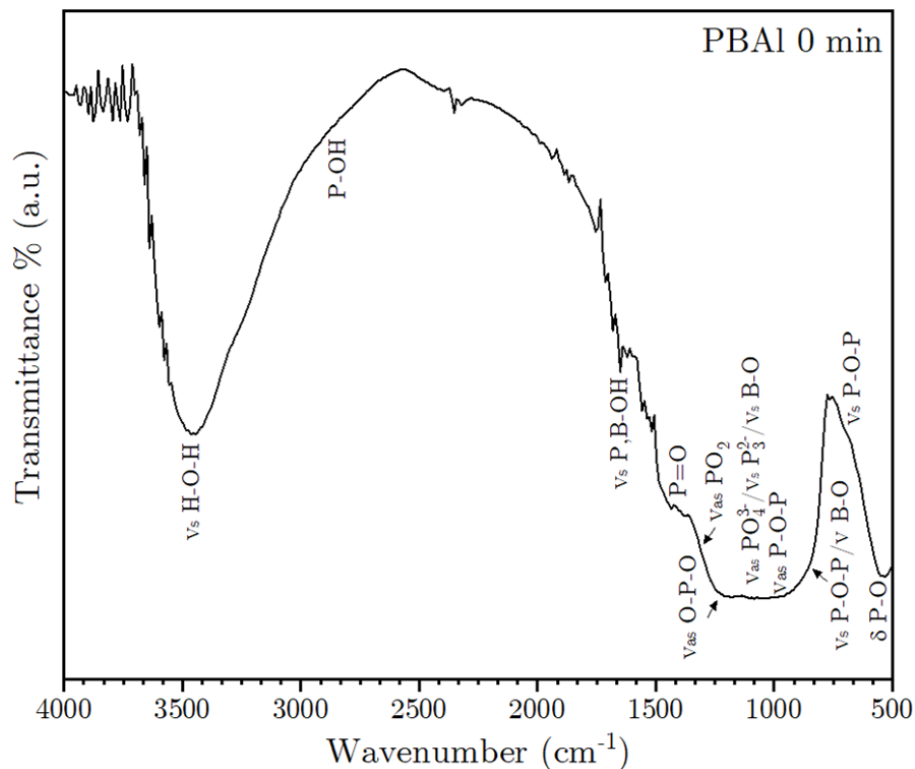


Figure 10. FTIR spectra of borophosphate glass matrices modified with aluminum without thermal treatment.

These spectra were collected between 400 and 4000 cm^{-1} and are mainly formed by convoluted phosphate bands, the higher phosphate concentration in the sample masks the borate contribution in the lattice. Few borate and some superimposition of phosphate and borate bands are also visible around 1100 cm^{-1} . Vibrational modes related to PO_2 in non-

bonding groups or stretching modes of B–O in BO_4 groups are located at 540 cm^{-1} for 200PBA1 matrix and at 553 cm^{-1} for 300PBZn matrix. This band is more pronounced in the aluminum modified sample and it decreases and narrows after thermal treatment.

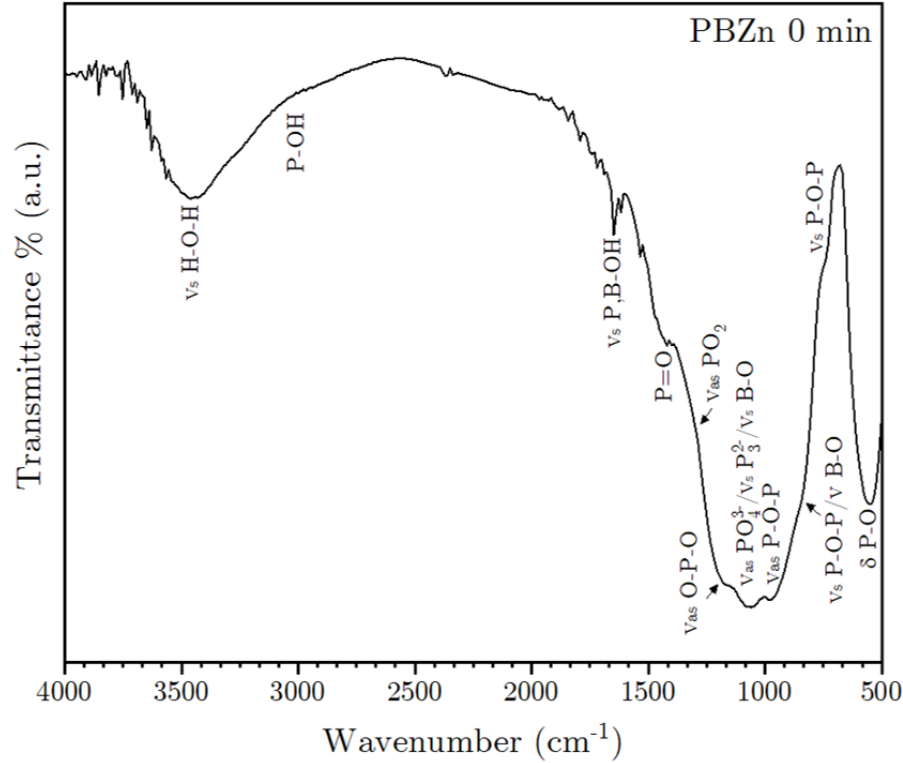


Figure 11. FTIR spectra of borophosphate glass matrices modified with zinc without thermal treatment.

Between the region $600\text{--}1000\text{ cm}^{-1}$, occur stretching vibrations of oxygen atoms in P–O–P structures, where symmetric vibrations are located at ≈ 690 and 739 cm^{-1} for 200PBA1 and 300PBZn glasses, respectively. This region decreases in intensity with annealing time treatment for aluminum matrix samples series and slightly gain intensity for matrix containing zinc. As reported by El-Damwari *et. al.*¹²⁶ in a study of phosphate glass modified with silver oxide, an increased concentration of Ag_2O in their lattice resulted in an area decrease for the region related to stretching vibrations of oxygen atoms in P–O–P bridges ($620\text{--}830\text{ cm}^{-1}$). This represented a reduction in bridging oxygen concentration linking two phosphorus ions, expending the number of NBO in their phosphate network.¹²⁶

Withing it, it can be inferred that the number of NBO in aluminum modified matrix slightly increases after thermal treatment, not affecting much the glass samples with zinc. Collected spectra of samples after annealing process of 12 minutes can be seen in **Figure 12**, where a comparison of samples heat treatment time is performed.

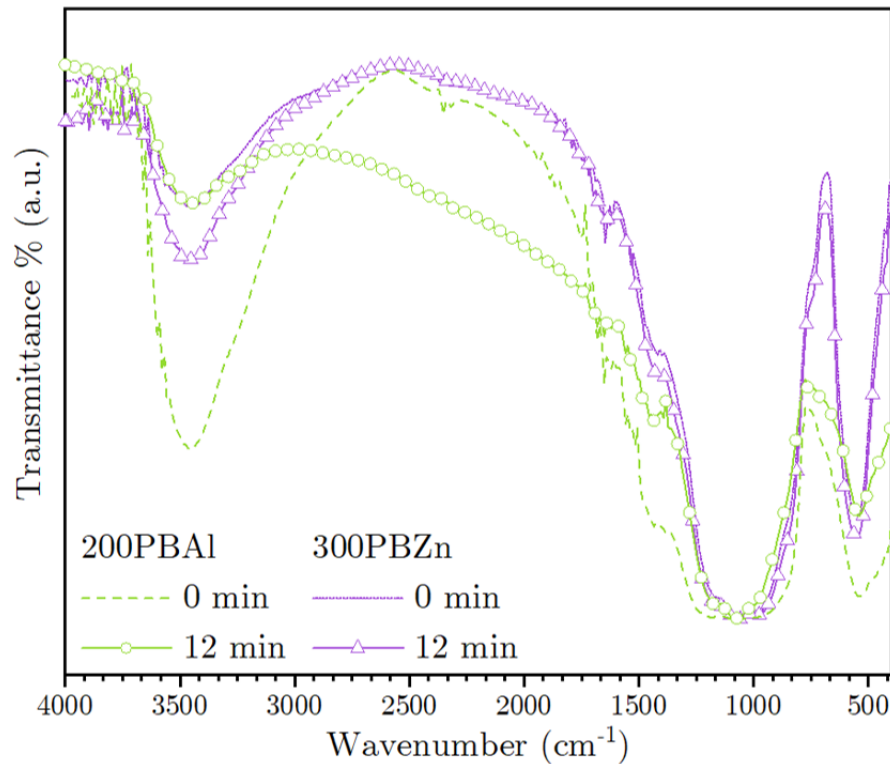


Figure 12. FTIR spectra of borophosphate glass matrices modified with aluminum (green) and zinc (purple) without thermal treatment and with thermal treatment with 12 min

A shoulder at approximately 857 cm^{-1} (200PBA1) and 853 cm^{-1} (300PBZn) is related to symmetric stretching of P–O–P in Q^2 units of metaphosphate and/or stretching of B–O bonds in BO_4 tetrahedra from diborate groups. An asymmetric stretching mode of P–O–P groups in Q^1 units is assigned, for aluminum and zinc modified lattices, at ≈ 971 and 976 cm^{-1} respectively. Furthermore, a superimposition of bands between asymmetric PO_4^{3-} in Q^0 units, symmetric $Q^1 PO_3^{2-}$ groups and symmetric B–O stretching in BO_4 groups occur at $\approx 1094\text{ cm}^{-1}$ for aluminum and 1080 cm^{-1} for zinc modified glasses. The bands

located between 1300-1500 cm^{-1} are assigned to vibrational modes of doubled bond P=O, in which at ≈ 1315 and 1296 cm^{-1} is situated asymmetric stretching of non-bridging oxygens in Q^2 tetrahedra ($\nu_{\text{as}} \text{PO}_2$) for 300PBZn and 200PBAI respectively. Vibrational modes of P=O in Q^3 units are found at around 1414 cm^{-1} (Zn^{2+}) and 1420 cm^{-1} (Al^{3+}). This band decreases in intensity after thermal treatment for aluminum glass sample, which may be related to a change in the lattice of a high cross-linked Q^3 structure to chain like Q^2 network.

Lastly, the lower frequency region ($1600\text{-}3600 \text{ cm}^{-1}$) are assigned to vibrational modes of OH groups, where harmonic OH vibration in P-OH or B-OH structures are situated at approximately 1651 and 1647 cm^{-1} . Vibration modes of P-OH are also located at ≈ 2877 and 2884 cm^{-1} and symmetric stretching of H-O-H groups are found at ≈ 3456 and 3462 cm^{-1} for 200PBAI and 300PBZn matrices, respectively. This late band is more attenuated for aluminum glass matrix without thermal treatment (0 min). It diminishes in intensity after thermal treatment, as observed in **Figure 12**, reaching similar values as for 300PBZn0. On the other hand, 300PBZn matrix has this band increased. This difference in band intensity relate to O-H vibrational modes may be due to sample handling. All assignments are summarized in **Table 6**.

4. Results and Discussion

Table 6. Vibrational modes presented on FTIR spectra of borophosphate glasses containing aluminum or zinc oxide.

	Position (cm ⁻¹)		Indication	Vibrational mode
	200PBA1	300PBZn		
≈	540	553	δ P–O/B–O	Bending modes in PO ₂ non-bonding groups and/or in BO ₄ groups. ^{65,71,75,77}
≈	690	739	vs P–O–P	Stretching vibrations of oxygen in P–O–P structures. ^{65,70,71,75,126,127}
≈	857	853	vs P–O–P/ν B–O	Symmetric P–O–P in linear Q ² units / stretching of B–O bonds in BO ₄ tetrahedra. ^{71,75,77,128}
≈	971	976	vas P–O–P	Asymmetric stretching of POP groups in Q ¹ units. ^{71,75,127}
≈	1094	1080	vs B–O/vas PO ₄ ³⁻ vs PO ₃ ²⁻	Superimposition of asym (PO ₄) ³⁻ in Q ⁰ groups, sym Q ¹ (PO ₃) ²⁻ groups and sym B–O in BO ₄ . ^{65,71,77}
≈	1218	1172	vs O–P–O	Vibrations of non-bridging PO ₂ groups. ⁷¹
≈	1315	1296	vas PO ₂	Asymmetric stretching of PO ₂ non-bridging oxygen in Q ² tetrahedra. ^{103,126}
≈	1414	1420	P=O	P=O stretch in Q ³ units. ¹²⁹
≈	1651	1647	vs P,B–OH	Harmonic OH vibrations in P–OH or B–OH structures. ⁷¹
≈	2877	2884	P–OH	Vibration modes of P–OH. ¹²⁹
≈	3456	3462	Vs O–H–O	Symmetric stretching of O–H groups. ⁷¹

Source: Self-elaborated

4.4. Nanoparticle Morphology by SEM

Borophosphate glasses doped with silver were used as a substrate for nanoparticle growth by using the bottom-up approach, based on thermal treatment under a reductive atmosphere. This process was accomplished for both matrices (containing aluminum or zinc) at different annealing times (2, 5, 8, 12 min.), in which these times individually resulted in distinct sizes of nanoparticles. Since Raman signal enhancement through LSPR is size dependent,^{42,61,130} we investigated how heat treatment time affected the nanoparticle growth and length. For this study, scanning electron microscopy (SEM) was selected to allow the examination of the glass surface in whole. Within it, SEM images were used for accessing nanoparticles diameter, also the morphology and the presence of clusters. The size evaluation used a count of 201 particles (of every topography SEM image) for both matrices at each HT time, and the resultant data were then used for calculating the average size.

4.4.1. Morphology and distribution evaluation

When the glass samples are exposed to heat under reductive atmosphere (H_2), the silver ions present in the glass matrix are reduced and the nucleation process is started. Each silver nucleus, formed on the glass surface, increases in size by aggregating dissolved Ag^+ ions from the neighbor particles and from the bulk (bottom-up growth process).

Figure 13 shows the SEM images for borophosphate glass modified with aluminum thermally treated during 2 (a), 5 (b), 8 (c) and 12 min (d). Sample matrix series modified with zinc are shown in **Figure 13** with 2 (e), 8 (f) and 12 (g, h) min. annealing time. Nanoparticle size and shape measurements were performed considering only the visible surface area. For the width evaluation, a qualitative analysis of the SEM images was used, as describe previously (3.3.1), to measure the total area and, thus, calculate the diameter.

As observed in **Figure 13**, Ag-NP particles are distributed through all the glass surfaces in an unequal shape, although adopting preferably a spherical-like form. The median size observed for the lowest HT time (2 min.) of the aluminum modified matrix sample was 8.4 nm, and the sizes for longer annealing times were approximately 3, 4 and 5-fold bigger for the 5, 8 and 12 minutes, respectively. For the zinc modified matrix sample, the median obtained was 24.9 nm and size variation were approximately 2 and 3-fold bigger for the 8 and 12 min., respectively (refer to **Table 7**).

It is also noticeable that each HT time resulted in a distribution width, with larger variations observed in zinc matrix sample set. This can be associated with the gaps between the nanoparticle, indicating a coalescence between clusters. The measured interparticle distance, represented as mean value with standard deviation, were 3.1 ± 0.7 , 10.3 ± 3.4 , 7.8 ± 2.6 and 11.5 ± 2.6 for aluminum containing matrix (treat for 2, 5, 8 and 12 min., respectively) and 5.1 ± 1.7 , 16.4 ± 4 and 26.7 ± 4 for zinc containing matrix (treat for 2, 8 and 12 min., respectively).

Interestingly, these inter-particle distance values increase instead of decreasing. It was expected that NP gap would be reduced since nanoparticles would grow and get closer to one another. However, this behavior indicates that smaller nanoparticles are dissolving and coalescing together forming one bigger Ag-NP nucleus, best seen in **Figure 13** (h). As a result, the silver nanoparticles seem to adopt a three-dimensional-like structure for prolonged thermal treatment times, disorderly growing in the axial and longitudinal plane, which contributes to the particle size variation and dispersity.

Schneider and co-workers,⁶⁴ for instance, obtained a silver nanoparticle film on germanium-phosphate glass fibers modified with aluminum by the bottom-up process, annealed under H₂ atmosphere, and achieved a similar behavior, in which longer thermal treatment time increased nanoparticle size. They also observed that, by increasing the thermal treatment temperature up to 350 °C, shorter annealing times were able to produce

more substantial nanoparticles, but coalescence between each silver cluster was more prominent, resulting in a thin metallic film instead of separate nanometallic nucleus.

Lenz *et. al.*⁶⁶ studied a likewise process, encompassing a borophosphate glass matrix modified with aluminum and doped with copper. They reported that, under a reductive atmosphere, no nanoparticle growth could be observed for low annealing temperatures (<300 °C), even at prolonged times (>1 h). According to these observations, it is possible to infer that nanoparticle growth by the bottom-up process depends not only on the thermal treatment time applied, but also on the temperature of thermal treatment, which are correlated to the composition of the glass matrix.

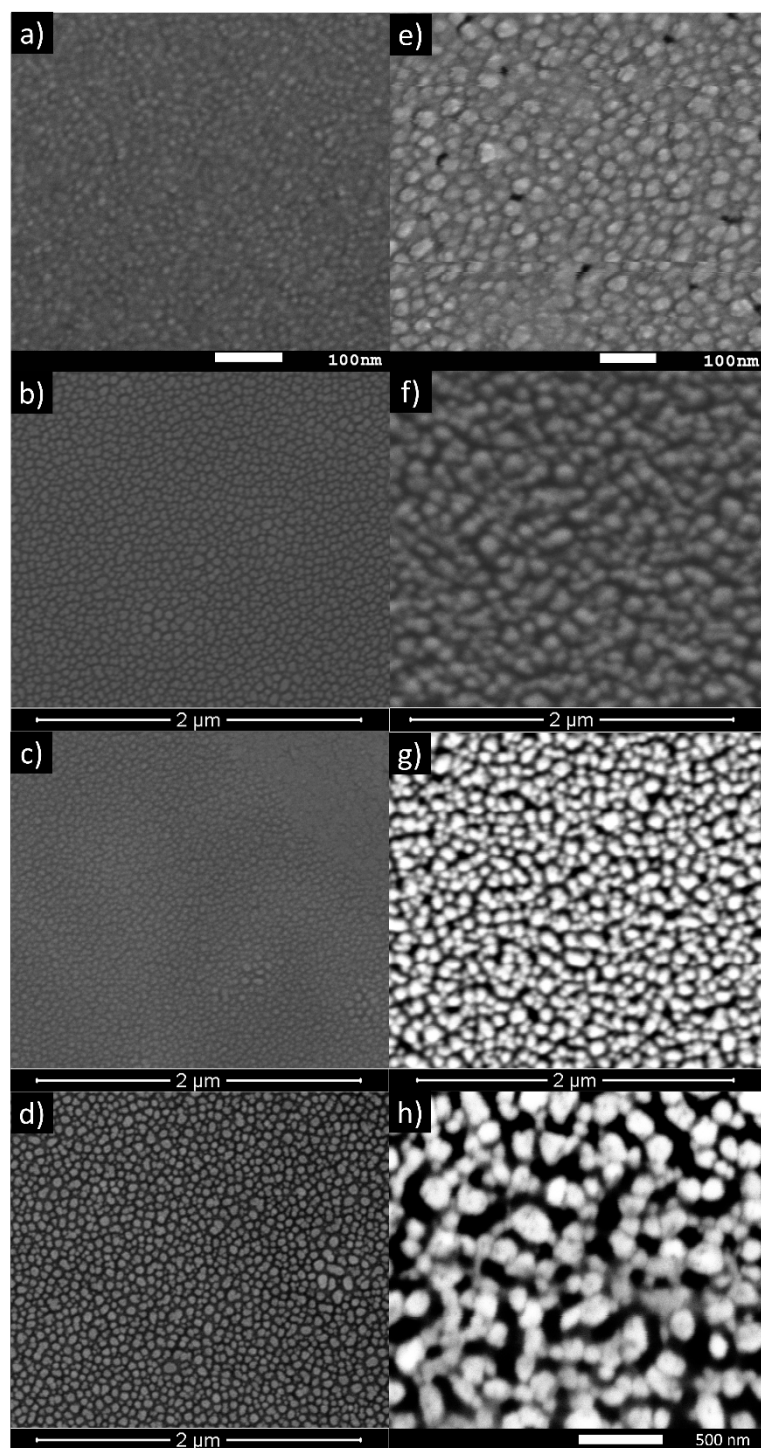


Figure 13. SEM images of borophosphate glasses modified with aluminum (left side) annealed for 2 (a), 5 (b), 8 (c) and 12 (d) minutes and zinc (right side) annealed for 2 (e), 8 (f) and 12 (g and h) min.

4.4.2. Nanoparticles size statistical analysis from SEM data

For nanoparticle size evaluation, it is important to consider that what is in fact being studied is an average of the total size values. Since NP growth process can result in a broad dispersion in size, identifying the best approach to represent the average value of the particle size distribution (PSD) is preferred. Shapiro-Wilk test (to access normality) was used, with a confidence interval of 95% and, according to the results, only aluminum modified matrix treated for 8 and 12 minutes were statistically significant ($p > 0.05$), representing that they were the only normally distributed data, (**Figure 14** represents the comparison between normally distributed data, observed for Ag-NP on 200PBA18 (green), and non-normally distributed data, observed for 300PBZn8 (purple)).

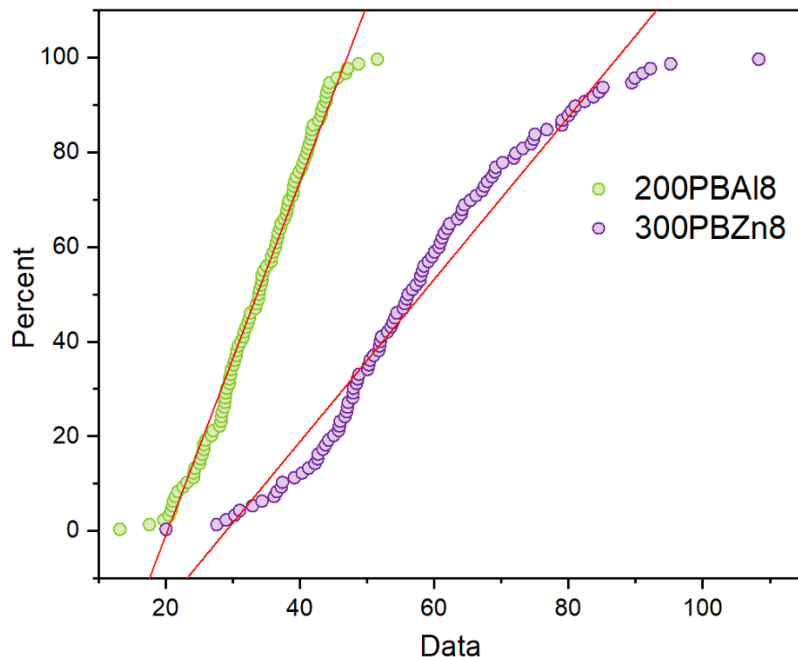


Figure 14. Normality plot of silver nanoparticle grown on both glass sample matrices (modified with aluminum or zinc), thermally treated for 8 min. Normally (200PBA18) and non-normally (300PBZn8) distributed data are compared.

For this reason, only nonparametric tests were selected for further analysis. The dispersity values, calculated using the quartile-based coefficient of variation (QCV) from a nonnormally distributed data, are summarized in **Table 7** and **Figure 15**.

4. Results and Discussion

Table 7. Descriptive statistics (median, percentiles, median absolute deviation (MAD), quartile-based coefficient of variation (QCV), mean and standard deviation) of nanoparticle size and distance of the respective heat treatment time of each glass matrix, with calculated values for samples treated for 5 min.

Glass Matrix	HT time (min.)	NP size (nm)				MAD	QCV (%)	NP gap distance (nm) mean \pm σ
		P25	Median	P75	Calculated $\pm \sigma$			
200PBAI	2	7.2	8.4	9.7	-	1.5	29.5	3.1 \pm 0.7
	5	21.9	25.7	29.9	21.7 \pm 5.6	5.0	31.1	10.3 \pm 3.4
	8	28.4	33.9	39.5	-	6.4	32.6	7.8 \pm 2.6
	12	32.4	41.0	49.1	-	9.2	40.7	11.5 \pm 2.6
300PBZn	2	15.7	20.5	24.9	-	5.3	45.1	5.12 \pm 1.7
	5	-	-	-	37.5 \pm 6	-	-	-
	8	47.0	56.1	68.6	-	13.1	38.6	16 \pm 4
	12	56.7	73.3	95.5	-	20.8	52.8	26.7 \pm 4

Source: Self-elaborated

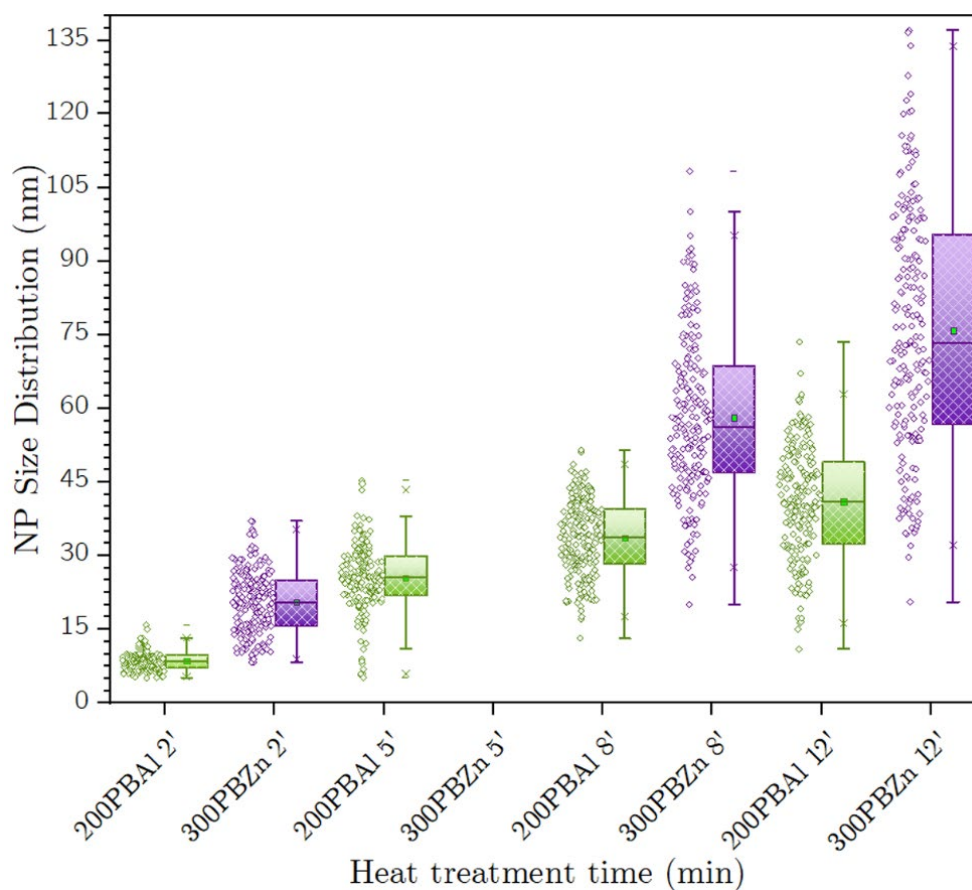


Figure 15. Boxplot of non-normal size distribution of nanoparticles grown on both glass matrices (modified with aluminum or zinc), at their respective thermal treatment time (2-12 min.). The dispersity of NP size (dot scores) has fixed values for “x” axis, varying only in the “y” axis.

In an attempt to calculate the median value of 300PBZn for the thermal treatment time of 5 minutes, a linear regression was performed on both glass sample medians at this specific HT time and is presented in **Figure 16**. The line equation for aluminum modified matrix (at HT time of 5 min.) is given as

$$y = 3.15*x + 5.97$$

Eqn. (7)

With a R^2 value of 0.92 and a mean deviation of ± 5.59 . While for zinc modified matrix, the line equation obtained was

$$y = 5.33*x + 10.84$$

Eqn. (8)

With a R^2 value of 0.99 and a mean deviation of ± 6 . nm. The comparison between the calculated size for the HT time of 5 min., using both Eqn. (7) and Eqn. (8), is also seen in **Figure 16**. The estimated value of 200PBA15 is 21.7, approximately 3.9 nm inferior than the experimental (25.7 nm) but is still in the calculated deviation range. This indicates a satisfactory fitting, with a good prediction of nanoparticle size values. The computed 300PBZn5 size was then measured, and a value of $37.5 \text{ nm} \pm 6 \text{ nm}$ was found. This value will be further used to represent the expected NP size of zinc modified matrix annealed for 5 min.

Moreover, seeking to analyze the particle size variation, we calculated the deviation of data from the median value applying MAD equation and the dispersity with QCV equation (Eqn. (2) and Eqn. (4) respectively). It was observed that the overall size deviation of 200PBA1 is lower compared to 300PBZn, but both MAD values increases in a linear fashion. Moreover, the coefficient of variation, related to the dispersity of the data sample, can be used to estimate the average uniformity of a particle set. Larger QCV values correspond to larger size distributions, where a value inferior than 0.3 (or 30%) indicates a relatively homogenous and uniformly sized distribution.¹³¹

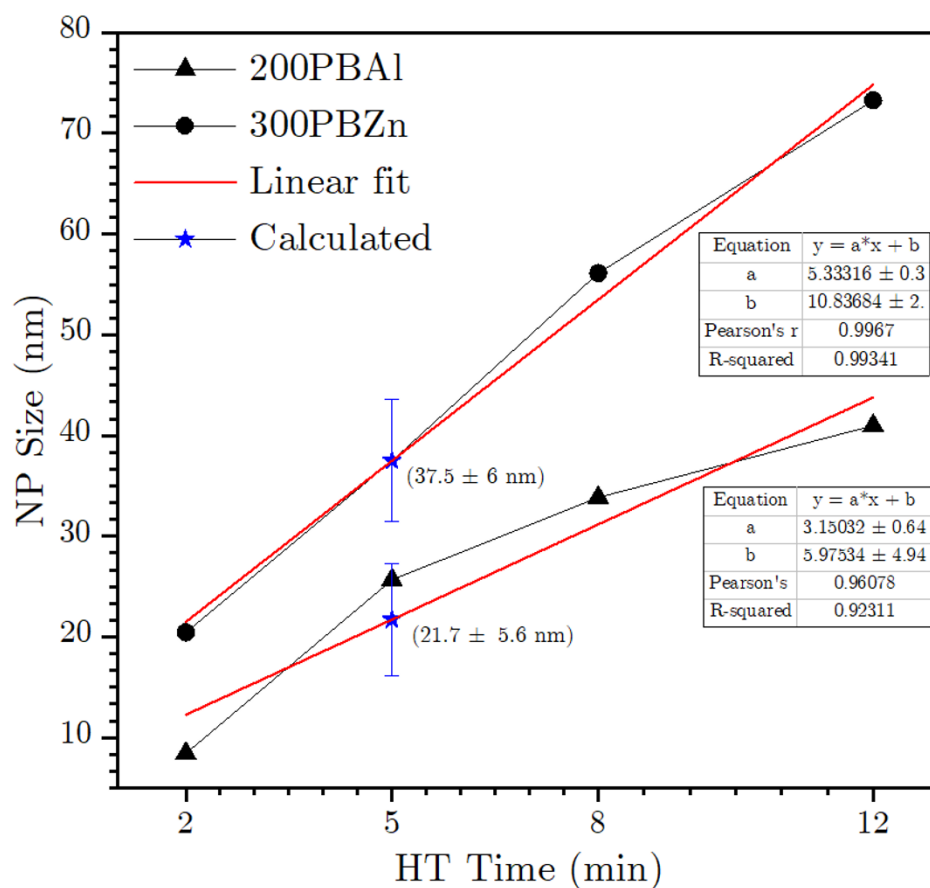


Figure 16. Linear regression fit (red line) of the nanoparticle size median, grown on borophosphate matrices containing aluminum (triangle) or zinc (circle), with their corresponding line equation, Pearson's correlation coefficient (r), and R^2 of each. The calculated NP size for HT time of 5min. for both lattices are represented as the blue star, with estimated standard deviation.

The dispersity variation of nanoparticles grown on 200PBAI increases with rise of thermal treatment time, demonstrating a strong positive linear correlation ($r = 0.94$). The zinc containing matrix, on the other hand, has a large QVC even at the shortest treatment time, with a weak linear correlation with HT time ($r = 0.48$). Withing it, it is apparent that not only nanoparticle size is bigger for 300PBZn matrix, but size variation and dispersity is also higher.

This difference in size particle due to thermal treatment time was also observed in a study performed by Jiménez and colleagues.¹³² They observed an increase in silver

nanoparticle size in their silver-doped phosphate glasses with increased heat treatment temperatures, indicating that higher thermal conditions favors ion mobility and the formation of more nucleation sites and, consequently, growth of nanoparticle.¹³² In the case of 300PBZn, the heighten of temperature influenced positively the diffusion of molecules, and an increased number of nucleation occurred.^{132,133} With prolonged annealing time, these clusters became larger, while new clusters were formed in an increased ratio, compared to 200PBAI, promoting the discrepancy between MAD and QCV values among matrices.

To access the correlation of HT time with nanoparticle size, Pearson's coefficient (Eqn. (1)) was calculated for each matrix. It was found that a strong and positive correlation exists between each vitreous sample ($r = 0.96$ for aluminum samples and $r = 0.99$ for zinc), with statistical significance ($p < 0.05$), represent more thermal treatment time is applied, bigger nanoparticle size is obtained.

However, even though nanoparticle size is directly related to the thermal treatment time applied (increased HT time results in increased NP size), the growth rate is not linear. Aluminum containing matrix, for example, had an initial growth rate of 200% from 2 to 5 minutes, followed by a -32% growth from 5 to 8 minutes and, at last, reached a rate of 21% from 8 to 12 minutes. For Zinc containing matrix, the treatment started with an estimated growth of approximately 83% from 2 to 5 minutes, followed by an estimation of 50% from 5 to 8 min. and, finally, a growth of 8% from 8 to 12 min. This suggests that maximum growth rate for 200PBAI is achieved at a HT time of 5 minutes approximately, while for 300PBZn it occurred at 2 min.

Additionally, the difference of growth rate between the two borophosphate samples corroborates with the NP size dispersity (observed in **Figure 17**) among compositions, and are related with the variance of thermal treatment temperature (200 °C for aluminum and 300 °C for zinc modified matrix), which are associated with the degree of packing of

the vitreous lattice. Sadok and collaborators⁷⁷ studied the effect of the addition of Na_2SO_4 in a sodium borophosphate glass doped with ZnO , to understand the cation mobility. They reported that by increasing sodium sulfate in the glass matrix, the density tended to decrease while molar volume increased, and this is a result of isotropic dissolution of sodium, “opening” spaces in the structure and favoring cation mobility.

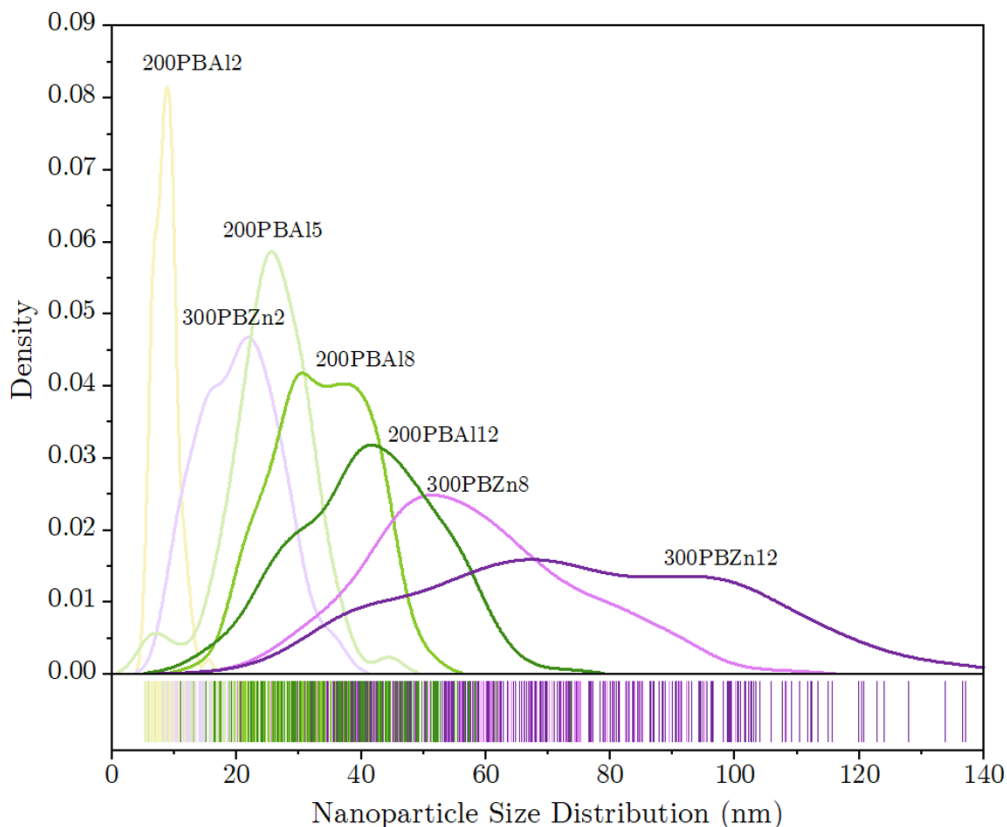


Figure 17. Nanoparticle size distribution of 200PBAI and 300PBZn borophosphate glass sample sets at their respective thermal treatment time (2-12 min).

Nonetheless, Kim and co-workers¹²² investigated the effect of ZnO addition in a borophosphate glass structure, and observed that increasing the content of ZnO in the glass matrix, the density also increased by reducing bond length and reinforcing bond strength in the glass network. Owing to this fact, the atomic packing in the glass structure is mostly responsible for the characteristic of ion mobility, being affected by bond strength, bond length and atomic radius.¹²² An efficiently packed atomic structure is expected to provide higher viscosity and, thus, a reduced rate of mass transport,¹⁰⁰ while an increase

in polymerization is expected to decrease ion mobility with network connectivity also increasing.^{134,135}

As a result of zinc having a shorter atomic radius and a heavier atomic mass than aluminum, it is expected that this glass modifier will result in a denser matrix, making it more difficult for the ions to move in the network. Thereby, this composition requires higher annealing temperatures to achieve Ag^+ reduction to Ag^0 in a satisfactory rate (shorter treatment times, < 20 min.). Within it, bigger particles can be obtained in shorter thermal treatment periods. However, this culminates in a quicker removal of silver ions from the neighboring, making it more difficult to control nucleation expansion process and formation of particles in a reduced diameter.

4.5. Plasmonic Resonance UV-VIS Absorbance

The interaction of light with a substance can result in the absorption of part of this light by the material, part of it may be scattered (Rayleigh scattering, for example) and the rest may be transmitted through the medium it is found.¹³⁶ Some useful applications related to light scattering can be exploited using metallic nanostructured glasses, since metal nanoparticles, in the range of 100 nm, scatter light more efficiently due to the excitation of localized surface plasmons which leads to optical resonance phenomena.¹³⁷ This resonance is a response to the mutual oscillation of conduction electrons presented on the boundary of a metal, in which an optically active dipole field configuration is presented.^{138,139} For silver, gold and copper nanoparticles, this dipole resonance occur in the ultra-violet and visible (UV-VIS) region and can be investigated by analyzing the metallic nanoparticles absorbance spectra in this region.¹³⁹ Withing it, UV-VIS absorbance spectroscopy was used to investigate the surface plasmon of the silver nanoparticles grown on the borophosphate matrices.

The spectra collected for all vitreous samples, 200PBA1 and 300PBZn, without annealing time (0 min.) and after thermal treatment for 2 min, 5 min, 8, and 12 min (each) are shown in **Figure 18** for aluminum (upper curves) and zinc (lower curves). The objective is correlate the difference in the plasmon band with nanoparticle size. The position and intensity of the surface plasmon resonances are dependent on few factors such as shape and size of nanoparticles. Thus, UV-VIS spectra can be associated regarding how annealing time and temperature influences nanoparticle growth and formation.¹⁴⁰

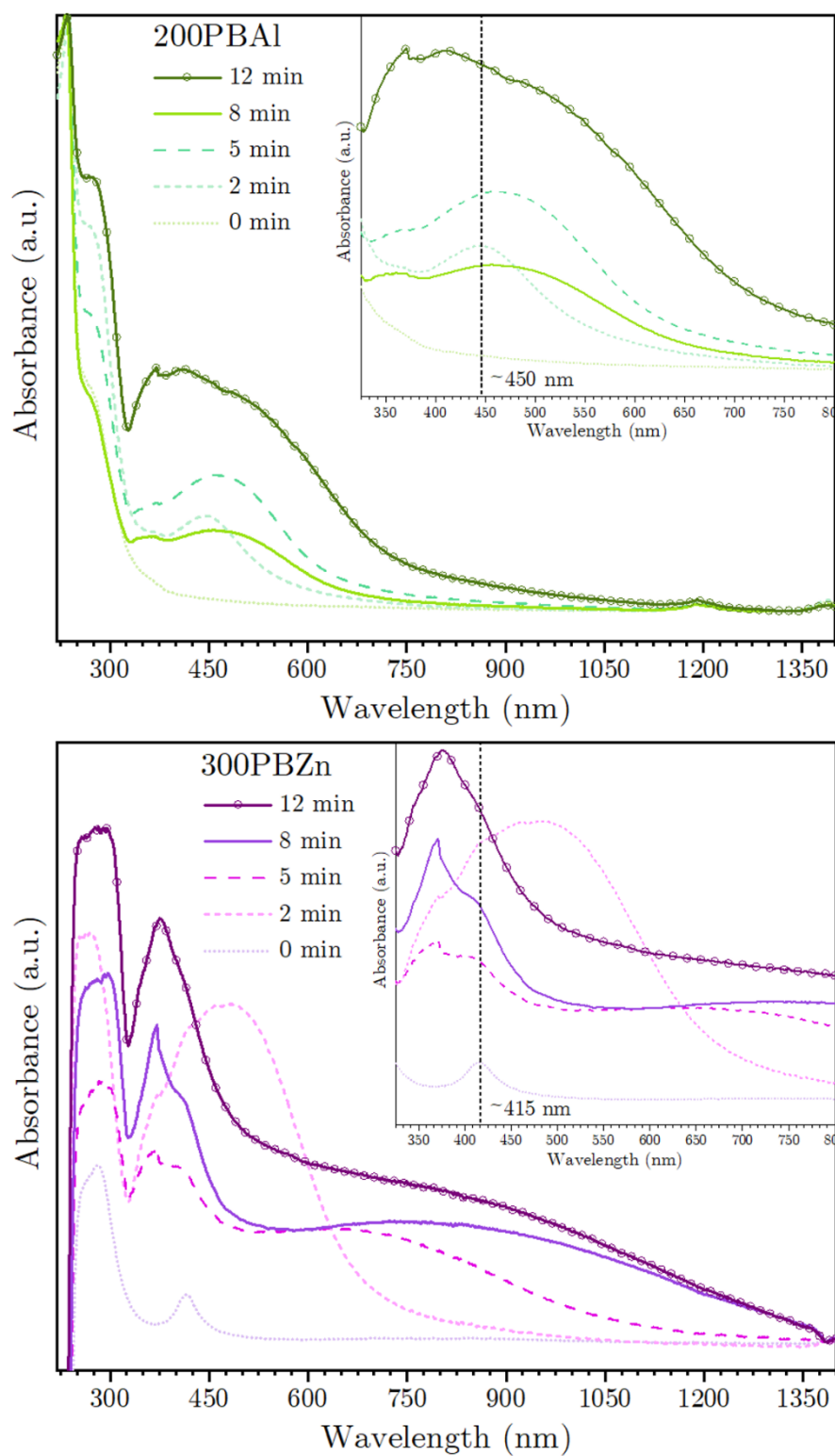


Figure 18. UV-VIS absorbance spectra of 200PBAI (uppermost) and 300PBZn (lowermost), at their respective thermal treatment time (in minutes).

A very intense band can be seen between 250–300 nm for both glass compositions at all annealing times, and is related to the absorption wavelength of borophosphate glass matrices.¹³⁶ Besides this strong band, no apparent band is seen for 200PBA1 glass without thermal treatment. The first plasmon band is seen just after a HT time of 2 min., at around 447 nm. This band broadens, shifts to higher wavelengths and it also tends to increase in intensity as the nanoparticle size also increases.

The increase in diameter results in a red-shift of the peak plasmon resonance and can be explained as there is a change in the free conduction electrons density on the nanometallic surface with the variation of size and modification of geometric shape of silver nanoparticles during thermal processing.^{136,141,142} This event was also observed by Park *et al.*,⁵⁶ in which an increase in their gold nanoislands thickness from 4 to 8 nm shifted the plasmon band to higher wavelength numbers. However, the NP size may not be the only aspect to be considered the cause of the shift, since the geometry shape of silver nanoparticles grown on the glass surface differs from an ideal sphere.¹⁴³

The increase in AgNP size of our borophosphate glasses due to prolonged annealing time rises the particle dispersity due to nanoparticle coalescence and cluster formation, as observed in the topic 4.4. As a result, it leads to delocalization and distribution of conduction electrons near each particle surface, resulting in the shift of SPR peak towards lower energies. This effect can also cause the peak to lower in intensity, broaden and/or result in the formation of another peak at longer wavelengths. As seen in **Figure 18** (top), 200PBA1 SPR peak shifts from 450 to about 480 nm, broadens and have a second SPR peak appearing at around 580 nm for annealing time of 12 minutes, corroborating with what has been discussed. The decrease in intensity for the 200PBA18 can be due to the delocalization of free conductive electrons with coalescence of nanoparticles.

Controversially as seen in 200PBA1, the zinc glass sample set present a small band at ~415 nm for sample with no thermal treatment (0 min.). This band does not shift

significantly after nanoparticle growth. After thermal treatment of 2 min., it is possible to see a band forming at around 370 nm associated to the first plasmon band for this matrix, After HT of 5 minutes, the delocalization of the free conductive electron as nanoparticle coalesce (observed in SEM analysis) can interfere in plasmon resonance intensity. Furthermore, these resonance bands are a result of the superposition of individual nanoparticles resonances, and the variation in size (PSD) may result in a range of absorption frequencies, contributing to band broadening.¹³⁹

4.6. Enhancement Factor

Surface-enhanced Raman scattering (SERS) is a very sensitive spectroscopic technique that offers excellent specificity and a fine multiplexing ability. The plasmonic resonance effect, which is responsible for providing the Raman signal enhancement, is achieved by the nanoscopic metallic surface of our vitreous matrices. This surface is composed of silver nanoparticles self-assembled on top of the vitreous substrate (planar metallic structures), with size varying according to its annealing time. The enhancement related to the plasmonic effect is dependent of several factors, such as nanoparticle size and shape, also of the intrinsic Raman properties of a molecule and its concentration. According to this, Raman signal enhancement can be calculated based on signal intensity and molecule concentration adsorbed on the metallic surface, providing an estimative of the overall improvement of a substrate. For this reason, SERS activity was study considering each borophosphate glass matrix (200PBAI and 300PBZn), and Cresyl Violet Perchlorate (CVP), a basic and well-known dye, was used as a standard to compare the enhancement efficiency of each heat treatment time (0-12 min.).

Greater enhancement values occur when there is an overlap between the excitation laser wavelength and the nanoparticle plasmon resonance, also when matches with the reporter molecule's emission maximum.¹³⁰ As the wavelength of Cresyl violet has its

maximum emission close to 600 nm, the chosen excitation line was 532 nm. Therefore, the identification of the best laser excitation line for SERS activity on the silver nanoparticles was necessary.

Figure 19 shows Raman SERS spectra curves of CVP on 200PBAI (a) and 300PBZn (b) glass matrix for samples treated at 2, 5, 8, and 12 min.. The fig. also shows, for the thermal treatment time investigated, the comparison of CVP spectra at each concentration, ranging between 1×10^{-6} , 1×10^{-3} and 1,0 mols/L (front to back).

One broad peak of CVP can be seen around 592 cm^{-1} and is related to bending modes of its central aromatic heterocyclic ring.¹⁴⁴ This peak was selected to further investigate the SERS effect as it was the most intense and defined among others. CVP spectra (at the range of 580-605 nm) at the three different concentrations (1 M, 1.10^{-3} M and 1.10^{-6} M) is summarized in **Figure 20** (a) using 200PBAI and (b) using 300PBZn sample sets, in which just a polynomial baseline correction was accomplished with no further spectra treatment performed.

The detection of normal CVP Raman signal (without SERS matrix assistance) were achieved at very low intensity only at the highest molarity (1 M). Further, it is possible to observe a continuous but non-linear increase in Raman signal intensity of CVP on the 200PBAI matrix with increasing HT time. Its highest intensity was found at 8 min, while for 300PBZn matrix, highest intensity was achieved at 5 min.

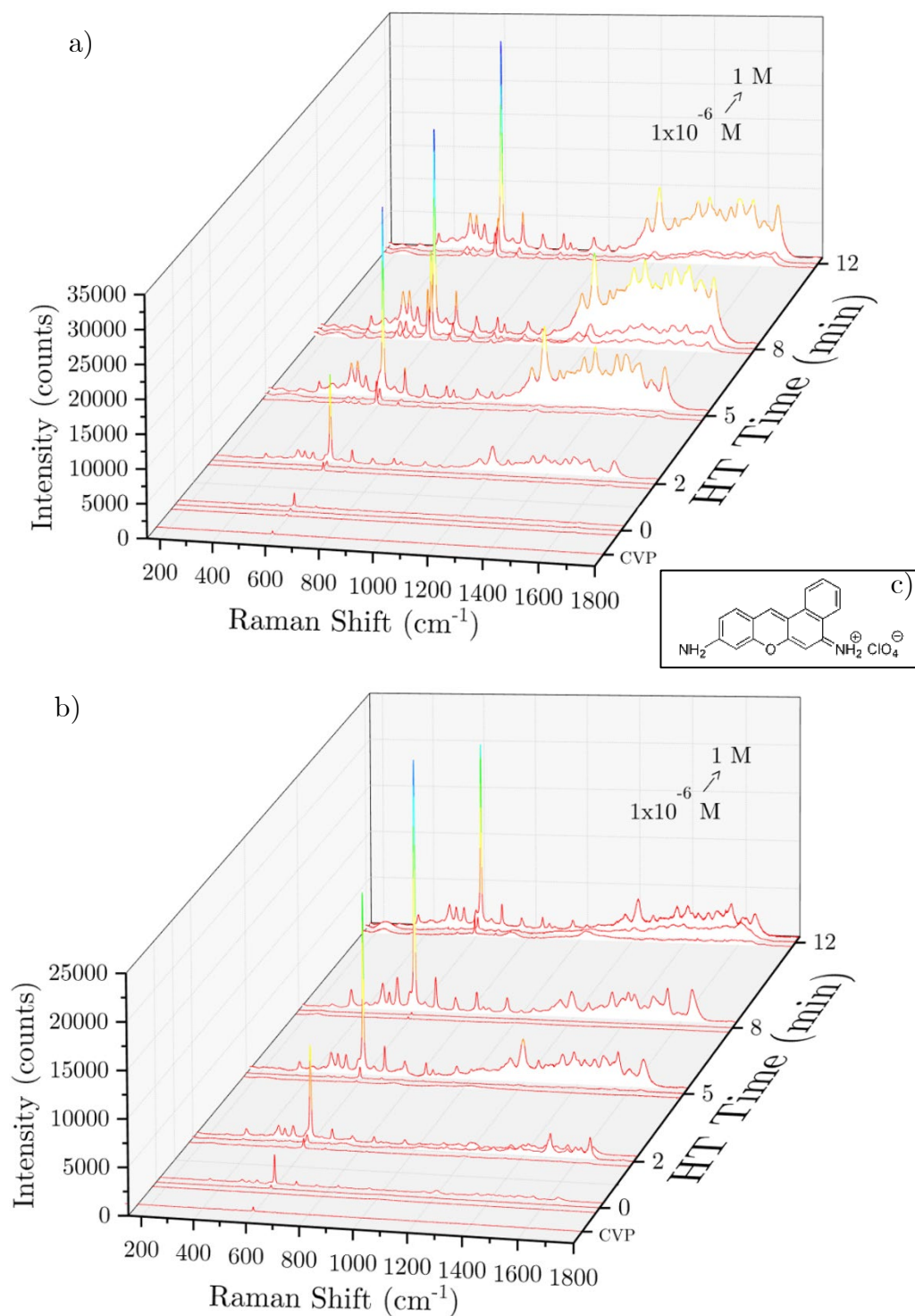


Figure 19. Normal Raman spectra of Cresyl Violet Perchlorate (CVP) at 1 M concentration and its enhanced Raman spectra obtained by SERS using 200PBAI set (a) and 300PBZn set (b) at the different annealing times (2 – 12 min), with concentrations of 10^{-6} M, 10^{-3} M and 1 M (front to back). (c) Chemical structure of CVP.

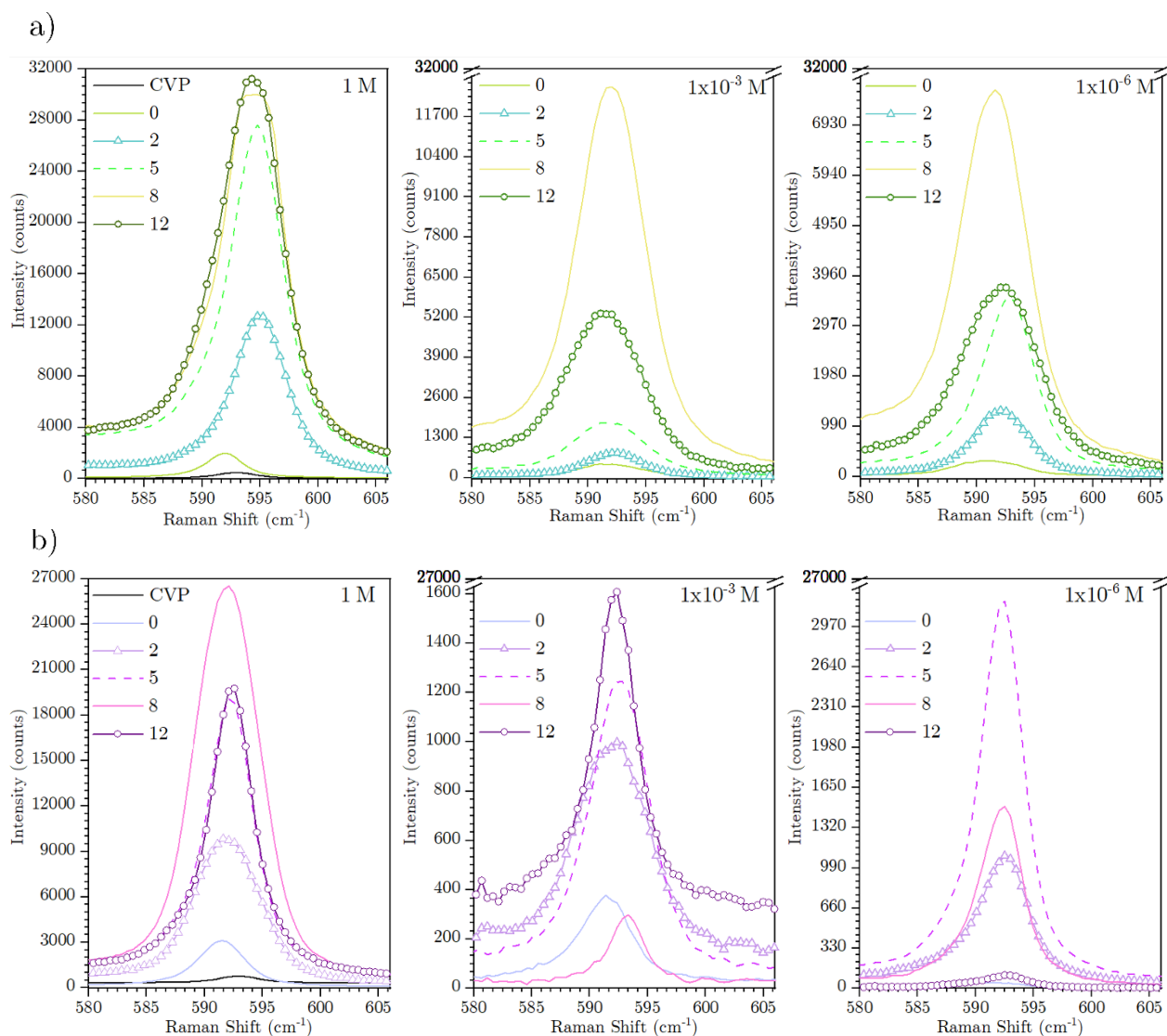


Figure 20. SERS of the CVP most intense peak (around ~ 592 cm^{-1}), at concentrations 1, 1×10^{-3} and 1×10^{-6} mol.l^{-1} , obtained on 200PBAI (a) and 300PBZN (b) vitreous substrates, at their respective annealing times (in minutes). The scales were adapted (cut) for better visualization.

Interestingly, the intensity for 200PBAI at 8 min. treatment has shown similar values compared to the intensity obtained for 300PBZn sample thermally treatment for 5 min, as observed in **Figure 21** for $1 \mu\text{M}$. They correspond to nanoparticles of $\sim 34 \pm 6$ nm and 38 ± 6 respectively (refer to **Table 7**). However, to further confirm the preference of this maximum intensity peak value in this nanoparticle size range, an average of the intensity in a diverse number of points is necessary.

For 300PBZn samples, the highest intensity of CVP at 1 M was obtained for matrix treated for 8 min. (-56 ± 13 nm). By lowering the Cresyl violet concentration to 10^{-3} and 10^{-6} mol.l⁻¹, the highest peak intensity altered from 200PBA12 to 200PBA18, indicating that the preferred size of our self-support AgNP for SERS effect is close to 34 nm for aluminum modified borophosphate glass. On the other hand, for zinc modified matrix, lowering the CVP concentration occurred in highest peak intensity of 10^{-3} M solution being detected by 300PBZn12 followed by 300PBZn5 at 10^{-6} M, with no regularity or pattern observed for the signal intensity behavior through concentrations.

Subsequently, the enhancement factor is considered one of the most important numbers for characterizing the SERS effect, especially for practical applications where it is important to know the magnitude of enhancement it can be achieved or expected.⁴⁸ The intensity values of CVP peak, obtained on each matrix for all thermal treatment time applied, were thus used for the calculation of the overall enhancement effect of the glass substrates, seen in **Figure 21** and with values summarized in **Table 8**. In regard of the strongest peak at -592 cm⁻¹, the RAMAN intensity values were used in Eqn. (5) to obtain the SERS substrate enhancement factor (SSEF) as described by authors.^{38,48,51,92} The SSEF considers the average number of molecules contributing to the signal in a certain area upon laser contact

The highest SSEF calculated was about 1.7×10^7 for 200PBA18 and 7×10^6 for 300PBZn5, which are 1-3 orders of magnitude higher than the reported for Ag nanoparticles with similar sizes ($-35 - 70$ nm).^{29,36,145} This difference can be attributed to the nanoparticles “hot-spots” presented in the substrate, also contributing for SERS enhancement, as interparticle distances and arrangements can affect the intensity of interparticle electromagnetic coupling and, thus, the degree of SERS enhancement.¹⁴⁶

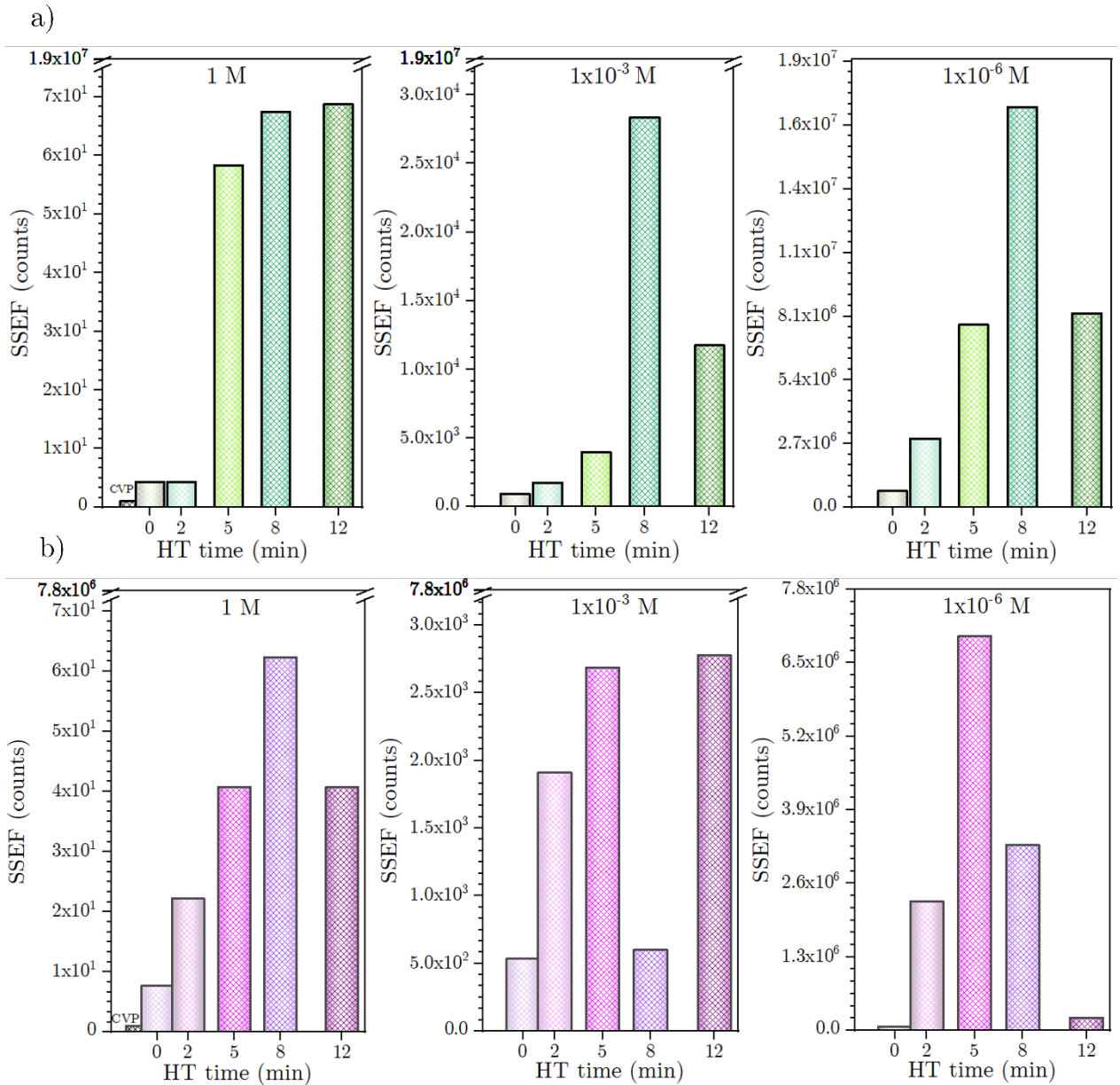


Figure 21. SERS substrate enhancement factor of borophosphate glasses modified with aluminum (a) and zinc (b) according to their respective heat treatment time (in minutes) and CVP concentration (1 , 1×10^{-3} and 1×10^{-6} mol.l⁻¹) compared to normal Raman signal of CVP obtained at 1 M. The scales were adapted (cut) for better visualization.

Wang *et. all.*,¹⁴⁷ fabricated a diamond silver nanostructure array with highly uniform inter-nanoparticle gaps ranging from 30 to 150 nm. They demonstrated that this extremely homogeneous substrate provided an enhancement factor on the order of 10^7 for a 30 nm gap when analyzing Rhodamine 6G, as SERS intensity being mostly depended on

the design patterns. Between 200PBA18 and 300PBZn5, which accounted for SSEF of 1.7×10^7 and 7×10^6 respectively, the particle sizes are expected to be similar, as demonstrated by SEM analysis (refer to topic 4.4), but inter-nanoparticle distance may differ, since coalescence of particles during growth process is more prevalent in zinc modified glass matrix. Another important aspect that may have interfered with enhancement effect is the presence of silver oxide layers on the nanoparticles. Han and collaborators,¹⁴⁸ for instance, observed that SSEF sharply dropped with increasing in Ag_2O thickness on their silver 48 nm nanocolloids, in which up to 3 orders of magnitude decrease from its EF_{max} of 10^6 was examined.

Table 8. SERS substrate enhancement factor of each thermal treatment time calculated at three different CVP concentrations for the peak at -592 cm^{-1} .

Peak 592 (cm^{-1})		SSEF		
		CVP (mol.L^{-1})		
Substrate	HT Time (min)	1	1×10^{-3}	1×10^{-6}
200PBA1	0	4.3	9.2×10^2	6.9×10^5
	2	4.3	1.7×10^3	2.9×10^6
	5	5.8×10^1	4.0×10^3	7.7×10^6
	8	6.7×10^1	2.8×10^4	1.7×10^7
	12	6.9×10^1	1.2×10^4	8.2×10^6
300PBZn	0	7.7	5.3×10^2	7.2×10^4
	2	2.2×10^1	1.9×10^3	2.3×10^6
	5	4.1×10^1	2.7×10^3	7.0×10^6
	8	6.2×10^1	6.0×10^2	3.3×10^6
	12	4.1×10^1	2.3×10^3	2.2×10^5

Source: Self-elaborated.

4.7. SERS Analysis of Adsorbed Protein

Aiming to investigate the ability of our borophosphate glass substrates for assessing enhanced biological Raman spectra, we investigated SERS effect of two proteins using both (aluminum and zinc modified) matrices at their two greatest SSEF identified. Since the enhancement effect is highly dependent of particle interaction between the analyte and

the metallic surface, three label-free methodologies for direct biomolecule adsorption were also investigated.

4.7.1. Single step incubation

The simplest approach studied involved the SERS detection of bovine serum albumin (BSA) and anti-Human interleukin 2 (anti-HIL2) antibody by natural drying, with no incubation was performed and aqueous solution was removed naturally by evaporation at room temperature. The spectra collected from the biological samples are simplified in **Figure 22** (a) for BSA and (b) for anti-HIL2. BSA SERS spectra, collected on the SERS substrates are being further examined with normal Raman spectra (without SERS substrate) of the powdered BSA sample and respective borophosphate glass used. Anti-HIL2 enhanced spectrum obtained on the SERS substrates are further compared with normal Raman spectra of the anti-HIL2 antibody and carbonate buffer solution.

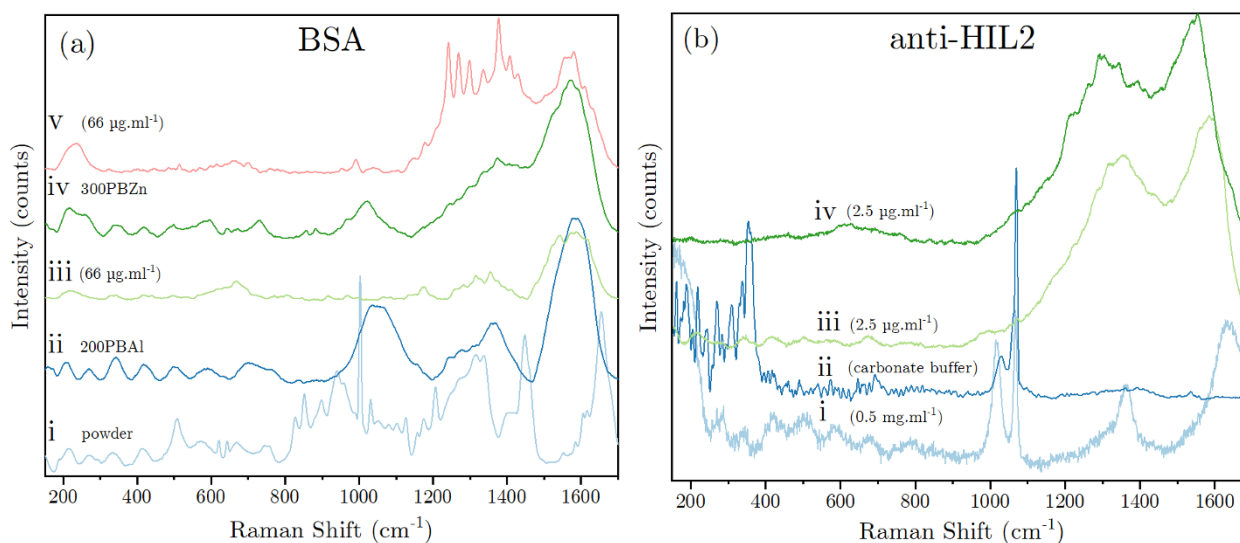


Figure 22. (a) Normal Raman spectra of BSA (i), 200PBA18 (ii) and 300PBZn5 (iv), with respective BSA SERS spectra collected on 200PBA15 (iii) and 300PBZn (v). (b) Normal Raman spectra of anti-HIL2 (i) and carbonate buffer (ii), with respective SERS spectra collected on 200PBA18 (iii) and 300PBZn5 (iv). SERS were collected subsequent ambient drying.

Figure 22 (a-i) shows the Raman spectra (not SERS enhanced) of BSA collected from powder sample. The disulfide bridges presented in the protein structure are presented in the lower frequency region ($\sim 500\text{ cm}^{-1}$). The peaks at $870\text{-}1150\text{ cm}^{-1}$ region are related to the aromatic residues in the protein and can be assigned to the backbone skeletal stretch ($\text{C}_\alpha\text{-C}$, $\text{C}_\alpha\text{-C}_\beta$ and $\text{C}_\alpha\text{-N}$). The strong peak occurring at approximately 1000 cm^{-1} can be associated to the side chain of the Phe amino-acid.^{138,149,150}

Figure 22 (a-ii, iv) shows the Raman spectra of pure glass matrix modified with aluminum and zinc, respectively. The Raman-SERS spectra of 200PBA18 and 300PBZn5 adsorbed with BSA are also shown in **Figure 22** (a-iii, v), respectively. In both spectra we can observe a significant contribution of the glass vibrational modes (a-ii for aluminum; a-iv for zinc containing matrices) between 1200 to 1650 cm^{-1} .

Furthermore, in order to determine the spectral contribution due to the buffer, **Figure 22** (b-i) displays normal Raman spectra of anti-HIL2 antibody (with no SERS substrate), compared with spectrum of carbonate buffer spectra (**Figure 22** b-ii), and respective antibody SERS spectra obtained on 200PBA1 (b-iii) and on 300PBZn (b-iv). It is evident that the peaks observed in the region ranging from 1000 to 1100 cm^{-1} are associated to the carbonate buffer and are assigned to vibrational modes of CO_3^{2-} .¹⁵¹ Additionally, as can be seen in **Figure 22** (b-iii, iv), SERS spectra of anti-HIL2 also shows contribution modes from the vitreous substrate between 1200 to 1650 cm^{-1} .

To further investigate spectra correlation and maximize the covariance of spectral data, principal component analysis (PCA) was performed. **Figure 23** and **Figure 24** shows the PCA analysis of BSA and anti-HIL2 Raman-SERS measurements, respectively. The PCs 1, 2 and 3 were selected for BSA data, explaining 97.5 % of the variance.

In **Figure 23**, the PCA scores of the diluted SERS BSA data presented a cluster (green circle) in the same region of the BSA pure Raman spectra (light blue score), representing that the maximum variation of each spectrum are similar. This indicates that

SERS spectra of BSA is related to the Raman spectra (without SERS substrate) of the protein. Furthermore, the scores related to the glass matrices can be observed separated from the protein cluster (dark and light purple at the left), indicating that the matrices had little influence in SERS spectra. This demonstrates the potential of PCA in associating BSA spectra with their respective SERS, revealing that short incubation in a “salt-free” aqueous environment is a promising application to investigate biomolecule. Additionally, the spectra obtained for the lower concentration (red circle) (1 nM) is close to the cluster but more dispersed, indicating a promising application of this analysis in separating different concentrations. Analysis at lower concentrations did not yield in satisfactory spectra.

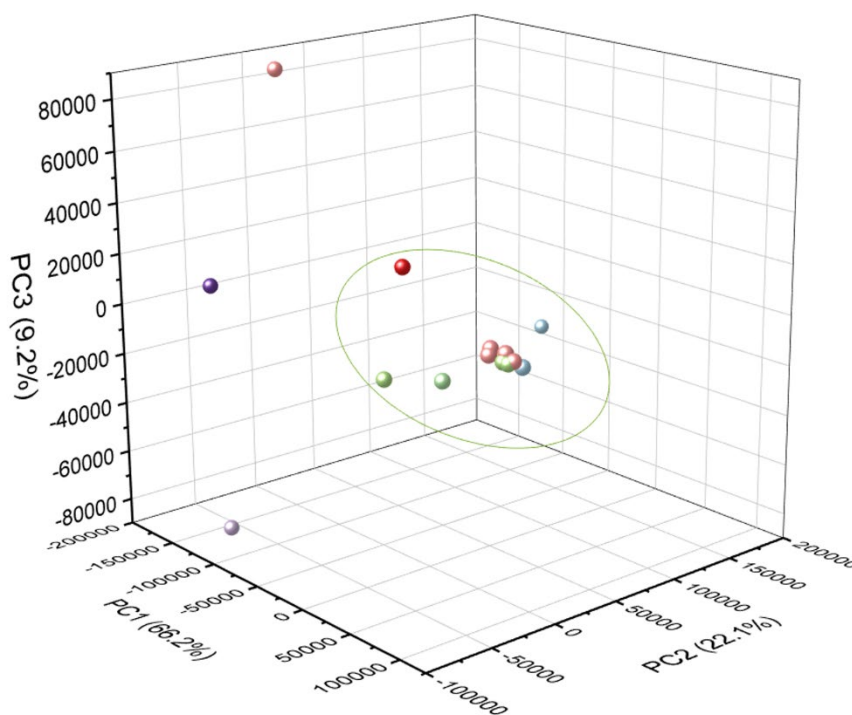


Figure 23. PCA scatter plot of BSA samples and vitreous substrates. ● (light purple) 200PBA18, ● (dark purple) 300PBZn5, ● (light blue) BSA Raman spectra, ● (light pink) 300PBZn5 + BSA 1µM, ● (red) 300PBZn + BSA 1nM, ● (light green) 200PBA18 + BSA 1µM

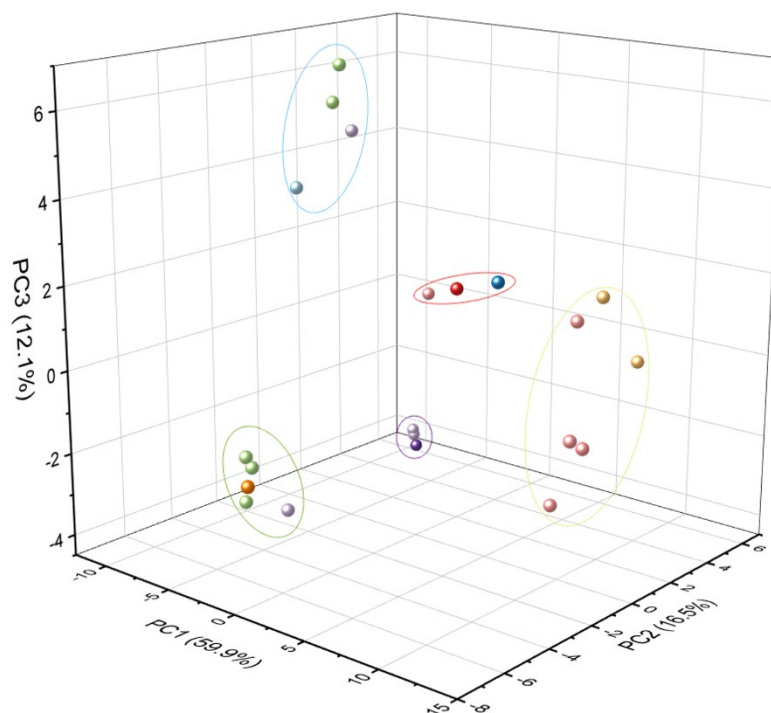


Figure 24. PCA scatter plot of anti-HIL2 samples and vitreous substrates. ● (light purple) - HIL2 antigen, ● (light green) anti-HIL2, ● (orange) antibody + antigen, ● (light pink) 200PBA18 + anti-HIL2 2.5 $\text{pg}\cdot\text{ml}^{-1}$, ● (light yellow) 200PBZn5 + anti-HIL2 $\text{pg}\cdot\text{ml}^{-1}$, ● (red) 200PBA18, ● (dark blue) 300PBZn5, ● (light blue) carbonate buffer, ● (dark purple) microscope slide.

Subsequently, PCs 1, 2 and 3 were selected to analyze HIL2 data, with a total of 88.5 % of the variability being explained. A total of five cluster could be observed from the PCA plot for anti-HIL2 spectra (**Figure 24**), with scores lightly dispersed. The cluster marked by a green circle contains mainly antibody scores (green), with one score representing antigen + antibody spectra (orange), and another related to HIL2 antigen spectra (light purple).

At the top of the plot, in the blue circle, there are scores related to antibody alone (green), antigen alone (light purple) and to the carbonate buffer spectra (light blue). The purple circle contains scores of antigens (light purple) and one related to the microscope slide (dark purple). The SERS scores collected on the vitreous substrates are grouped and marked with a yellow circle (light pink–200PBA18, light yellow–300PBZn5).

The Raman spectra of vitreous substrates (without protein adsorption) are grouped (red circle) close to the region of the yellow circle, with one of the scores representing 200PBA1 + antibody spectra (light pink). These correlations indicate that, even with no visual spectra association, it is possible to compare similar aspects of the biological data. However, no correlation between scores of anti-HIL2 normal Raman spectra and SERS spectra obtained with vitreous matrices is seen, while there are associations of anti-HIL2 associated with carbonate buffer score. Furthermore, antigen scores are mostly correlated with the microscope slide spectra, and anti-HIL2 SERS spectra (either from aluminum or zinc modified glasses) are grouped close to the normal Raman spectra of the borophosphate matrices. This represents that a strong interference from the SERS substrate/glass slide and from the buffer solution can be present in anti-HIL2 biomolecule detection under buffer condition.

4.7.2. Antibody immobilization

In order to optimize anti-HIL2 adsorption, antibodies were immobilized by submitting protein solutions to incubate with 200PBA18 and 300PBZn5 samples prior to analysis. The spectra, shown in **Figure 25**, were collected for each concentration of solution, considering anti-HIL2 standard at $2.5 \mu\text{g}\cdot\text{ml}^{-1}$ and antibody incubated with four-fold serially diluted HIL2 antigen, ranging from $800 \text{ pg}\cdot\text{ml}^{-1}$ to $12.5 \text{ pg}\cdot\text{ml}^{-1}$.

However, during spectra collection, few aluminums containing vitreous samples were lost, and could not be included in the results. For this reason, only spectra related to incubated samples (anti-HIL2 and anti-HIL2 + HIL2 ranging from 12.5 to $800 \text{ pg}\cdot\text{ml}^{-1}$) on 300PBZn5 substrate will be shown, with the results being presented in **Figure 25**.

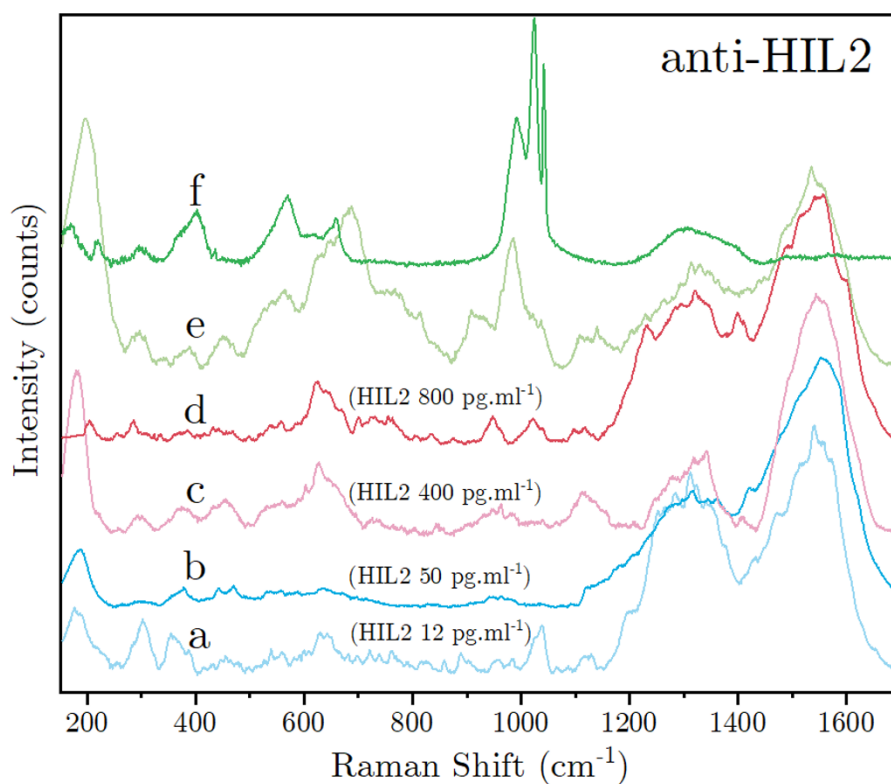


Figure 25. SERS of immobilized anti-HIL2 incubated with HIL2 antigen at 12.5 pg.ml⁻¹ (a), 50 pg.ml⁻¹ (b), 200 pg.ml⁻¹ (c), 800 pg.ml⁻¹ (d), anti-HIL2 antibody (e) and normal Raman of anti-HIL2 (f).

As noticed in the adsorption processes related previously, the region between 1200 to 1650 cm⁻¹ of the Raman shift is also presented and may show correlation to the spectra of vitreous substrate (similarly as observed in **Figure 22**). Normal Raman spectra of anti-HIL2 antibody (**Figure 25** (f)) shows three peaks between 990 and 1050 cm⁻¹. Furthermore, it is observed that a peak at the lowest frequency region (~200 cm⁻¹) is very prominent. This region was previously attributed to silver oxides presented on the borophosphate glass substrates (refer to **Table 5**), and its presence indicates a higher oxidation state of silver particles in the presence of buffer solutions. The covariance between antigen concentration and antibody spectra was further investigated with PCA and can be seen in **Figure 26**.

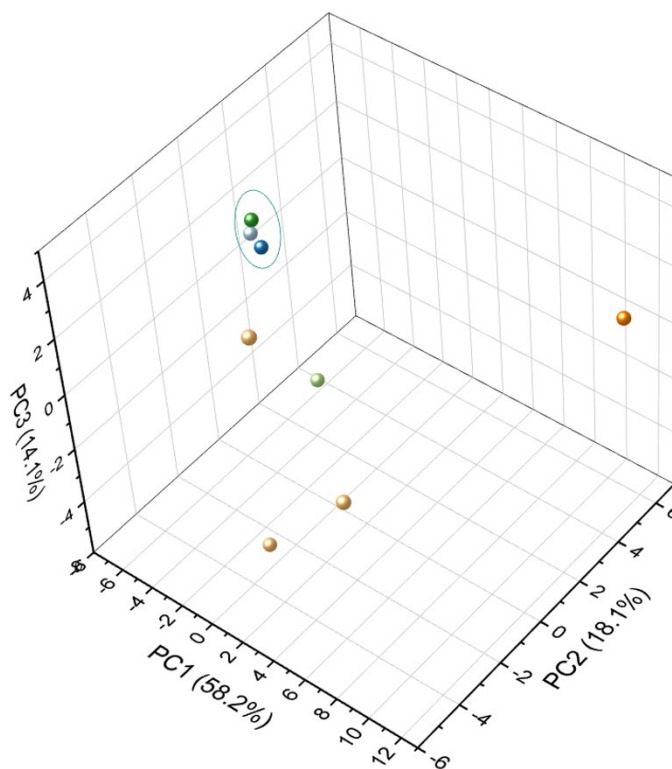


Figure 26. PCA scatter plot of immobilized anti-HIL2 antibody (on 300PBZn5) conjugated with HIL2 at different concentrations. ● (light blue) HIL2 12.5 pg.ml⁻¹, ● (dark blue) HIL2 50 pg.ml⁻¹, ● (light green) HIL2 200 pg.ml⁻¹, ● (dark green) HIL2 800 pg.ml⁻¹, ● (light yellow) immobilized anti-HIL2, ● (orange) normal Raman of anti-HIL2.

The principal component analysis of the immobilized antibodies spectra was plotted based on the PCs 1, 2 and 3, corresponding to a total of 90.4% of the covariance being explained. The SERS anti-HIL2 antibodies spectra (not conjugated), obtained with 300PBZn5 substrate, are represented as light yellow scores. As can be seen, they are not grouped, representing that a considerable difference between spectra exists. Alternatively, immobilized antibodies at the presence of the HIL2 antigen clustered, having one outlier score related to HIL2 400 pg.ml⁻¹ (light green). To further investigate the ability of the technique in differentiating protein at different concentrations, optimization of the technique (including immobilization and spectra collection) must be considered, with data of each dilution being obtained in triplicate.

4.7.3. Discussion

A direct protein adsorption followed by SERS analysis was investigated in order to check the performance of our substrates in biomolecule detection using a simple, label-free approach. It was observed that one condition, out of the three tested, efficiently enhance the protein Raman signal and resulted in satisfactory PCA analysis, and another having demonstrated a promising application. Notwithstanding, these results were presented comprising few data scores (or few spectra collections), and a more categorical result considering a greater sample number is essential.

In summary, the adsorption of BSA on the silver surface presented better SERS results than adsorption of incubated anti-HIL2 (with or without HIL2 antigen conjugation), while adsorption of anti-HIL2 with short incubation could not be conclusive. Few aspects can be related to the overall unsatisfactory SERS results: (i) metallic silver surface neutrality; (ii) oxidation of silver nanoparticles; (iii) salt competition; (iv) protein degradation/denaturation during analysis.

As highlighted by Jazayeri *et. al.*,⁴⁰ for protein adsorption via non covalent bonds, physical interactions must occur, either ionically or hydrophobically. However, since our silver nanoparticles were obtained by reduction under H₂ atmosphere, it is expected that pure metallic particles of Ag⁰ (with no charge) are presented. Bovine serum albumin is a circulating protein that easily adsorbs on a different range of surfaces due to its molecule structure.^{39,152} This protein has many binding sites that can hydrophobically adsorb on the silver nanoparticles.³⁹ The anti-HIL2 antibody, on the other hand, is a small protein, with few binding sites and mostly having high affinity to its antigen. This may have influenced the low affinity for the silver nanoparticle surface.

Additionally, exposure to ambient air during sample handling and preparation may have led to nanoparticle oxidation, observed in Raman spectra around 200 cm⁻¹ (refer to **Table 5**), and in the presence of buffer for prolonged periods, oxidation of silver

nanoparticles may also have occurred, as seen in **Figure 25** ($\sim 200\text{ cm}^{-1}$). Silver oxide layers interfere in the SERS effect and protein adsorption as it introduces a reasonable hydrophilicity to the nanoparticles, forming a solvation layer.¹⁵³ As Raman enhancement signal is highly dependent on the distance between analyte and metallic surface, this mechanical barrier could explain the difficulty in accessing spectral information of the anti-HIL2 antibody for ambient drying, with short incubation.

On the other hand, the buffer choice can depress protein adsorption by retarding the biomolecule interaction through “competition”. For example, it was examined by authors¹⁵⁴ that PBS buffer interferes in the adsorption ratio of BSA as negatively charged phosphate ions in PBS buffer tend to adsorb on the solid surface and retard the approach of the also negatively charged BSA ($\text{PI} = 4.7$).¹⁵⁴ In the SERS study of biomolecules, BSA was prepared in a “salt-free” aqueous solution, compared to the carbonate buffer solution used for the antibody adsorption. As observed in the approaches that used buffer solutions, interaction of the salt ion with nanoparticle was pre-emptive over biomolecule adsorption. It must also be considered that nanoparticle degradation (lixiviation from the glass surface) may have occurred due to high buffer pH.

Furthermore, direct detection of a biomolecule, relies on the analysis of its intrinsic Raman signature, which may be related to amino acids with aromatic rings (Trp, Tyr, Phe) and their amide groups as their common vibration modes are symmetric and, thus, Raman active.^{138,150} Since the molecular structure must remain adjacent to the metal nanoparticles (in the range of 1-4 nm) for significant SERS enhancement, the amplified signal will correspond to vibrations of the closest bonds on a metallic surface.¹⁵⁵ The dependence of nanoparticle distance with biomolecule can result in protein conformational changes occurring during SERS measurements. This is because a direct contact between proteins and metallic nanoparticles has shown to cause denaturation and loss of function, probably due to the strong heat occurring from the LSPR phenomena. As a result, the

native Raman spectra of a biomolecule will not match with the respective SERS spectra, making it difficult to further analyze the spectral variances.¹³⁸

At last, it was possible to observe dissimilarities in the SERS spectra compared to Raman spectra of proteins collected without the SERS substrates. This can be a consequence of different molecular orientations (or, to some degree, loss of structure), resulting in spectra fluctuations, such as frequency shifts, peak intensity variations, peak broadening and appearance and disappearance of Raman signal.^{60,138} It can be inferred from the irregular protein spectra that adsorption is not specific, with no preferred orientation being adopted.

Conclusions

In order to elucidate the difference between two compositions of silver doped borophosphate glasses thermally treated and the efficiency in SERS application, this work proposed three lines of research: (i) characterization of glass matrices and silver nanoparticles according to the adopted thermal treatment time, (ii) investigation of SERS performance with overall enhancement factor in respect of a standard molecule and (iii) study the performance of our vitreous substrate in detecting biomolecule based on three direct approaches for biomolecule adsorption.

It was found that the main differences between matrices are related to the degree of packing and thermal stability of the vitreous substrates, being direct correlated to nanoparticle growth and SERS enhancement. The employed techniques (XRD, DSC, Raman and FTIR) for characterizing the structure of 200PBA1 and 300PBZn found little correlation to matrix changes in response to thermal treatment. While techniques employed to characterize nanoparticle (SEM and UV-VIS) demonstrated that AgNP grown from 300PBZn presented its higher growth rate at the HT time of only 2 minutes, and increased HT time resulting in higher and more dispersed nanoparticles.

Additionally, both sample sets at all thermal treatment times had SERS performance investigated in the presence of CVP. It was demonstrated that highest SSEF was calculated for 200PBA18 sample (1.7×10^7), while highest enhancement for 300PBZn8 (7×10^6) was observed to be in the same nanoparticle size range (34 and 37 nm, respectively). Overall SSEF of 200PBA1 sample set was higher due to lower nanoparticle size distribution. However, SERS enhancement factor is still not much higher than the founds in the literature.

Furthermore, BSA and anti-HIL2 SERS detection based on a direct approach demonstrated to be promising when analyzing the results with principal component analysis. However, biomolecule detection in the presence of buffer solution displayed challenges related to salt competition for the metallic surface and nanoparticle oxidation.

This work presents the first study comparing borophosphate glasses modified with two distinct oxides (Al_2O_3 and ZnO) for silver nanoparticle growth, with investigation of the potentiality in applications as SERS substrate for biomolecule detection. Within it, new perspectives for the future arise, associated to:

- (i) Investigation of the true degree of packing, density, viscosity and conductivity of matrices to further understand how ion mobility is affected by the lattice and how it can help in improving nanoparticle growth at a more controlled rate.
- (ii) Definition of better parameters (such as temperature) of thermal treatment to achieve a more homogeneous particle size dispersion, aiming reduced inter-particle distance without coalescence for increased SERS effect.
- (iii) Examination of the silver nanoparticle surface in response to pH variations and salt concentrations, elucidating the best parameters for lower particle degradation/interference.
- (iv) Investigation of the vitreous substrates affinity with different biomolecule structures. For this future perspective, it is important to already have elucidated the interference of buffer solutions and pH variations with nanoparticle, understanding what the limitations in biomolecule interaction are.
- (i) Detailed study of the vitreous substrate ability in detecting enhanced biomolecule spectra and (under optimum conditions), varying concentration and samples type for elucidate the ability in differentiating distinct biomolecules, aiming further clinical analysis application.

APPENDIX A

Theoretical Background

A.1. X-Ray Diffraction

X-Ray Diffraction (XRD) is a technique used to measure the crystal structures of a material under study and can further be used to chemically identify a material by a known structure of a common material.¹⁰²

X-rays are high-energy electromagnetic radiation (ranging from about 200 eV to 1 MeV), having wavelengths varying around 10 nm to 1pm (10^{-8} to 10^{-12} m). They are produced by the interaction of an external source of energy (beam of electrons) with the electrons in the shells of an atom. The e^- of the electron beam are derived from a cathode at a high negative potential (usually a tungsten filament). They are directed to a cooled anode (at ground potential) with a very high velocity. The energy loss arising from this impact is manifested as x-rays in a continuous spectrum of energy (x-ray wavelengths). This loss is the result of a higher energy level electron filling the vacancy in a lower energy shell left from the ejected e^- during the collision. For the XRD technique, only the $K\alpha$ wavelength (derived from an e^- of the L shell filling the K shell) of a Cu anode is important, corresponding to an x-ray photon with great energy and resulting in a diffractogram with higher intensities.¹⁵⁶

During an XRD analysis, when the x-ray beam interacts with a sample, x-rays are scattered by a regular array of scattering centers whose spacings are about the same as

the radiation wavelength. For instance, atoms and ions have size on the order of 0.1nm, so crystal structures have diffraction gratings in a subnanometer scale. The region of the electromagnetic spectrum comprising a wavelength in this range is x-radiation.¹⁰² Under these circumstances, when an x-ray beam strikes a crystal surface at some angle θ , part of the beam is scattered by the (first) layer of atoms, and the unscattered remaining penetrates to the second layer thus repeating the scattering process and penetration to the underlying layers.¹⁵⁷

Considering that the incident and diffracted radiation beams are always coplanar and with an angle between them of 2θ , a constructive interference among the scattered rays occur when the interplanar distance (d) of the crystal is in the same range of the incident wavelength (λ), satisfying Bragg's equation,

$$n \lambda = 2d \sin \theta$$

where n is an integer. Then, by knowing the incident radiation wavelength and measuring θ , the interplanar distance and further the structure of the crystal can be determined by Bragg's equation.

A.2. Differential Scanning Calorimetry

The differential scanning calorimetry (DSC) is a thermodynamical tool that analyzes the heat energy uptake/release of a sample, and at what temperature these changes take place.^{104,158} The technique is based on measuring the difference in heat flow between a sample and a reference and it gives, for each procedure, a plot of heat flow or power compensation versus temperature called thermogram.¹⁵⁷ The distinction between each plot result is that power compensation measures the change in energy flowing amidst a sample and a reference directly in mW or J/s. In contrast, heat flux analyses the difference in temperature between a sample and a reference, where it is further converted to an energy equivalent in mW.

In a thermogram plotted with heat flux vs. temperature, endothermic transitions are observed in the downward direction since they result in a negative temperature differential. Further, accordingly to an analysis plot, it is possible to identify thermodynamic transitions such as glass transition and crystallization of, for example, vitreous samples based on the thermic behavior of the analyzed sample.

The glass transition temperature (T_g) corresponds to a temperature in which a supercooled liquid becomes glass and below this region the reorganization of structural units virtually ceases and is frozen-in thermodynamically in a non-equilibrium energy state.^{159,160} Moreover, the crystallization temperature corresponds to the transition of the internal structure from a lower order structure (or SRO) to a highly ordered one (LRO), with release of energy. T_g occurs over a region in temperature, and not in a discrete point. For this reason, there are few accepted methods in the literature for T_g calculations such as:

Onset	The intersection of tangents from the baseline and initial slope of the step
Midpoint	The middle point of the step, measured as half of the step height
Endset	The intersection of tangents from the step and final baseline
Inflection point	The inflection point of the step

Reference: Paul Gabbott 2008¹⁰⁴

A.3. Raman and Infrared Spectroscopies

The most important spectroscopies for observing vibrational spectra are the infrared (IR) and Raman spectroscopies.¹⁶¹ These two techniques are used for measuring the vibrations within a molecular structure and even though some vibrations can be active in both, they derive from different mechanisms and rules.¹⁶² Thus, they are considered complementary in a study.

The Raman spectrum of a sample can be obtained by irradiating it with a monochromatic laser in the UV, visible or near-IR region.¹⁵⁷ When electromagnetic

radiation, with a *quantum* $h\nu_{ex}$, hits a molecule, it can be absorbed, transmitted or scattered. From this interaction, when the photon is momentarily absorbed and molecule transits from ground to a greater (and unstable) virtual energy state, there are two possible outcomes. The molecule can either elastically scatter a photon with same quantum energy $h\nu_0$, called Rayleigh scattering (higher probability), where no energy is lost, or inelastically scatter a photon with superior (stokes) or inferior (anti-stokes) resultant frequency and energy.^{157,161,162} The inelastic scattering of light is known as Raman, and results in a change in the vibrational and rotational energy of a molecule, having energy represented as

$$E = h(\nu_{ex} \pm \nu_s)$$

Where $h\nu_{ex}$ is the emitted photon energy and $h\nu_s$ is the scattered photon energy by the molecule in which it can be $h\nu_s^-$ if the molecule, in the ground vibrational level, re-emits a photon with lower frequency or $h\nu_s^+$ if the molecule, in a vibrationally excited state, scatters the radiation with higher frequency. Thus, when the resultant energy is higher than the emitted ($E > 0$), it is called stokes scattering and when its lower ($E < 0$) it is called anti-stokes scattering.¹⁶²

Furthermore, when a molecule is exposed to the electric field of an electromagnetic radiation, its electrons are attracted to the opposite dispersed forces, leaving one side negatively charged and the other with an excess of positive charge. This creates in the molecule an induced dipole moment μ and, dividing it by the electric field E , it provides the polarizability α .^{157,162}

$$\alpha = \mu E$$

The polarizability measures how deformable the bonds of a molecule can get in an electric field. As a result, molecular vibrations that cause a change in the polarizability are Raman active if they emit scattered radiation with different (stoke/anti-stoke) frequencies.^{157,162} As a consequence, Raman is best at symmetric vibrations of non-polar groups.¹⁶²

Similarly, the infrared spectroscopy works with frequencies in the IR region, between 14000 and 10 cm^{-1} , where mid-IR is 4000-400 cm^{-1} .¹⁶² The absorption of this radiation by a molecule results in its excitation to a higher vibrational/rotational level,¹⁶³ where only the radiation with oscillating frequency that matches with the natural frequency of a molecule will be absorbed. The resulting molecular vibration must cause a change in the dipole moment of the molecule to be considered IR active. Consequently, alternatively from Raman, IR is best for asymmetric vibrations of polar groups, .¹⁶² Thus, the difference between all emitted frequencies in the selected IR region by the matched frequency absorbed results in a spectrum given by the equipment.

A.4. Scanning Electron Microscopy

The scanning electron microscopy (SEM) is a versatile technique for providing images of external morphology with greater resolution information than the conventional optical microscopies.¹⁵⁷ This difference arises from resolution of optical light microscopy being limited by diffraction effects proportional to the wavelength of light, while SEM adopts a high energy electron beam rather than light to scan a sample surface.^{157,164} It is known that the smaller the wavelength, the greater is the resolving power revealed in an image.¹⁶⁴ Due to this fact, SEM provides images with far superior resolution since an electron beam have very short wavelength ($\lambda = 0.000004 \mu\text{m}$ or 0.04 \AA) and, when it is accelerated by a sufficiently large potential difference (1 to 100 kV), a resolving power up to 0.24 nm can be achieved.¹⁶⁴

When the electron beam interacts with the surface of a sample, it can generate an abundance of signals, in which backscattered (elastically scattered beam electrons) and secondary electrons (inelastically scattered sample electrons) are the ones used for image composition. Moreover, spatial resolution of SEM images is controlled by four important electron beam parameters, the beam current, the accelerating current, the probe size and

its convergence angle. It is also important to note that some materials provide low signal-to-noise ratio (low atomic number) and, thus, the specimens must be coated with a thin conductive (metallic) layer.¹⁶⁴

A.4.1. Statistical analysis of nanoparticle size study

The PSD can be study by central values given by mean, median and mode, and a symmetric distribution of data have these three values equivalents. Respectively, non-symmetric distribution differs for the mean, median and mode values. The SEM technique provide results on an area and shape basis, so median can be and is more frequently used to define the central point of this type of data. But the choice to evaluate central values affects the result of the analysis if the data is not normally distributed. Nonetheless, to ascertain which of them is the most accurate descriptive statistics, particle size data were submitted to a normality test in order to determine if the sample has a normal distribution.

Regarding this, Shapiro-Wilk test were used, with a confidence interval of 95%, for assessing normality of data previously the statistical analyses. According to the results from this test, only aluminum modified matrix treated for 8 and 12 minutes were statistically significant ($p > 0.05$), representing that they were the only normally distributed data. All the other particle size counts, consequently, had a non-normal distribution data ($p < 0.05$). As a consequence, determining the central value of nanoparticle size using median, instead of mean, will provide a more accurate size average representation. Considering this, the best way to graphically represent median size distribution is by using boxplot and its respective interquartile range, which presents the lower and upper limits of data, quartile range (QR - division of data into four equal parts) and percentiles.

Normally, the lower and the upper ends of a QR represent the 25th and 75th percentile, or the first and third quartile respectively, while the middle line represents the 50th percentile (Q_2) or median. The first quartile (Q_1) or 25th percentile is positioned so

that 25% of data lies below Q_1 and 75% of data lies above it. The second quartile (Q_2) or 50th percentile or median is located such that 50% (half) of data is situated below Q_2 and the other half above it. The third quartile (Q_3) or 75th percentile is placed such that 75% of data lies below Q_3 and 25% lies above it. The vertical lines expanded from the boxes (whiskers) represent the range of data, indicating the extrapolated variability from the lower and upper quartiles. The whiskers range normally comprise 1.5 and -1.5 of the interquartile range (if data is below: $Q_1 - 1.5 \times \text{IQR}$; or above: $Q_1 + 1.5 \times \text{IQR}$), in which that covers usually as much as about 99% of data, and likely only 1% will be outliers.⁸⁸

Furthermore, there are several different methods to statistically analyze the dispersion or variability of data (deviation of data from the median value), and a robust one that considers the absolute deviation of data from the median is the median absolute deviation (MAD), which is less sensitive to extremely high or low values and non-normality.

A.5. Ultraviolet-Visible Spectroscopy

Ultraviolet-visible (UV-Vis) spectroscopy is an analytical technique that measures the absorbance or transmittance of light by an analyte in the UV-VIS region, which ranges from 100 up to 800 nm¹⁴¹. The capability of a material to absorb and emit light is what defines its color¹⁴¹ and, in case of glasses, the color is governed by chromophores (metal oxides) and/or difference in nanoparticle sizes presented in the glass.¹⁶⁵ The interaction of light with a substance can result in absorbance of radiation at specific regions (UV-VIS),¹³⁶ where the ratio of incoming by the outgoing light is called transmittance or, in other words, how much light is absorbed at each wavelength¹⁴¹.

Nonetheless, when a glass has nanoparticles in its surface (within 100 nm size), light will be scattered more efficiently due to surface plasmon resonance (SPR) effect.¹³⁶ The excitation spectra, originated from the SPR, is dependent from physical features such as

size, shape, dielectric constant, composition and others¹⁶⁶ and, as a result, it is possible to qualitatively analyze nanoparticles by its plasmonic absorption bands.

A.6. Surface-enhanced Raman Spectroscopy

Surface-enhanced Raman Spectroscopy (SERS) can be defined, generally, as the Raman signal amplification by surface plasmons generated from the interaction of electromagnetic wave with a metallic surface (commonly nanoparticles).^{48,157} This strong enhancement of Raman scattering can further be attributed to areas on the nanometallic surface with highly confined local optical fields called “hot-spot”, where also maximum enhancement factor (EF) is achieved.¹⁶⁷ Overall, there are two accepted (multiplicative⁴⁸) mechanisms contributing simultaneously to the enhancement signal, one is long-range electromagnetic (EM) effect and the other is short-range chemical (CM) effect, firstly described by Fleischmann et al. in 1973.^{14,168} However, just the first mechanism will be further described here due to its great contribution to the signal improvement observed in SERS.

The electromagnetic mechanism (EM) is mainly based in the optical property called Localized Surface Plasmon Resonance (LSPR), which is the collective oscillation between (conduction) electrons presented at the interface of metallic nanoparticles with the incident wavelength of light.¹³¹ In other words, under excitation at certain frequencies, these electrons resonate with the incident optical field,^{17,29,45} producing enhanced electromagnetic fields and thus increases the scattering light signal of a particular molecule that lies close to the metallic surface.^{48,131}

Furthermore, it is important to consider that SERS spectrum of a molecule might not correspond entirely to its classical Raman spectrum. Majority of vibrational bands will correspond to vibrations of the closest bonds on a metallic surface, so orientation of molecule can affect the resultant spectrum.⁴⁸

There are several mechanisms allowing one to predict, measure or compare EF and, due to the diversity of factors contributing to SERS mechanism (such as type of metal, size and shape of nanoparticles, laser wavelength, molecule under study, etc), it is very difficult to compare EF of even similar SERS substrates.⁴⁸ Under those circumstances, it is important to describe the approaches adopted in the EF estimation to avoid bias.

References

1. Yang, D. *et al.* Photonic Crystal Nanobeam Cavities for Nanoscale Optical Sensing : A Review. (2020). doi:doi:10.3390/mi11010072
2. Sur, U. K. Surface-enhanced Raman scattering (SERS) spectroscopy: a versatile spectroscopic and analytical technique used in nanoscience and nanotechnology. *Adv. nano Res.* **1**, 111–124 (2013).
3. Park, J. *et al.* Exosome Classification by Pattern Analysis of Surface-Enhanced Raman Spectroscopy Data for Lung Cancer Diagnosis. *Anal. Chem.* **89**, 6695–6701 (2017).
4. Hernandez-Vargas, G. *et al.* Electrochemical biosensors: A solution to pollution detection with reference to environmental contaminants. *Biosensors* **8**, 1–21 (2018).
5. WHO. Ten threats to global health in 2019. Available at: <https://www.who.int/news-room/feature-stories/ten-threats-to-global-health-in-2019>. (Accessed: 21st January 2020)
6. Mitchell, S. L. & Carlson, E. E. Tiny Things with Enormous Impact: Nanotechnology in the Fight Against Infectious Disease. *ACS Infect. Dis.* **4**, 1432–1435 (2018).
7. Didkowska, J., Wojciechowska, U., Mańczuk, M. & Lobaszewski, J. Lung cancer epidemiology: Contemporary and future challenges worldwide. *Ann. Transl. Med.* **4**, 1–11 (2016).
8. Wilcox, B. A. Emerging Global Health Challenges and Integrated Health Models. **1**, 1–6 (2019).
9. Magaji, B. A., Moy, F. M., Roslani, A. C. & Law, C. W. Survival rates and predictors of survival among colorectal cancer patients in a Malaysian tertiary hospital. *BMC Cancer* **17**, 1–8 (2017).
10. Fournier, P. E. *et al.* Modern clinical microbiology: New challenges and solutions. *Nat. Rev. Microbiol.* **11**, 574–585 (2013).
11. Paul, S. *Application of Biomedical Engineering in Neuroscience. Application of Biomedical Engineering in Neuroscience* (2019). doi:10.1007/978-981-13-7142-4

12. Bohunicky, B. & Mousa, S. A. Biosensors: The new wave in cancer diagnosis. *Nanotechnol. Sci. Appl.* **4**, 1–10 (2011).
13. Liu, Y. *et al.* Plasmonic gold nanostars for Multi-Modality sensing and diagnostics. *Sensors (Switzerland)* **15**, 3706–3720 (2015).
14. Suchorska, B. *et al.* 18F-FET-PET as a biomarker for therapy response in non-contrast enhancing glioma following chemotherapy. *J. Neurooncol.* **139**, 721–730 (2018).
15. Hernández-Arteaga, A. *et al.* Diagnosis of breast cancer by analysis of sialic acid concentrations in human saliva by surface-enhanced Raman spectroscopy of silver nanoparticles. *Nano Res.* 1–9 (2017). doi:10.1007/s12274-017-1576-5
16. Silvestri, G. A. *et al.* Methods for staging non-small cell lung cancer: Diagnosis and management of lung cancer, 3rd ed: American college of chest physicians evidence-based clinical practice guidelines. *Chest* **143**, e211S-e250S (2013).
17. Lane, L. A., Qian, X. & Nie, S. SERS Nanoparticles in Medicine: From Label-Free Detection to Spectroscopic Tagging. *Chem. Rev.* **115**, 10489–10529 (2015).
18. Kim, H., Chung, D. R. & Kang, M. A new point-of-care test for the diagnosis of infectious diseases based on multiplex lateral flow immunoassays. *Analyst* **144**, 2460–2466 (2019).
19. Vidic, J., Manzano, M., Chang, C. M. & Jaffrezic-Renault, N. Advanced biosensors for detection of pathogens related to livestock and poultry. *Vet. Res.* **48**, 1–22 (2017).
20. Chen, H., Liu, K., Li, Z. & Wang, P. Point of care testing for infectious diseases. *Clin. Chim. Acta* **493**, 138–147 (2019).
21. Ding, P., Ouyang, W., Luo, J. & Kwoh, C.-K. Heterogeneous information network and its application to human health and disease. *Brief. Bioinform.* **00**, 1–20 (2019).
22. Califf, R. M. Biomarker definitions and their applications. *Exp. Biol. Med.* **243**, 213–221 (2018).
23. Gualandi, I. *et al.* Textile Organic Electrochemical Transistors as a Platform for Wearable Biosensors. *Sci. Rep.* **6**, 1–10 (2016).
24. Wang, S. Q., Chinnasamy, T., Lifson, M. A., Inci, F. & Demirci, U. Flexible Substrate-Based Devices for Point-of-Care Diagnostics. *Trends Biotechnol.* **34**, 909–921 (2016).
25. Brangel, P. *et al.* A Serological Point-of-Care Test for the Detection of IgG Antibodies against Ebola Virus in Human Survivors. *ACS Nano* **12**, 63–73 (2018).
26. Hernández-arteaga, A., Jesús, J. De, Nava, Z., Kolosovas-machuca, E. S. & Jesús,

- J. Diagnosis of breast cancer by analysis of sialic acid concentrations in human saliva by surface-enhanced Raman spectroscopy of silver nanoparticles. (2017). doi:10.1007/s12274-017-1576-5
27. Sebba, D. *et al.* A point-of-care diagnostic for differentiating Ebola from endemic febrile diseases. *Sci. Transl. Med.* **10**, 1–12 (2018).
 28. Jeon, H. Bin, Tsalu, P. V. & Ha, J. W. Shape Effect on the Refractive Index Sensitivity at Localized Surface Plasmon Resonance Inflection Points of Single Gold Nanocubes with Vertices. *Sci. Rep.* **9**, 13635 (2019).
 29. Matteini, P. *et al.* Site-Selective Surface-Enhanced Raman Detection of Proteins. *ACS Nano* **11**, 918–926 (2017).
 30. Alvarez-puebla, A. & Liz-marza, L. M. SERS-Based Diagnosis and Biodetection. 604–610 (2010). doi:10.1002/sml.200901820
 31. Xiao, L. *et al.* Untargeted Tumor Metabolomics with Liquid Chromatography-Surface-Enhanced Raman Spectroscopy. *Angew. Chemie Int. Ed.* (2019). doi:10.1002/anie.201912387
 32. Zong, C. *et al.* Surface-Enhanced Raman Spectroscopy for Bioanalysis: Reliability and Challenges. *Chem. Rev.* **118**, 4946–4980 (2018).
 33. Zhu, X. *et al.* Application of nanomaterials in the bioanalytical detection of disease-related genes. *Biosens. Bioelectron.* **74**, 113–133 (2015).
 34. Prats-Mateu, B. & Gierlinger, N. Tip in–light on: Advantages, challenges, and applications of combining AFM and Raman microscopy on biological samples. *Microsc. Res. Tech.* **80**, 30–40 (2017).
 35. Schlücker, S. Surface-enhanced raman spectroscopy: Concepts and chemical applications. *Angew. Chemie - Int. Ed.* **53**, 4756–4795 (2014).
 36. Lu, Y., Luo, Y., Lin, Z. & Huang, J. A silver-nanoparticle/cellulose-nanofiber composite as a highly effective substrate for surface-enhanced Raman spectroscopy. *Beilstein J. Nanotechnol.* **10**, 1270–1279 (2019).
 37. Lizoń, A., Wyrwal-Sarna, M., Gajewska, M. & Drozd, R. Silver nanoparticle-based assay for the detection of immunoglobulin free light chains. *Materials (Basel)*. **12**, (2019).
 38. Pereira, A. J. *et al.* Facile Shape-Controlled Fabrication of Copper Nanostructures on Borophosphate Glasses: Synthesis, Characterization, and Their Highly Sensitive Surface-Enhanced Raman Scattering (SERS) Properties. *J. Phys. Chem. C* **120**, 12265–12272 (2016).
 39. Tauran, Y., Brioude, A., Coleman, A. W., Rhimi, M. & Kim, B. Molecular

- recognition by gold, silver and copper nanoparticles. *World J. Biol. Chem.* **4**, 35 (2013).
40. Jazayeri, M. H., Amani, H., Pourfatollah, A. A., Pazoki-Toroudi, H. & Sedighimoghaddam, B. Various methods of gold nanoparticles (GNPs) conjugation to antibodies. *Sens. Bio-Sensing Res.* **9**, 17–22 (2016).
 41. Wei, C., Li, M. & Zhao, X. Surface-enhanced raman scattering (SERS) with silver nano substrates synthesized by microwave for rapid detection of foodborne pathogens. *Front. Microbiol.* **9**, 1–9 (2018).
 42. Dendisova-Vyskovska, M., Prokopec, V., Člupek, M. & Matějka, P. Comparison of SERS effectiveness of copper substrates prepared by different methods: What are the values of enhancement factors? *J. Raman Spectrosc.* **43**, 181–186 (2012).
 43. Zito, G., Rusciano, G., Pesce, G., Dochshanov, A. & Sasso, A. Surface-enhanced Raman imaging of cell membrane by a highly homogeneous and isotropic silver nanostructure. *R. Soc. Chem.* (2015). doi:10.1039/c5nr01341k
 44. Wang, Y., Salehi, M., Schütz, M., Rudi, K. & Schlücker, S. Microspectroscopic SERS detection of interleukin-6 with rationally designed gold/silver nanoshells. *Analyst* **138**, 1764–1771 (2013).
 45. Caires, A. J., Alves, D. C. B., Fantini, C., Ferlauto, A. S. & Ladeira, L. O. One-pot in situ photochemical synthesis of graphene oxide/gold nanorod nanocomposites for surface-enhanced Raman spectroscopy. *RSC Adv.* **5**, 46552–46557 (2015).
 46. Jana, J., Ganguly, M. & Pal, T. Enlightening surface plasmon resonance effect of metal nanoparticles for practical spectroscopic application. *RSC Adv.* **6**, 86174–86211 (2016).
 47. Jatschka, J., Dathe, A., Csáki, A., Fritzsche, W. & Stranik, O. Propagating and localized surface plasmon resonance sensing - A critical comparison based on measurements and theory. *Sens. Bio-Sensing Res.* **7**, 62–70 (2016).
 48. Le Ru, E. C., Blackie, E., Meyer, M. & Etchegoint, P. G. Surface enhanced raman scattering enhancement factors: A comprehensive study. *J. Phys. Chem. C* **111**, 13794–13803 (2007).
 49. Zhang, X. *et al.* Ultrasensitive SERS performance in 3D ‘sunflower-like’ nanoarrays decorated with Ag nanoparticles. *Nanoscale* **9**, 3114–3120 (2017).
 50. Quero, G. *et al.* Nanosphere lithography on fiber: Towards engineered lab-on-fiber SERS optodes. *Sensors (Switzerland)* **18**, 1–15 (2018).
 51. Liu, X., Shao, Y., Tang, Y. & Yao, K. F. Highly Uniform and Reproducible Surface Enhanced Raman Scattering on Air-stable Metallic Glassy Nanowire Array. *Sci.*

-
- Rep.* **4**, 1–7 (2014).
52. Zhu, L. *et al.* Enhanced Surface-Enhanced Raman Scattering (SERS) Sensitivity by the Self-Assembly of Silver Nanoparticles (Ag NPs) Laminated on Polydimethylsiloxane (PDMS). *Anal. Lett.* **52**, 2868–2882 (2019).
53. Chen, W. *et al.* Substrate influence on the polarization dependence of SERS in crossed metal nanowires. *J. Mater. Chem. C* **5**, 7028–7034 (2017).
54. Ke, Y., Meng, G., Huang, Z. & Zhou, N. Electrospayed large-area membranes of Ag-nanocubes embedded in cellulose acetate microspheres as homogeneous SERS substrates. *J. Mater. Chem. C* **5**, 1402–1408 (2017).
55. Kim, W. *et al.* A label-free cellulose SERS biosensor chip with improvement of nanoparticle-enhanced LSPR effects for early diagnosis of subarachnoid hemorrhage-induced complications. *Biosens. Bioelectron.* **111**, 59–65 (2018).
56. Park, M., Jung, H., Jeong, Y. & Jeong, K. H. Plasmonic Schirmer Strip for Human Tear-Based Gouty Arthritis Diagnosis Using Surface-Enhanced Raman Scattering. *ACS Nano* **11**, 438–443 (2016).
57. Panneerselvam, R., Xiao, L., Waites, K. B., Atkinson, T. P. & Dluhy, A. A rapid and simple chemical method for the preparation of Ag colloids for surface-enhanced Raman spectroscopy using the Ag mirror reaction. *Vib. Spectroscopy* **1**, 1–7 (2018).
58. Lee, P. C. & Meisel, D. Adsorption and surface-enhanced Raman of dyes on silver and gold sols. *J. Phys. Chem.* **86**, 3391–3395 (1982).
59. Szekeres, G. P. & Kneipp, J. SERS probing of proteins in gold nanoparticle agglomerates. *Front. Chem.* **7**, 1–10 (2019).
60. Almeahadi, L. M., Curley, S. M., Tokranova, N. A., Tenenbaum, S. A. & Lednev, I. K. Surface Enhanced Raman Spectroscopy for Single Molecule Protein Detection. *Sci. Rep.* **9**, 1–9 (2019).
61. Novikov, S. M. *et al.* Highly stable silver nanoparticles for SERS applications. *J. Phys. Conf. Ser.* **1092**, (2018).
62. Solís, D. M., Taboada, J. M., Obelleiro, F., Liz-Marzán, L. M. & García De Abajo, F. J. Optimization of Nanoparticle-Based SERS Substrates through Large-Scale Realistic Simulations. *ACS Photonics* **4**, 329–337 (2017).
63. Fan, M. & Brolo, A. G. Silver nanoparticles self assembly as SERS substrates with near single molecule detection limit. *Phys. Chem. Chem. Phys.* **11**, 7348–7349 (2009).
64. Schneider, R., Felix, J. F., Moura, L. G. & Morais, P. C. One step fabrication of glass-silver@core-shell fibers: Silver-doped phosphate glasses as precursors of SERS
-

- substrates. *J. Mater. Chem. C* **2**, 9021–9027 (2014).
65. Belusso, L. C. S. *et al.* Synthesis of silver nanoparticles from bottom up approach on borophosphate glass and their applications as SERS, antibacterial and glass-based catalyst. *Appl. Surf. Sci.* **473**, 303–312 (2019).
66. Lenz, G. F. *et al.* Self-supported copper (Cu) and Cu-based nanoparticle growth by bottom-up process onto borophosphate glasses. *J. Mater. Sci.* **52**, 6635–6646 (2017).
67. Zanotto, E. D. & Mauro, J. C. The glassy state of matter: Its definition and ultimate fate. *J. Non. Cryst. Solids* **471**, 490–495 (2017).
68. Yadav, A. K. & Singh, P. A review of the structures of oxide glasses by Raman spectroscopy. *RSC Adv.* **5**, 67583–67609 (2015).
69. Stebbins, J. F., Dubinsky, E. V., Kanehashi, K. & Kelsey, K. E. Temperature effects on non-bridging oxygen and aluminum coordination number in calcium aluminosilicate glasses and melts. *Geochim. Cosmochim. Acta* **72**, 910–925 (2008).
70. Koudelka, L. & Mošner, P. Borophosphate glasses of the ZnO-B₂O₃-P₂O₅ system. *Mater. Lett.* **42**, 194–199 (2000).
71. Carta, D. *et al.* The effect of composition on the structure of sodium borophosphate glasses. *J. Non. Cryst. Solids* **354**, 3671–3677 (2008).
72. Rao, K. J. *Structural Chemistry of Glasses*. (Elsevier, 2002).
73. Venkateswara Rao, G. & Shashikala, H. D. Optical and mechanical properties of calcium phosphate glasses. *Glas. Phys. Chem.* **40**, 303–309 (2014).
74. Karabulut, M. *et al.* Mechanical and structural properties of phosphate glasses. *J. Non. Cryst. Solids* **288**, 8–17 (2001).
75. Choudhary, B. P., Rai, S. & Singh, N. B. Structure and properties of silver phosphate glasses doped with copper oxide nanoparticles. *Emerg. Mater. Res.* **6**, 285–295 (2017).
76. Kim, N.-J., Im, S.-H., Kim, D.-H., Yoon, D.-K. & Ryu, B.-K. Structure and Properties of Borophosphate Glasses. *Electron. Mater. Lett.* **6**, 103–106 (2010).
77. Sadok, K. H., Haouari, M., Gallot-Lavallée, O. & Ben Ouada, H. Effect of Na₂SO₄ substitution for Na₂O on the structural and electrical properties of a sodium borophosphate glass. *J. Alloys Compd.* 878–888 (2019). doi:10.1016/j.jallcom.2018.11.203
78. Podstawka, E., Ozaki, Y. & Proniewicz, L. M. Adsorption of S-S containing proteins on a colloidal silver surface studied by surface-enhanced Raman spectroscopy. *Appl. Spectrosc.* **58**, 1147–1156 (2004).

-
79. Park, H. *et al.* SERS imaging of HER2-overexpressed MCF7 cells using antibody-conjugated gold nanorods. *Phys. Chem. Chem. Phys.* **11**, 7348–7349 (2009).
80. Zhang, D., Ansar, S. M., Vangala, K. & Jiang, D. Protein adsorption drastically reduces surface-enhanced Raman signal of dye molecules. *J. Raman Spectrosc.* **41**, 952–957 (2009).
81. Chuong, T. T. *et al.* Dual-reporter SERS-based biomolecular assay with reduced false-positive signals. *Proc. Natl. Acad. Sci. U. S. A.* **114**, 9056–9061 (2017).
82. Li, L., Hutter, T., Steiner, U. & Mahajan, S. Single molecule SERS and detection of biomolecules with a single gold nanoparticle on a mirror junction. *Analyst* **138**, 4574–4578 (2013).
83. Wiseman, M. E. & Frank, C. W. Antibody adsorption and orientation on hydrophobic surfaces. *Langmuir* **28**, 1765–1774 (2012).
84. Cowcher, D. P. *et al.* Detection of Protein Glycosylation Using Tip-Enhanced Raman Scattering. *Anal. Chem.* **88**, 2105–2112 (2016).
85. Bizzarri, A. R. & Cannistraro, S. Surface-enhanced resonance Raman spectroscopy signals from single myoglobin molecules. *Appl. Spectrosc.* **56**, 1531–1537 (2002).
86. Delfino, I., Bizzarri, A. R. & Cannistraro, S. Single-molecule detection of yeast cytochrome c by Surface-Enhanced Raman Spectroscopy. *Biophys. Chem.* **113**, 41–51 (2005).
87. Lenz, G. F. *et al.* Self-supported copper (Cu) and Cu-based nanoparticle growth by bottom-up process onto borophosphate glasses. *J. Mater. Sci.* **52**, 6635–6646 (2017).
88. Forthofer, R. N., Lee, E. S. & Hernandez, M. *Biostatistics: Analysis, and to Design, A Guide to Discovery.* (ELSEVIER Academic Press, 2007). doi:10.1192/bjp.111.479.1009-a
89. Clayton, K. N., Salameh, J. W., Wereley, S. T. & Kinzer-Ursem, T. L. Physical characterization of nanoparticle size and surface modification using particle scattering diffusometry. *Biomicrofluidics* **10**, 1–14 (2016).
90. Bonett, D. G. Confidence interval for a coefficient of quartile variation. *Comput. Stat. Data Anal.* **50**, 2953–2957 (2006).
91. Qian, X. M. & Nie, S. M. Single-molecule and single-nanoparticle SERS: From fundamental mechanisms to biomedical applications. *Chem. Soc. Rev.* **37**, 912–920 (2008).
92. Zhang, L., Lang, X., Hirata, A. & Chen, M. Wrinkled nanoporous gold films with ultrahigh surface-enhanced Raman scattering enhancement. *ACS Nano* **5**, 4407–4413 (2011).
-

-
93. Kumar, S., Aaron, J. & Sokolov, K. Directional conjugation of antibodies to nanoparticles for synthesis of multiplexed optical contrast agents with both delivery and targeting moieties. *Nat. Protoc.* **3**, 314–320 (2008).
 94. Gautam, R., Vanga, S., Ariese, F. & Umapathy, S. Review of multidimensional data processing approaches for Raman and infrared spectroscopy. *EPJ Tech. Instrum.* **2**, (2015).
 95. Parachalil, D. R., Brankin, B., McIntyre, J. & Byrne, H. J. Raman spectroscopic analysis of high molecular weight proteins in solution—considerations for sample analysis and data pre-processing. *Analyst* **143**, 5987–5998 (2018).
 96. Bates, S. *et al.* Analysis of amorphous and nanocrystalline solids from their X-ray diffraction patterns. *Pharm. Res.* **23**, 2333–2349 (2006).
 97. Zachariasen, W. H. The atomic arrangement in glass. *J. Am. Chem. Soc.* **54**, 3841–3851 (1932).
 98. Reynoso, V. C. S. *et al.* Crystallization kinetics in phosphate sodium-based glass studied by DSC technique. *J. Phys. Chem. Solids* **64**, 27–30 (2003).
 99. Wishall, C. FAST ION TRANSPORT IN OXIDE GLASSES *. *J. Healthc. Risk Manag.* **24**, 34–35 (2009).
 100. Ehrt, D. & Flügel, S. Electrical conductivity and viscosity of phosphate glasses and melts. *J. Non. Cryst. Solids* **498**, 461–469 (2018).
 101. Tricot, G., Revel, B. & Wegner, S. Thermal stability of a low Tg phosphate glass investigated by DSC, XRD and solid state NMR. *J. Non. Cryst. Solids* **357**, 2708–2712 (2011).
 102. Shackelford, J. F. *Introduction to Materials Science for Engineers.* (2014).
 103. Saitoh, A. *et al.* The structure and properties of $x\text{ZnO}-(67-x)\text{SnO}-\text{P}_2\text{O}_5$ glasses: (I) optical and thermal properties, Raman and infrared spectroscopies. *J. Non. Cryst. Solids* **484**, 132–138 (2018).
 104. Gabbott, P. *Principles and Applications of Thermal Analysis.* (2008).
 105. Mandlule, A., Döhler, F., Van Wüllen, L., Kasuga, T. & Brauer, D. S. Changes in structure and thermal properties with phosphate content of ternary calcium sodium phosphate glasses. *J. Non. Cryst. Solids* **392–393**, 31–38 (2014).
 106. Brauer, D. S., Wilson, R. M. & Kasuga, T. Multicomponent phosphate invert glasses with improved processing. *J. Non. Cryst. Solids* **358**, 1720–1723 (2012).
 107. Christie, J. K., Ainsworth, R. I. & De Leeuw, N. H. Investigating structural features which control the dissolution of bioactive phosphate glasses: Beyond the network connectivity. *J. Non. Cryst. Solids* **432**, 31–34 (2016).

-
108. Lima, C. L. J. de *et al.* Thermal, Structural and Crystallization Study of Niobium Potassium Phosphate Glasses. *Mater. Res.* **18**, 13–16 (2015).
 109. Choi, J. H., Cha, D. H., Kim, J. H. & Kim, H. J. Development of thermally stable and moldable chalcogenide glass for flexible infrared lenses. *J. Mater. Res.* **31**, 1674–1680 (2016).
 110. Zhang, S. & Stamboulis, A. Effect of zinc substitution for calcium on the crystallisation of calcium fluoro-alumino-silicate glasses. *J. Non. Cryst. Solids* **432**, 300–306 (2016).
 111. Jain, P. K., Deepika & Saxena, N. S. Glass transition, thermal stability and glass-forming ability of Se 90In10-xSbx (x = 0, 2, 4, 6, 8, 10) chalcogenide glasses. *Philos. Mag.* **89**, 641–650 (2009).
 112. Kosmal, M., Reben, M., Pichniarczyk, P., Ziabka, M. & Skrzypek, S. J. Surface crystallization and phase evolution of BaO–SrO–TiO₂–SiO₂–Al₂O₃-based glass ceramics. *J. Therm. Anal. Calorim.* **130**, 221–228 (2017).
 113. Bash, E. Structural Theories of Glass Formation Different. *PhD Propos.* **1**, 12–66 (2015).
 114. Cassanjes, F. C. *et al.* Thermal, Structural and Crystallization Study of Niobium Potassium Phosphate Glasses. *Mater. Res.* **18**, 13–16 (2015).
 115. Chen, Z., Xu, X., Zhang, H., Chen, S. & Su, J. Effect of the Addition of Large Atomic Size Elements on the Glass Formation of Al-Ca-Ni Amorphous Alloys. *IOP Conf. Ser. Mater. Sci. Eng.* **394**, (2018).
 116. Inoue, A. Amorphous, nanoquasicrystalline and nanocrystalline alloys in Al-based systems. *Prog. Mater. Sci.* **43**, 365–520 (1998).
 117. Matzkeit, Y. H. *et al.* Borophosphate glasses: Synthesis, characterization and application as catalyst for bis(indolyl)methanes synthesis under greener conditions. *J. Non. Cryst. Solids* **498**, 153–159 (2018).
 118. Szumera, M., Waclawska, I. & Sułowska, J. Influence of CuO and ZnO addition on the multicomponent phosphate glasses: Spectroscopic studies. *J. Mol. Struct.* **1114**, 78–83 (2016).
 119. Langar, A., Sdiri, N., Elhouichet, H. & Ferid, M. Structure and electrical characterization of ZnO-Ag phosphate glasses. *Results Phys.* **7**, 1022–1029 (2017).
 120. Chen, P., Li, S., Qiao, W. & Li, Y. Structure and crystallization of ZnO-B₂O₃-P₂O₅ glasses. *Glas. Phys. Chem.* **37**, 29–33 (2011).
 121. Jayasimhadri, M. *et al.* White light generation from Dy³⁺ -doped ZnO- B₂ O₃ - P₂ O₅ glasses. *J. Appl. Phys.* **106**, (2009).
-

-
122. Kim, Y. S., Choi, W. G. & Ryu, B. K. Effect of ZnO content change on the structure and properties of zinc borophosphate glasses. *Glas. Phys. Chem.* **40**, 408–414 (2014).
123. Matzkeit, Y. H. *et al.* Borophosphate glasses: Synthesis, characterization and application as catalyst for bis(indolyl)methanes synthesis under greener conditions. *J. Non. Cryst. Solids* **498**, 153–159 (2018).
124. Lim, J. W. (Austin). The properties and structure of tin phosphate glasses modified with other oxides. 1–95 (2010).
125. Langer, J. S. Theories of glass formation and the glass transition. *Reports Prog. Phys.* **77**, (2014).
126. El-Damrawi, G., Hassan, A., Doweidar, H. & Shaboub, A. Structural Studies on Ag₂O-P₂O₅ Glasses. *New J. Glas. Ceram.* **07**, 77–89 (2017).
127. Karabulut, M., Yuce, B., Bozdogan, O., Ertap, H. & Mammadov, G. M. Effect of boron addition on the structure and properties of iron phosphate glasses. *J. Non. Cryst. Solids* **357**, 1455–1462 (2011).
128. Brow, R. K. Review: the structure of simple phosphate glasses. *J. Non. Cryst. Solids* **263**, 1–28 (2000).
129. Massera, J., Mishra, A., Guastella, S., Ferraris, S. & Verne, E. Surface functionalization of phosphate-based bioactive glasses with 3-aminopropyltriethoxysilane (APTS). *Biomed. Glas.* **2**, 51–62 (2016).
130. Israelsen, N. D., Hanson, C. & Vargis, E. Nanoparticle properties and synthesis effects on surface-enhanced Raman scattering enhancement factor: An introduction. *Sci. World J.* **2015**, (2015).
131. Holban, A. M. & Grumezescu, A. M. *Nanoarchitectonics for Smart Delivery and Drug Targeting. Nanoarchitectonics for Smart Delivery and Drug Targeting* (2016). doi:10.1016/c2015-0-06101-9
132. Jiménez, J. A., Sendova, M. & Liu, H. Evolution of the optical properties of a silver-doped phosphate glass during thermal treatment. *J. Lumin.* **131**, 535–538 (2011).
133. Bian, J. C. *et al.* Electrodeposition of silver nanoparticle arrays on ITO coated glass and their application as reproducible surface-enhanced Raman scattering substrate. *Appl. Surf. Sci.* **258**, 1831–1835 (2011).
134. Yamaguchi, T. *et al.* The mobility of proton carriers in phosphate glasses depends on polymerization of the phosphate framework. *Phys. Chem. Chem. Phys.* **19**, 29669–29675 (2017).
135. Pavić, L., Krivačić, S., Moguš-Milanković, A. & Šantić, A. Low potassium mobility in iron pyrophosphate glasses. *J. Non. Cryst. Solids* **535**, (2020).
-

-
136. Titus, D., James Jebaseelan Samuel, E. & Roopan, S. M. *Nanoparticle characterization techniques. Green Synthesis, Characterization and Applications of Nanoparticles* (Elsevier Inc., 2019). doi:10.1016/b978-0-08-102579-6.00012-5
 137. Fan, X., Zheng, W. & Singh, D. J. Light scattering and surface plasmons on small spherical particles. *Light Sci. Appl.* **3**, 1–14 (2014).
 138. Bruzas, I., Lum, W., Gorunmez, Z. & Sagle, L. Advances in surface-enhanced Raman spectroscopy (SERS) substrates for lipid and protein characterization: Sensing and beyond. *Analyst* **143**, 3990–4008 (2018).
 139. Eccles, J. W. L. *et al.* UV-Vis plasmon studies of metal nanoparticles. *J. Phys. Conf. Ser.* **241**, 012090 (2010).
 140. Paramelle, D. *et al.* A rapid method to estimate the concentration of citrate capped silver nanoparticles from UV-visible light spectra. *Analyst* **139**, 4855–4861 (2014).
 141. Rocha, F. S., Gomes, A. J., Lunardi, C. N., Kaliaguine, S. & Patience, G. S. Experimental methods in chemical engineering: Ultraviolet visible spectroscopy—UV-Vis. *Can. J. Chem. Eng.* **96**, 2512–2517 (2018).
 142. Mogensen, K. B. & Kneipp, K. Size-dependent shifts of plasmon resonance in silver nanoparticle films using controlled dissolution: Monitoring the onset of surface screening effects. *J. Phys. Chem. C* **118**, 28075–28083 (2014).
 143. Nikonorov, N. V., A.I., S. & V.A., T. Silver Nanoparticles in Oxide Glasses: Technologies and Properties. *Silver Nanoparticles* 177–201 (2010). doi:10.5772/8506
 144. Pînzaru, S. C., Falamas, A., Dehelean, C., Morari, C. & Venter, M. Double amino functionalized ag nanoparticles as SERS tags in raman diagnostic. *Croat. Chem. Acta* **86**, 233–244 (2013).
 145. He, R. X., Liang, R., Peng, P. & Norman Zhou, Y. Effect of the size of silver nanoparticles on SERS signal enhancement. *J. Nanoparticle Res.* **19**, (2017).
 146. Yuen, C., Zheng, W. E. I. & Huang, Z. Surface-enhanced raman scattering: principles, nanostructures, fabrications, and biomedical applications. **1**, 267–284 (2008).
 147. Wang, Q. *et al.* Large-scale diamond silver nanoparticle arrays as uniform and sensitive SERS substrates fabricated by surface plasmon lithography technology. *Opt. Commun.* **444**, 56–62 (2019).
 148. Han, Y. *et al.* Effect of oxidation on surface-enhanced raman scattering activity of silver nanoparticles: A quantitative correlation. *Anal. Chem.* **83**, 5873–5880 (2011).
 149. Fazio, B. *et al.* SERS detection of Biomolecules at Physiological pH via aggregation of Gold Nanorods mediated by Optical Forces and Plasmonic Heating. *Sci. Rep.* **6**,
-

- 1–13 (2016).
150. Ettah, I. & Ashton, L. Engaging with Raman Spectroscopy to Investigate Antibody Aggregation. *Antibodies* **7**, 24 (2018).
 151. Fortes, A. D. *et al.* Structure, hydrogen bonding and thermal expansion of ammonium carbonate monohydrate. *Acta Crystallogr. Sect. B Struct. Sci. Cryst. Eng. Mater.* **70**, 948–962 (2014).
 152. Maleki, M. S., Moradi, O. & Tahmasebi, S. Adsorption of albumin by gold nanoparticles: Equilibrium and thermodynamics studies. *Arab. J. Chem.* **10**, S491–S502 (2017).
 153. Oje, A. I., Ogwu, A. A., Mirzaeian, M., Tsendzughul, N. & Oje, A. M. Pseudocapacitance of silver oxide thin film electrodes in ionic liquid for electrochemical energy applications. *J. Sci. Adv. Mater. Devices* **4**, 213–222 (2019).
 154. Wei, T., Kaewtathip, S. & Shing, K. Buffer effect on protein adsorption at liquid/solid interface. *J. Phys. Chem. C* **113**, 2053–2062 (2009).
 155. Kahraman, M. & Wachsmann-Hogiu, S. Label-free and direct protein detection on 3D plasmonic nanovoid structures using surface-enhanced Raman scattering. *Anal. Chim. Acta* **856**, 74–81 (2015).
 156. Suryanarayana, C. & Norton, M. G. *X-Ray Diffraction a practical approach*. (1998). doi:10.1007/978-1-4899-0148-4
 157. Skoog, D. A., Crouch, S. R. & Holler, F. J. *Principles of Instrumental Analysis*. (2016).
 158. Gill, P., Moghadam, T. T. & Ranjbar, B. Differential Scanning Calorimetry Techniques: Applications in Biology and Nanoscience. *J. Biomol. Tech.* **21**, 167–193 (2010).
 159. Baur, E., Ruhrberg, K. & Woishnis, W. *Chemical resistance of commodity thermoplastics*. *Chemical Resistance of Commodity Thermoplastics* (2016). doi:10.1016/c2012-0-06185-6
 160. Schmelzer, J. W. P. & Tropin, T. V. Glass transition, crystallization of glass-forming melts, and entropy. *Entropy* **20**, 1–32 (2018).
 161. Schrader, B. *Infrared and Raman Spectroscopy*. (1995).
 162. Larkin, P. J. *IR and Raman Spectroscopy Principles and Spectral Interpretation*. (2011). doi:10.1017/CBO9781107415324.004
 163. Ru, E. Le & Etchegoin, P. *Principles of Surface Enhanced Raman Spectroscopy and related plasmonic effects*. (2009).

164. Ul-Hamid, A. *A Beginners' Guide to Scanning Electron Microscopy*. (2018). doi:10.1007/978-3-319-98482-7
165. Möncke, D., Papageorgiou, M., Winterstein-Beckmann, A. & Zacharias, N. Roman glasses coloured by dissolved transition metal ions: Redox-reactions, optical spectroscopy and ligand field theory. *J. Archaeol. Sci.* **46**, 23–36 (2014).
166. Ali, S., Khan, Y., Iqbal, Y., Hayat, K. & Ali, M. Size determination of gold nanoparticles in silicate glasses by UV–Vis spectroscopy. *J. Nanophotonics* **11**, 016011 (2017).
167. Ozaki, Y., Kneipp, K. & Aroca, R. *Frontiers of Surface-Enhanced Raman Scattering - Single Nanoparticles and Single Cells*. (2014).
168. Fleischmann, M., Hendra, P. J. & McQuillan, A. J. Raman spectra of pyridine adsorbed at a silver electrode. *Chem. Phys. Lett.* **26**, 163–166 (1974).